The thermal fluctuations of red blood cells

Submitted by John Hale, to the University of Exeter as a thesis for the degree of Doctor of Philosophy in Physics, September 2009.

I certify that all material in this thesis which is not my own work has been identified and that no material has previously been submitted and approved for the award of a degree by this or any other University.

. . . . . John Hale

Abstract

In this thesis, we describe the development of a new technique for determination of the mechanical properties of the red blood cell membrane from measurement of its thermal fluctuations. Experimentally, the shape fluctuations of the equatorial contours of red blood cells are recorded using fast phase-contrast video microscopy, from which the Fourier fluctuation spectrum is obtained and analysed. The experimentally obtained fluctuation spectra are interpreted using a coarse grained particle dynamics simulation which models the thermal fluctuations of an elastic mesh endowed with bending and shear elasticity, and constant volume and surface area. We demonstrate that the simulation correctly describes the mean shape of the red cell as well as the membrane thermal fluctuations. Comparison between theory and experiment leads to physically sound values for the relevant membrane elastic moduli and helps distinguish between the contributions of the lipid bilayer and the membrane skeleton.

We extend this technique to investigate the mechanical response of red blood cells to oxidative stress. We show that it is possible to discriminate between the actions of different oxidising agents from their distinctive effects on the membrane thermal fluctuation spectrum. This allows comparative measures of the membrane material properties to be extracted using an approximate analytical model thus discriminating between the effects of each oxidising agent on different structural components of the membrane.

This technique was also applied to investigate the response of the red blood cell to oxidative stress under simulated hyperglycemic conditions characteristic for disease

states such as diabetes. We established that the membrane elasticity of glycated cells deteriorate much fasted under administration of hydrogen peroxide, which may be related to the observed microvascular complications in diabetes, characterised by disproportionately high levels of reactive oxidative species. We demonstrate that metformin, one of the most widely prescribed anti-diabetic drugs, has an ameliorative effect on the membrane mechanical properties, which is probably due to its anti-glycating effects.

The technique provides a reproducible means to assess the effects of reactive oxidative species on the red blood cell membrane mechanical properties and distinguish between effects on the protein membrane skeleton and the lipid bilayer. This makes the new method of potential value in monitoring the effects of drug induced changes hence assessing progress of treatment in terms of the antioxidant or anti-glycation properties of administered drugs in diabetes or other conditions characterised by high levels of oxidative stress.

Acknowledgements

The author wishes to thank:

Peter G. Petrov, C. Peter Winlove, Gianluca Marcelli, Kim H. Parker, Jackie Whatmore, Claire Ball and all my friends and colleagues in the School of Physics.

Contents

List of Figures

List of Tables

Publications and Conferences

Red blood cell thermal fluctuations: comparison between experiment and molecular dynamics simulations

John P. Hale, Gianluca Marcelli, Kim H. Parker, C. Peter Winlove and Peter G. Petrov

Received 27th May 2009, Accepted 4th August 2009

We outline a new method of analysis of thermal shape fluctuations of red blood cells, based on comparison between experiments and coarse-grained molecular dynamics simulations. The fluctuations of 2D equatorial contours of red blood cells are recorded experimentally using fast phase-contrast video microscopy, from which the fluctuation spectrum is calculated. The spectrum is compared to the corresponding contour fluctuation spectrum obtained from a finitetemperature particle-dynamics simulation, modelling a cell with bending and shear elasticity and conserved volume and surface area. We demonstrate that the simulation correctly describes the mean cell shape as well as the membrane thermal fluctuations, returning physically sound values for the relevant membrane elastic moduli.

Chapter 1

Introduction

All living matter is built up from cells. Each cell is enclosed by its outer plasma membrane that controls the interaction between the cell and its environment. The basic function of the membrane, outer or internal, is to act as a highly selective barrier for the exchange of molecules between the different spatial regions and compartments.

Many cell functions reside in or are directed by the cell membrane and its functional role extends well beyond that of a container for the contents of the cell. Increasing evidence shows that the mechanical properties of the cell membrane play an important role influencing its function. This makes the study of membrane physical properties of great biophysical importance.

Characterisation of the mechanical properties of the membrane has, and is expected to yield a number of advances in the understanding of membrane structure and function. Important examples include insights into the structure of membranes, in particular the coupling between the lipid/protein bilayer and the protein mesh cytoskeleton, including the role of skeletal proteins and the structure of the attachment complexes to the lipid bilayer. The study of the membrane mechanical properties provides a means to characterise in a quantitative way the physiological state of the membrane, its changes to disease, metabolic defects, or application of drugs. These developments could also lead to formulations of biotechnical applications,

such as vesicles for drug delivery or membranes combined with electronic devices for biosensors.

Included in the rest of this chapter is an introduction to the red blood cell structure and the origins of its membrane mechanical properties as currently understood. The current techniques used to experimentally determine the mechanical properties of the membrane are summarised. Further we proceed to give an overview of the theory of membrane elasticity and its relation to the red blood cell equilibrium shape and the membrane thermal fluctuations.

1.1 Red blood cell membrane structure

Red blood cells (erythrocytes, RBCs) are a major component of the blood. Their main function, ensured by the protein haemoglobin, is to supply tissue with oxygen.

RBCs are disk shaped and biconcave, i.e. of discocyte shape, and their mean diameter is approximately 8 μm. About 52% of the membrane mass consists of proteins, 40% - lipids and 8% - carbohydrates. The thickness of the RBC membrane is about 20 nm comprising of the lipid bilayer with embedded proteins coupled to the protein filament mesh of the skeleton. Although very flexible this membrane must also sustain considerable deformation: during the 120 days of the human RBC's lifetime it travels approximately 300 miles through crowded narrow blood vessels, some of which are of a smaller size than the RBC diameter.

Human RBCs are highly specialised and lack a nucleus, internal organelles, microtubules and intermediate filaments. Their distinctive biconcave shape is solely determined by the properties of their membrane. Since human RBC lack a three dimensional cytoskeletal framework or a nucleus, the biochemistry and structure of the cytoskeleton and its interactions with the lipid bilayer of the membrane is the best studied cytoskeletal/membrane complex.

Biomembranes consists of a mixture of many different amphiphilic molecules and associated proteins that reflect their diverse biological functions. However, in spite

of this chemical complexity, all biomembranes are organised according to the same universal construction principle: a lipid bilayer with embedded transmembrane proteins attached to the cytoskeleton, a protein filament mesh with associated proteins Figure (1.1).

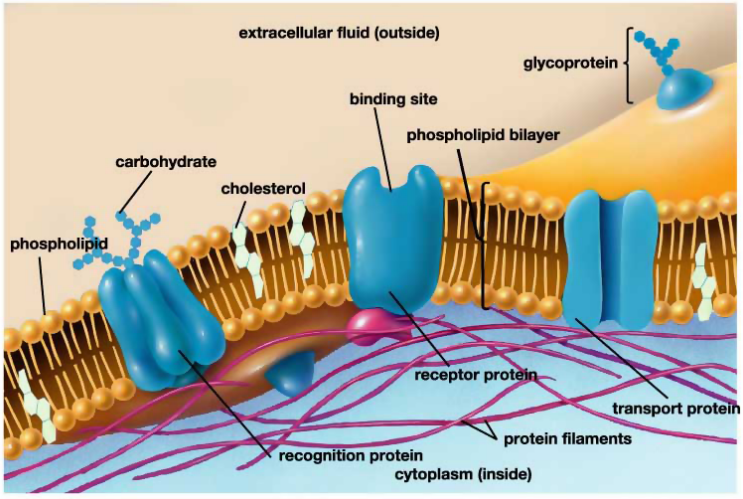

Figure 1.1: A cartoon image of the cell membrane showing the two leaflets of the membrane. The integral proteins and the attached cytoskeleton. [1]

Yet while the structure and composition of the red blood cell membrane are reasonably well understood the contributions of the various components to the mechanical properties of the membrane are not. [14]

1.1.1 Lipid bilayer

The lipid bilayer of the red blood cell membrane is composed of hundreds of different lipid species. There are three main classes of membrane lipids, phospholipids (62.7%), neutral lipids (25.2%) and glycolipids (about 12%). Phospholipids are the main component of the lipids in the membrane and are mainly glycerol based phosphoglycerides - sphingomyelin (SM) is the only phospholipid with a sphingosine backbone. The general structure of the phospholipid is the backbone, usually glycerol with two fatty acids attached to it (on carbon atoms 1 and 2) and a negatively charged phosphate group (on the 3rd carbon atom). Attached to the phosphate

are other groups (polar head) which determine the type of phospholipids. There are three of these, phosphatidylcholine (PC), phosphatidylethanolamine (PE) and phosphatidylserine (PS). Neutral lipids of human erythrocytes almost exclusively consist of cholesterol. Cholesterol is a steroid found in both leaflets of the membrane and important in maintaining the fluidity of the cell membrane by altering the packing of lipids in the bilayer. Glycolipids occur when a carbohydrate is associated with a phospholipid on the outer surface of a cell.

The lipid bilayer is not symmetric. The inner leaflet composition is dominated by the aminophospholipids PS and PE, while the outer leaflet is mainly composed of the choline phospholipids PC and SM, with no PS component. Loss of this asymmetry in the membrane has been associated with the process of cell death, in particular the exposure of inner leaflet phosopholipid PS to the outer leaflet of the membrane, which is an important signal for removal of cells by phagocytosis.

Lipid bilayers are structures formed when the head groups of the lipid molecules form two lipid/water interfaces and the tails produce a hydrophobic region within the bilayer. These structures form spontaneously due to the hydrophobic effect. The hydrophobic tails of the lipid order the water molecules which is energetically costly. Clustering of the lipids reduces the ordering of the water molecules increasing entropy. The overall shape of the lipid molecules determine the structures formed; cone shaped lipids form micelles whereas cylindrical shaped lipids form bilayers.

The unsaturated acyl chains of the phospholipids reduce the packing density due to the double bonds hindering rotation of the carbon carbon bonds of the chain maintainly the lipids in a liquid crystal phase. Cholesterol also maintains the lipid membrane in a liquid crystal phase. Cholesterol is a rigid molecule which binds to phosolipids in the bilayer reducing the its mobility thus increasing the membrane rigidity and the temperature range of the liquid crystal state of the membrane.

It is now generally excepted that the lipids are not randomly distributed within the leaflet of the bilayer but tend to form lipid rafts with distinct lipid compositions. These lipid rafts/microdomains ($10 - 200\,\mathrm{nm}$) result from lipid-lipid or lipid-protein

interactions and maybe dynamic structures and are thought to be important in the function of many membrane proteins.

Within the bilayer are embedded proteins, which have hydrophilic and hydrophobic regions. Their location and geometry determine whether the protein is an integral protein (spans across the membrane) or a peripheral protein (protrudes in or out of the cell). The main biological functions of the membrane proteins are to transport molecules/ions across the membrane, receive specific molecules such as hormones and function as enzymes. The major membrane spanning protein band 3 has three contributions to the mechanical properties include (i) an anchor point for the membrane skeleton (ii) it couples the two leaflets of the lipid bilayer membrane changing the membrane viscosity (iii) its geometry also effects the local membrane curvature. The relative importance of these effects on the mechanical properties is still a source of uncertainty [14].

1.1.2 Membrane Skeleton

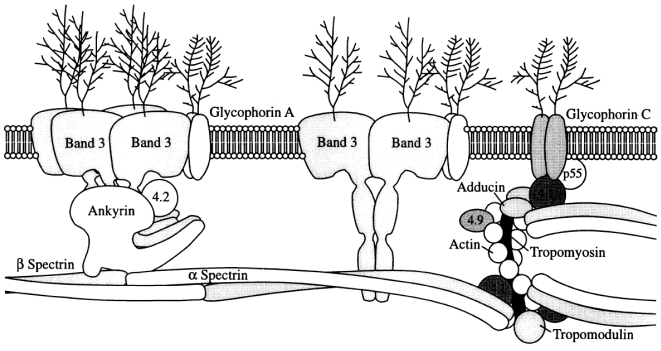

Figure 1.2: Schematic model of the red blood cell membrane, showing the anchor points structures of the spectrin membrane skeleton to the lipid bilayer. [2]

The red cell membrane skeleton is a multi-protein complex formed by structural proteins including spectrin, ankyrin, protein 4.1, actin and several other proteins. The membrane skeleton proteins interact with the lipid bilayer and transmembrane proteins to give the red cell membrane its strength and integrity. They interact with

each other to form scaffolding on the inner surface of the lipid bilayer. Spectrin dimers interact side-to-side to form flexible rod-like heterodimers which self-associate head-to-head to form tetramers. The tetramers are linked by ankyrin to the cytoplasmic domain of the integral membrane protein band 3. Protein 4.2 binds to band 3 at the same position and may enhance the ankyrin–band 3 interaction. Multiple spectrin tetramers interact at their tail ends with actin protofilaments, tropomyosin, tropomodulin and adducin to form junction complexes. Protein 4.1, which also binds to the integral membrane protein glycophorin C, interacts with spectrin at the actin binding domain and increases the affinity of the spectrin–actin binding.

High resolution electron microscopy of the stretched membrane skeleton (Figure 1.3) has provided striking images of a regular lattice like organisation with five to seven rod-shaped spectrin molecules attached to short actin filaments $30-50\,\mathrm{nm}$ in length to form a sheet of five and seven sided polygons.

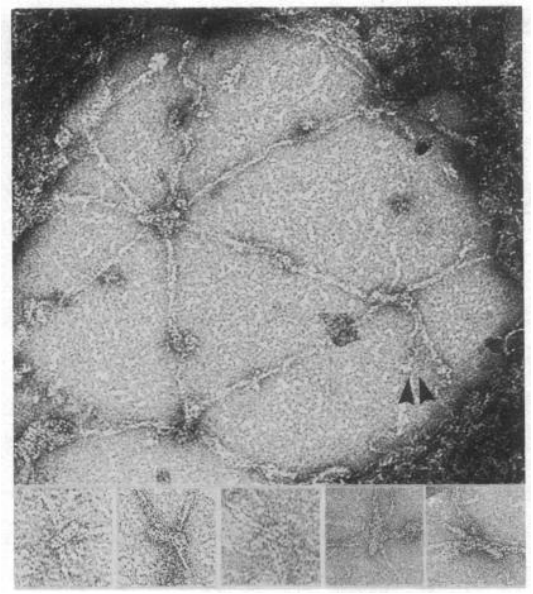

Figure 1.3: Electron microscopy image of the red blood cell membrane skeleton, clearly showing the anchor points (Band 3) to the bilayer and the connections between them (Spectrin) [3]

While its clear the shear modulus of the membrane is related to the membrane skeleton, the relative importance of the different lipid complex anchors to the mechanical properties is still unclear. Also hydrophobic parts of the spectrin molecule has been

shown to directly interact with the lipids of the bilayer.[15, 16]

1.2 Shape of RBC: Theoretical approaches

The familiar biconcave discoid shape of the normal red cell and the observed shape changes that occur physiologically have been subject of considerable research since the invention of sufficiently magnifying microscopes.

Since the red cell lacks any cytoplasmic cytoskeleton and internal structures and the origin of the red cell shape is entirely due to the mechanical properties of the membrane. The shape transitions of the red cell in pathological states are therefore due to a changes in the composition or structure of the lipid membrane or the underlying cytoskeleton, altering the mechanical properties. It is clear therefore that the understanding of the mechanical origin of the shape changes of the red cell will give some insight into the structural significance of pathological changes.

In the following theoretical treatment the membrane is considered to be homogenous. This is a reasonable approximation when considering membrane deformations on length scales greater than the bilayer thickness ($> 10\,\mathrm{nm}$) for vesicles and greater than the spectrin length for the red blood cell membrane ($> 200\,\mathrm{nm}$).

Any deformation of the cell membrane is a superposition of three deformations, pure bending, pure shearing and isotropic compression (Figure 1.4).

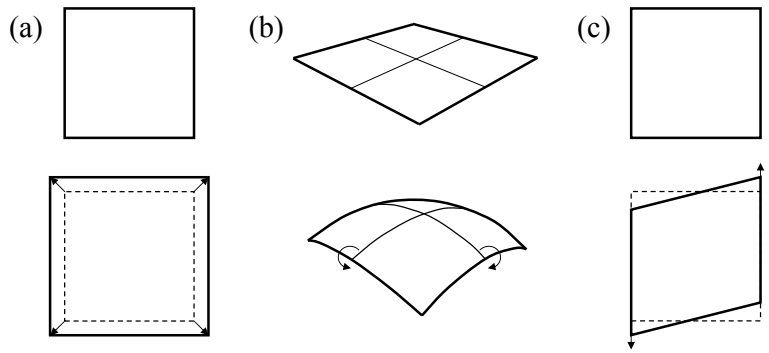

Figure 1.4: The membrane deformations. (a) stretching deformation / area compressibility. (b) bending deformation (c) shear deformation.

The resistance of lipid bilayers to isotropic tension (compression or dilation) is characterised by

$$g_{compression} = \frac{1}{2} K_c \left(\frac{\Delta A}{A} \right)^2 \tag{1.1}$$

where $\Delta A/A$ is the relative change in area and K_c is the lateral compressibility modulus measured in J/m^2.

The compressibility modulus, K_c, and the bending modulus κ are proportional to each other, such that

$$\kappa \simeq K_c / d_m^2 \tag{1.2}$$

where d_m is the membrane thickness.

Pure shearing is a deformation in which area is conserved. The energy is expressed as

$$g_{shear} = \frac{1}{2} \mu (\lambda^2 + \lambda^{-2} - 2) \tag{1.3}$$

where the strain is expressed in terms of the elongation ratio $\lambda = (L_0 + \delta L)/L_0$ and μ is the shear elastic modulus.

It is only recently that the structural similarity between the smectic liquid crystal and the fluid membrane has been used to explain the mechanical properties of lipid membrane. In the early 1970s Helfrich developed continuum physics models of the bilayer [17], treating the bilayer as a liquid crystal. This helped explain theoretically the observed shapes and shape transitions of lipid vesicles as a first approximation in describing the shape and mechanical properties of the red blood cell.

1.2.1 The Helfrich Model

Helfrich recognised that if we consider the hydrocarbon chains as aligned along the director of a uniaxial liquid crystal, the lipid bilayer can be treated as a smectic A liquid crystal with thickness twice that of the length of a lipid molecule. Based on the Frank free energy density for unaxial liquid crystal with the normal of the membrane

as the director of the liquid crystal, Helfrich deduced the curvature elasticity energy of a membrane as

$$F_{Helfrich} = \int\limits_{surface} \left[\frac{\kappa}{2}(H - H_0)^2 + \kappa_G K\right] dA \tag{1.4}$$

where the mean curvature ($H = 1/R_1 + 1/R_2$) and the Gaussian curvature ($K = 1/R_1R_2$) are given in terms of the two principle radii of curvature, R_1 and R_2 (Figure 1.5) and H_0 is the spontaneous curvature which as before describes the curvature of the bilayer in the relaxed state. The elastic constants κ and κ_G are the bending modulus and the Gaussian bending modulus, equivalent to the splay and saddle splay coefficients in the Frank energy for liquid crystals [18].

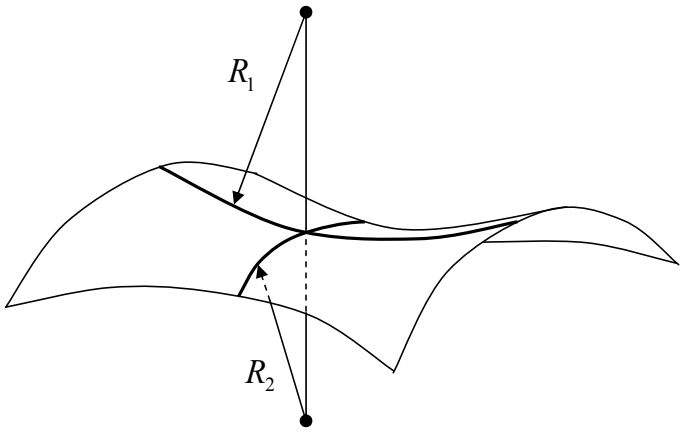

Figure 1.5: Principal radii of curvature R_1 and R_2 associated with one point of the surface.

The rigorous derivation of the Helfrich Hamiltonian is very involved. Below is a simplified treatment which describes the origin of the Hamiltonian from a simple microscopic model and gives some insight to the physics of Equation (1.4). More comprehensive treatments can be found in [19].

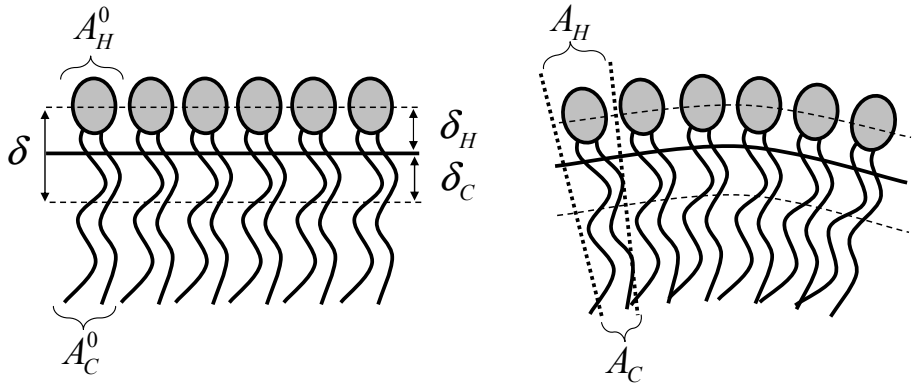

Figure 1.6: Illustration of the microscopic model showing the deformation of a lipid monolayer. The thick solid line indicating the neutral surface about which the bending moments of the head and chains (dashed lines) vanish.

The model supposes that the stresses are localised to two regions in the each monolayer of the bilayer (Figure 1.6): one corresponds to the lipid heads and the other to the lipid chains. In a harmonic approximation the elastic free energy per molecule can be written as

$$f = f_H + f_C = \frac{1}{2}k_H\left(\frac{A_H}{A_H^0} - 1\right)^2 + \frac{1}{2}k_C\left(\frac{A_C}{A_C^0} - 1\right)^2 \tag{1.5}$$

where A_H and A_C are the actual area per molecule and at the level of the heads and chains respectively, A_H^0 and A_C^0 are the unstressed areas and k_H and k_C are the respective elastic constants. The area of the neutral surface is defined as A where δ_H and δ_C are the distances from the neutral surface, where due to the lipid heads and the lipid chains defined. From the definition of the neutral surface

$$\begin{aligned} A_H &= A\left[1 + \delta_H H + \delta_H^2 K\right] \\ A_C &= A\left[1 + \delta_C H + \delta_C^2 K\right]. \end{aligned} \tag{1.6}$$

Therefore for a flat membrane where $A_H = A_C = A$ is a the point at which the sum of the moments of the stresses vanish. The equilibrium area at which f in equation

1.5 is a minimum is

$$A_0 = \left(\frac{k_H}{A_H^0} + \frac{k_C}{A_C^0}\right) / \left(\frac{k_H}{{A_H^0}^2} + \frac{k_C}{{A_C^0}^2}\right) \tag{1.7}$$

the area of the neutral surface. By substituting (1.6) and (1.7) into equation (1.5) it is possible to obtain the Helfrich energy (1.4) of the bilayer. Although the form of the Helfrich energy could be obtained by just considering the membrane as a thin elastic sheet it would be inconsistent with the fluid properties of the membrane. By considering the liquid crystalline properties of the lipid bilayer the relationship between the microscopic properties of the bilayer and its elastic properties are revealed. The bending modulus (κ), guassian bending modulus (κ_G), and spontaneous curvature (H_0) are related to the microscopic properties by

$$\begin{aligned} \kappa &= \delta_H \delta_C K_c \\ \kappa_G &\propto \left(A_H^0 - A_C^0\right) \\ H_0 &= \frac{\bar{\kappa}}{\kappa} \frac{1}{\delta_H - \delta_C}. \end{aligned} \tag{1.8}$$

Various features particular to lipid bilayers are revealed by the equations (1.8). For instance κ is proportional to δ^2 and not δ^3 as for solid plates due to the chosen stress distribution in the monolayer. For more realistic models the stresses would not be restricted to two points so $\kappa \propto \delta^n$ with $2 < n < 3$. This suggests the bending modulus would be dependent on the lipid packing and tilt. A typical value of κ can be estimated from (1.8). For typical values $K_c \simeq 0.05\,\mathrm{N}m^{-1}$ and $\delta_H \sim \delta_C \sim 10\,\text{Å}$ the bending modulus is $\kappa \simeq 12\,k_BT$. Equation (1.8) also suggests that since both κ_G and H_0 are proportional to $(A_H^0 - A_C^0)$ they could be easily modified by a change in the interaction or the lateral size of either the lipid heads or their chains (for example by methylation of the lipid chain).

The integral of the second term in (1.4) depends upon only the topology of the surface (i.e number of holes or handles) not on its shape. The Gauss-Bonnet theorem gives the identity $\int K dA = 4\pi(1-g)$ where g is the genus of the surface which is 0 for all closed topologies with no holes or handles. The second term therefore can

omitted when considering vesicles and cells of fixed topology. The other constraints on the observed shapes are the surface area and volume which combined with the (1.4) give

$$F_{Helfrich} = \int \frac{1}{2}\kappa(H - H_0)^2 dA + \delta p \int dV + \sigma \int dA \tag{1.9}$$

where the Lagrange multipliers σ and δp are the constant area and volume constraints, which physically are the osmotic pressure between the inside and outside of the cell and the surface tension. This model predicts vesicle shapes of three main types: prolates/dumbbells, oblates/discocytes, and cup-shaped stomatocytes. It is interesting to note that at a particular volume-to-area ratio, one of the solutions of the shape equation is a discocyte, the shape of a red blood cell, although no contribution of the membrane skeleton to the elastic energy is included in the free energy (1.9). The model does not however explain vesicle pear and star shapes or shapes with buds, all observed in the laboratory. It also fails to explain the echinocyte shape of the red blood cell and does not take into account the shear properties of the its membrane skeleton.

1.2.2 ADE Model

Miao et al. [20] combined the Helfrich energy and the area difference model suggested by Sheetz and Singer [21] to develop the area-difference-elasticity model (ADE model). Adding the area difference term to the Helfrich energy leads to

$$F_{ADE}[S] = \frac{\kappa}{2} \oint_S dA \, (2H - H_0)^2 + \frac{\bar{\kappa}}{2} \frac{\pi}{AD^2} (\Delta A - \Delta A_0)^2 \tag{1.10}$$

where D is the bilayer thickness, A is the membrane surface area, ΔA is the differential area between the inner and outer leaflets, $\Delta A_0 = A_0^{out} - A_0^{in}$ is the differential area of the two leaflets in the relaxed state and κ and $\bar{\kappa}$ area the local and non-local bending moduli of the membrane.

This model predicts shapes depending not only on their bending modulus and reduced volume but also on the area difference between the two leaflets of the bilayer (1.7). The elastic effects of spontaneous curvature (H_0) and the area difference term in (1.10) can be combined into a dimensionless parameter, the effective differential area,

$$\overline{\Delta a}_0 = \Delta a_0 - \frac{c_0}{2\pi\xi} \tag{1.11}$$

where ξ is the ratio of the elastic moduli, $\xi = \bar{\kappa}/\kappa$, and $c_0 = H_0 R_A$, $\Delta a_0 = \Delta A_0/8\pi D R_A$ are reduced dimensionless quantities scaled by $R_A = (A/4\pi)^{1/2}$. Using this model it is possible to predict the morphology of vesicles and their shape changes [22], successfully describing not only the shapes predicted by the Helfrich model but also pears, buds and starfish vesicles [23].

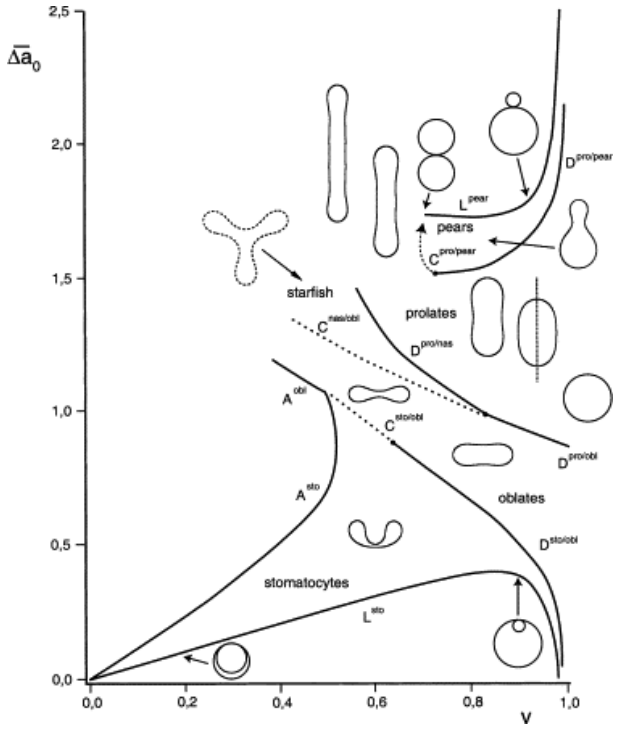

Figure 1.7: A shape phase diagram of lipid vesicles, with a fixed ratio of elastic moduli ξ, as predicted by the area-difference-elasticity model. [4]

The ADE model does exhibit the stable discocytic shape of the red blood cell, and when ΔA_0 is decreased it becomes unstable and transforms into a stomatocyte shape. However when ΔA_0 is increased rather than transform into a echinocyte the

model predicts budding of the membrane.

1.2.3 Adding shear elasticity to the ADE model

For a more comprehensive description of the RBC mechanical properties, the effects of the membrane skeleton also need to be considered. The narrow necks formed when the membrane buds produce large stretching and shear deformations. Including the membrane skeleton elasticity will raise the energy of budded shapes leaving echinocyte as the low-energy shape for sufficiently positive ΔA_0.

Lim et al. [24] added to (1.10) by considering the contribution of the membrane skeleton to the elastic free energy as defined by the ADE model.

$$F_{RBC}[S, S_0] = F_{ADE}[S] + F_{MS}[S, S_0] \tag{1.12}$$

with

$$F_{MS}[S, S_0] = \frac{K_\alpha}{2} \oint_{S_0} dA(\alpha^2 + a_3\alpha^3 + a_4\alpha^4) + \mu \oint_{S_0} dA(\beta + b_1\alpha\beta + b_2\beta^2) \tag{1.13}$$

where $\alpha = dS/dS_0 - 1 = \lambda_1\lambda_2 - 1$ and $\beta = (\lambda_1 - \lambda_2)^2/2\lambda_1\lambda_2$ are the local area and strain invariants, respectively ($\lambda_{1,2}$ are the the local principle stretches). K_α and μ are the linear elastic moduli for stretching and shear.

Using this model Lim et al. [24] showed that the contribution from the membrane skeleton is required to explain the RBC shape sequence from stomatocyte to echinocyte. This shows theoretically a stabilising effect of the membrane skeleton on the membrane.

1.3 Fluctuating Membranes

Helfrich was also the first to consider the thermal fluctuations of lipid bilayer membranes [17]. Using the Helfrich energy he was able to derive the height fluctuations

of a planar membrane. Since this pioneering work much progress has been made considering membrane with increasing complexity.

1.3.1 Flat membranes

The flat membrane is the simplest model used to examine the statistics of membrane fluctuations and commonly used to understand the effects of more complex interactions such as protein interactions, membrane confinement and protein diffusion [25, 26, 27].

When considering the fluctuations of a flat membrane it is more convenient to represent the Helfrich energy in terms of a Monge representation [28]. For small height displacement $h(x, y)$ from a reference plane the Helfrich energy is

$$F = \int\int dxdy \left\{ \frac{1}{2}\kappa(\nabla^2 h)^2 + \frac{1}{2}\sigma(\nabla h)^2 \right\} \tag{1.14}$$

where κ is the bending modulus, σ is the membrane tension and $\nabla \equiv \hat{x}\frac{\partial}{\partial x} + \hat{y}\frac{\partial}{\partial y}$ is the gradient operator in two dimensions. Since the fluctuations of the surface are described in terms of frequencies and wavelengths, it is more convenient to calculate the statistics of (1.14) if the Fourier transform of $h(x, y)$ is used:

$$\begin{aligned} \tilde{h}(q_x, q_y) = \tilde{h}(\mathbf{q}) &= \frac{1}{\sqrt{L}} \int_{-L}^{L} dx e^{iq_x x} \frac{1}{\sqrt{L}} \int_{-L}^{L} dy e^{iq_y y} h(x, y) \\ &= \frac{1}{L} \int d^2\mathbf{r} e^{i\mathbf{q}\cdot\mathbf{r}} h(\mathbf{r}). \end{aligned} \tag{1.15}$$

Similarly the inverse transform is

$$\begin{aligned} h(x, y) = h(\mathbf{r}) &= \frac{\sqrt{L}}{2\pi} \int_{-\infty}^{\infty} dq_x e^{-iq_x x} \frac{\sqrt{L}}{2\pi} \int_{-\infty}^{\infty} dq_y e^{-iq_y y} \tilde{h}(q_x, q_y) \\ &= \frac{L}{(2\pi)^2} \int d^2\mathbf{q} e^{-i\mathbf{q}\cdot\mathbf{r}} \tilde{h}(\mathbf{q}). \end{aligned} \tag{1.16}$$

Substituting h in terms of $\tilde{h}$ into the expression for energy (1.14) an expression for

the energy in terms of $\tilde{h}$ is obtained:

$$F = \frac{1}{2}\int_S d^2\mathbf{r}\Bigg\{\sigma\left(\frac{L}{(2\pi)^2}\nabla\int d^2\mathbf{q}e^{-i\mathbf{q}\cdot\mathbf{r}}\tilde{h}(\mathbf{q})\right)\left(\frac{L}{(2\pi)^2}\nabla\int d^2\mathbf{q}'e^{-i\mathbf{q}'\cdot\mathbf{r}}\tilde{h}(\mathbf{q}')\right) + \kappa\left(\frac{L}{(2\pi)^2}\nabla^2\int d^2\mathbf{q}e^{-i\mathbf{q}\cdot\mathbf{r}}\tilde{h}(\mathbf{q})\right)\left(\frac{L}{(2\pi)^2}\nabla^2\int d^2\mathbf{q}'e^{-i\mathbf{q}'\cdot\mathbf{r}}\tilde{h}(\mathbf{q}')\right)\Bigg\}. \quad (1.17)$$

Substituting $q^2 = \mathbf{q}\cdot\mathbf{q}$ and integrating out $\int d^2r$, as well as using the definition of the delta function

$$\int_{-\infty}^{\infty} dx e^{i(q_1-q_2)x} = 2\pi\delta(q_1 - q_2), \quad (1.18)$$

an expression of the energy in terms of q and the mean squared amplitude $\left|\tilde{h}(\mathbf{q})\right|^2$ is obtained

$$F = \frac{L^2}{(2\pi)^2}\int d^2\mathbf{q}\,\frac{1}{2}(\sigma q^2 + \kappa q^4)\left|\tilde{h}(\mathbf{q})\right|^2. \quad (1.19)$$

Finally, since these modes are harmonic the equipartition theorem can be applied, assigning an average energy $k_BT/2$ for each mode. This gives an equation for the mean square amplitudes of the height as a function of the wavevector q,

$$\left\langle\left|\tilde{h}(q)\right|^2\right\rangle = \frac{k_BT}{\sigma q^2 + \kappa q^4} \quad (1.20)$$

where T is the temperature, κ is the bending modulus, σ is the membrane tension and k_B is the Boltzmann constant. Equation (1.20) is the *fluctuation spectrum* of the membrane. Thus measuring experimentally the fluctuation spectra and fitting (1.20) is a practical method to measure the mechanical properties of the membrane.

In microscopy techniques often only a line through the membrane can be imaged therefore what actually is measured is $\left\langle\left|h(q_x, y=0\right|^2\right\rangle$. Therefore from equation (1.20) one can obtain [29]

$$\left\langle\left|h(q_x, y=0\right|^2\right\rangle = \frac{k_BT}{2\sigma}\left[\frac{1}{q_x} - \frac{1}{\sqrt{\frac{\sigma}{\kappa} + q_x^2}}\right]. \quad (1.21)$$

This analytical method has been extended to quasi-spherical vesicles.

Often, experimentally derived 2D contours are represented as $r(\varphi) = r_0[1+\sum_n a_n \cos(n\varphi)+ \sum_n b_n \sin(n\varphi)]$. The correspondence of $\langle|h(q_x, y=0)|\rangle$ and the experimental mean square amplitude $\langle|c_n|^2\rangle$, where $c_n^2 = a_n^2 + b_n^2$ is given by [29]

$$\langle|h(q_x, y=0)|\rangle = \frac{\pi\langle R\rangle^3}{2}\langle|c_n|^2\rangle. \tag{1.22}$$

1.3.2 Quasi-Spherical vesicles

Currently the only geometry more complex than that of a flat membrane to be solved in a purely analytical way is the quasi-spherical vesicle [30]. Of course a perfect sphere of fixed volume cannot fluctuate but quasi-spherical flaccid vesicles with a small excess area do, and their fluctuation spectra can be calculated. It is assumed in this model that the time averaged equilibrium shape is a sphere and the volume and area are conserved. The only important contribution to the excess energy of the deformed fluctuating vesicle is the curvature elastic energy. Since the area is constant the area compressibility modulus is $K_A \approx \infty$, also the vesicle has no membrane skeleton and the bilayer is a fluid so there is no shear viscosity, $\mu = 0$.

The quasi-spherical vesicle can be expanded in spherical harmonics around the a sphere. Since the curvature depends only on the normal displacement $u(\theta, \psi)$, u is chosen to express the local curvature and expanded in spherical harmonics, $Y_{nm}(\theta, \psi)$, with amplitudes $U_{nm}(t)$ giving

$$u(\theta, \psi) = \sum_{\substack{n=2,\ldots \\ m=0,\ldots\pm n}} U_{nm}(t) Y_{nm}(\theta, \psi) \tag{1.23}$$

The sum starts from $n = 2$ because the fundamental mode $n = 0$ does not conserve volume and $n = 1$ represents a uniform displacement of the entire sphere, therefore not adding to bending fluctuations.

Likewise it can be shown the spherical harmonics are linearly independent therefore the equipartition theorem can be applied with the average energy of each mode set

to $k_BT/2$. In this way the fluctuations of a quasi-spherical vesicle, can be expressed as

$$\left\langle \left| U_n^m(t) \right|^2 \right\rangle = \frac{k_BT}{\kappa} \frac{1}{(n-1)(n+2)\left[\bar{\sigma} + n(n+1)\right]} \tag{1.24}$$

where $(n = 2, \left|m\right| \leq 2)$, κ is the bending modulus and $\bar{\sigma} = \sigma \left\langle R \right\rangle^2 / \kappa$ is the dimensionless tension.

Experimentally it is only possible to measure the fluctuations of the equatorial contour of the vesicle it is therefore more practical to transform (1.24) into an equation for the mean square fluctuations of the equatorial contour [29] as follows

$$\left\langle \left| c_n \right|^2 \right\rangle = \sum_{n=p}^{n=n_{max}} \frac{2n+1}{\pi} \frac{(n-p)!}{(n+p)!} (P_n^p(0))^2 \frac{k_BT}{\kappa(n^2(n+1)^2 - (2-\sigma)n(n+1))} \tag{1.25}$$

where $P_n^p(x)$ are the associated Legendre polynomials. Clearly the quasi-spherical case is non-trivial and equation (1.25) describing the fluctuations of the contour is somewhat difficult to fit. Practically the equations (1.25) and (1.21) differ very little for $n > 5$ (the error is equal or less than the experimental error) therefore the flat membrane approximation is often used to extract the mechanical properties of vesicles [29].

1.3.3 Flicker spectroscopy of non-spherical vesicles

The quasi-spherical technique is limited to measuring the mechanical properties of vesicles near the spherical limit. For these vesicles long wavelengths are dominated by surface tension, therefore to determine κ requires the spectrum to be measured up to large mode numbers requiring large vesicles ($\sim 50\,\mu m$). The volume to area ratio changes with temperature making quasi-spherical vesicle impractical for determining the temperature dependence of κ, since they would not remain quasi-spherical. In addition, the membrane fluctuations at the spherical limit are insensitive to the effective spontaneous curvature, so $\bar{C}_0$ cannot be determined.

Döbereiner et al. [5] developed a novel technique to address the limitations of the quasi-spherical method, advanced flicker spectroscopy of non-spherical vesicles. Extensive Monte Carlo simulations of dynamically triangulated vesicles were used to generate data for a wide range of reduced volumes (v) and spontaneous curvatures ($\bar{c}_0$), which were then used to extract the elastic parameters of the vesicle membrane from the flicker spectroscopy data.

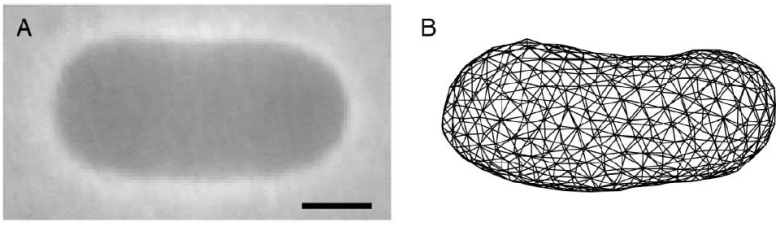

Figure 1.8: Experimental and theoretical vesicle shapes [5]. (A) Phase contrast image of a vesicle with $v = 0.828$ (black bar corresponds to $5\,\mu$m). (B) Snapshot of a simulated shape with $v = 0.825$, $\kappa/k_BT = 25$, and $\bar{c}_0 = -0.28$.

Experimentally the fluctuating prolate vesicles were recorded in phase contrast microscopy with their long-axis in the focal plane. The contours of the fluctuating vesicle were traced at rate of 2/sec to subpixel resolution. Choosing a coordinate system such that the long axis of the vesicle lies in the x-direction, each of contours are then represented in polar coordinates (r, φ) as $r(\varphi) = r_0[1 + \sum_n a_n \cos(n\varphi) + \sum_n b_n \sin(n\varphi)]$, where φ is the angle measured from the positive x axis. The time-dependent Fourier coefficients $\{a_n, b_n\}$ encode all the experimental shape fluctuation information. The mean-values $\langle a_n \rangle$ describe the mean shape ($\langle b_n \rangle = 0$ here because the contours are orientated). The mean-square amplitudes $\langle \Delta a_n^2 \rangle \equiv \langle (a_n - \langle a_n \rangle)^2 \rangle$ measure the thermal fluctuations of the vesicles about their mean shape.

The Monte Carlo simulation data is analysed in an identical fashion, taking a Fourier expansion of a two-dimensional contour in a plane through the centre of mass of the simulated vesicle. Experimental data is then fitted to the Monte Carlo data sets using the time averaged amplitudes $\langle a_2 \rangle$, $\langle a_4 \rangle$ and the mean square fluctuation amplitudes $\langle \Delta a_2^2 \rangle$, $\langle \Delta a_3^2 \rangle$, $\langle \Delta a_4^2 \rangle$, and $\langle \Delta a_5^2 \rangle$. A least squared fit to the experimental data determines the bending modulus κ, the effective spontaneous curvature c_0 and

the reduced volume v simultaneously for a given vesicle.

1.3.4 RBC Models

Marcelli et al. [31] developed a coarse grained molecular dynamics approach to simulate the thermal fluctuations of the red blood cell. The model membrane consists of a two-dimension network of $N \approx 5762$ particles arranged in a regular triangulation. Each particle of the mesh represents an area of the membrane while the network itself represents the spectrin membrane skeleton. For small deformations the mesh can be described by two elastic moduli - the area compressibility modulus K_A and the shear modulus μ. Since a free fluctuating RBC has constant area, a constant surface area constraint is applied which means that the area compressibility modulus $K_A \to \infty$.

Each particle is connected to its six nearest neighbours by linear springs, giving a harmonic potential of

$$V_{ij}^{spring} = \frac{1}{2}k\left[(r_i - r_j) - r_0\right]^2 \tag{1.26}$$

where k is the spring constant, r_i and r_j is the positions of particle i and j, and r_0 is the equilibrium distance between them (r_0 is chosen to be the average length of a spectrin filament, $\sim 100\,\mathrm{nm}$).

The dihedral potential is applied between adjacent triangles of the mesh. This potential is a discretization of the bending energy and endows the mesh with bending elasticity, and defined as

$$V_{ijml}^{dihedral} = D\left[1 + \cos(\varphi_{ijml})\right] \tag{1.27}$$

where φ_{ijml} is the dihedral angle between triangles $\triangle_{ijm}$ and $\triangle_{jml}$ (see Figure 1.9). The two dimensional network is closed and embedded in three dimensional space.

For topological reasons, there are 12 'defects' within the network where the particles have 5 connections instead of 6. The continuum limit of equation (1.27) is the

bending energy for a solid membrane [32]. This is not the same as the Helfrich bending energy for a fluid membrane however for small displacements the bending energies for solid and fluid membranes are identical [33].

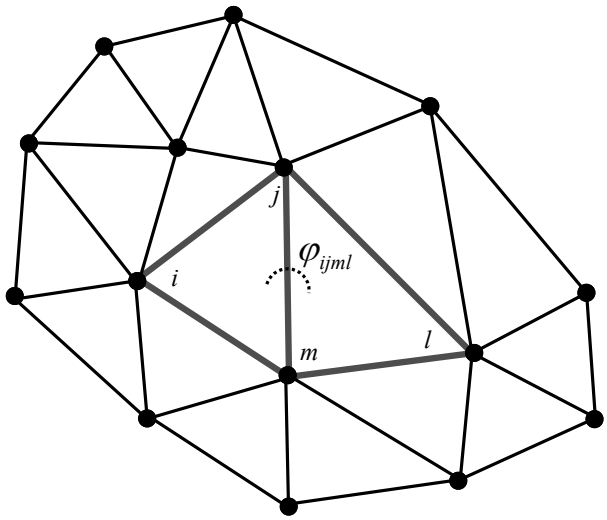

Figure 1.9: The triangularization of the red blood cell mesh. The harmonic potential is defined between the nodes e.g. i and j. The dihedral potential is defined by the angle between two adjacent triangles of harmonic potentials e.g. the angle φ_{ijml} defined between the triangles ijm and jlm.

The molecular dynamics simulations were performed using the DL_POLY v 2.12 simulation package (Daresbury Laboratory, Cheshire, UK) [34]. The temperature is kept constant using a Nose-Hoover thermostat and the value of the temperature used is T = 309 K. The constant area constraint is maintained by the Lagrange method of undetermined multipliers.

From the analysis of the dynamics of the system at equilibrium, estimates of the in-plane shear modulus and out-of-plane bending modulus can be obtained. This is done by considering a small patch of 19 points. The average z-displacement is defined as the out-of-plane height fluctuations, and analysed in same way as the flicker experiments such as point-dark-field microscopy [35]. In order to evaluate the shear modulus the average x- and y-displacements (in-plane) of the 19 particles are measured. A value of the shear modulus can be obtained from this using an expression reported by Discher et al. [36].

Using this model Marcelli et al. [31] were able to show that it is possible to observe nanometer-scale fluctuations with values of the shear and bending moduli similar to those obtained experimentally. This helped explain the 2 orders of magnitude difference between the measured value of the shear modulus for large deformation experiments such as micropipette aspiration and thermal fluctuation measurements (see Table 1.1).

1.4 Methods of measurement of the RBC mechanical properties

1.4.1 Whole blood methods

Clinically only two methods have been widely applied to determine the deformability of the red blood cell, filtration through micro-pore filters and measurement of red cell elongation due to externally applied shear stress by laser diffraction. These methods examine the rheology of the whole blood to infer information about the mechanical properties of the red blood cell.

Teitel and Radulescu [37] in 1952 were the first to describe a method for evaluating the deformability of red blood cells from their ability to pass through filter paper. This method was later improved through use of polycarbonate membrane filters with known pore size of the order of 3 μm [38]. The flow of a pure erythrocyte suspension is measured, the leukocytes are removed to avoid blocking the pores and corrupting the result. The rate of flow as a function of time gives a measure of the magnitude of the mechanical properties of the cell which determine its transit time namely, the cell geometry (including the volume to area ratio), the membrane elasticity and the cytoplasmic viscosity. Gravity flow filtration has been able to differentiate control and patient groups in numerous studies. For example, Barnes et al. [39] showed that the deformability of red blood cells in patients with diabetes did not differ significantly from normal controls when the patients did not suffer compli-

cations. Diabetics with complications showed significant decrease in deformability when compared to normal controls and diabetics with no complications.

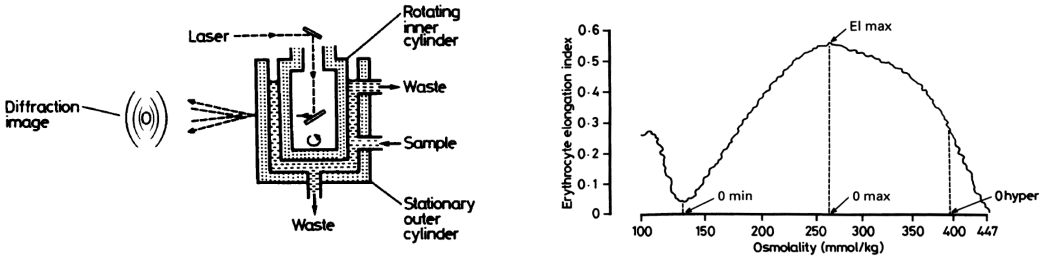

Figure 1.10: (a) Sectional drawing of ektacytometer showing the HeNe laser beam passing through the red blood cell test suspension to generate an elliptical diffraction pattern as the red blood cells are sheared by the rotation of the inner cylinder of the viscometer. (b) Typical output of the ektacytometer showing the effect of changing osmolarity on red blood cell elongation index [6].

The Ektacytometer combines a viscometer with laser diffraction and is available as a commerical instrument (LORCA, RR Mechatronics, The Netherlands)[40]. These devices work by passing a HeNe laser beam through a sample in a transparent cylindrical viscometer and measuring the geometry of the elliptical diffraction pattern produced. From the diffraction pattern the elongation index is calculated by the difference between the long and short axes over the sum of the axes $(A-B)/(A+B)$. As these devices lend themselves to flow analysis the progressive increase in osmolarity allows the elongation index to be measured as a function of the osmolarity. The osmolarity at which the peak elongation index occurs (EI max, Figure 1.10) is a measure is a measure of the mean volume to area ratio of the sample. Any reduction in the volume to area ratio would cause the peak to move to the right as in autoimmune haemolytic anaemia and likewise with excess area as in liver failure the peak would move to the left. The peak elongation index occurs at physiological osmolarity and is a sensitive measure of the mean cell elasticity.

The availability and wide use of these devices is a tribute to their reliability and clinical success but they only give an overall assessment of the cell deformability and do not give much information about the detailed mechanical properties of the cell [6] .

1.4.2 Micropipette Aspiration

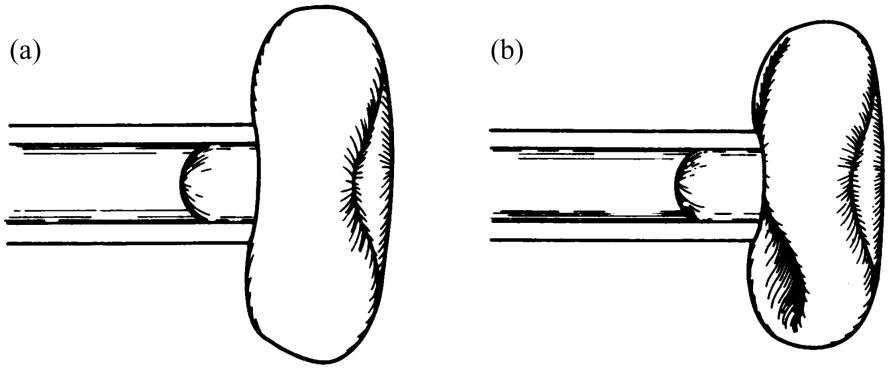

Figure 1.11: A schematic view of red blood cell micropipette aspiration [7]. (a) Measurement of the shear modulus. The cell is aspirated in the dimple region of the cell the projected length in the pipette is measured as a function of the aspiration pressure. (b) Measurement of bending modulus. When the aspiration pressure is sufficiently large the cell creases and buckles. The pressure at which occurs is a measure of the bending modulus.[7]

One of the most established techniques to determine the mechanical properties of the red individual blood cell is micropipette aspiration. By using micropipettes various researchers have been able to extract the area compressibility, bending, shear moduli and also the membrane viscosity. Micropipettes with internal diameters of $\sim 1\,\mu m$ are drawn or pulled from glass capillaries. A negative pressure is applied in the pipette and the membrane of the cell is aspirated into the pipette tip (Figure 1.11).

The area compressibility modulus $K_c = \tau \Delta A / A_0$ where τ is the tension ΔA is the resulting increase in surface area due to τ and A_0 is the initial surface area can be measured by aspirating a osmotically swollen red blood cell [41]. The cell enters the pipette until the portion of the cell outside is a smooth sphere. Increasing the pressure further causes an increase in area since there is no free excess area. Measurement of the tongue length in the pipette and the dimensions of the external portion of the cell gives the total surface area as a function of pressure from which the area compressibility can be calculated. The cell membrane will not allow an area dilation grater than $\sim 3\,\%$ before it ruptures. Using this method corrected for the osmotic volume change Evans and Waugh [42] measured a value for the area compressibility modulus of $0.45\,\mathrm{N}m^{-1}$. The area compressibility modulus is

relativity large and the deformations in the circulation can be considered to take place at constant surface area.

The shear modulus of the red blood cell can be determined by aspirating a small portion of the cell membrane into a pipette with a small internal radius $0.5-0.75\,\mu$m. Measuring the length of the cell tongue L in the pipette at increasing values of applied pressure ΔP allows the shear modulus to be determined. The aspirated region should be from a flat portion of the cell (see figure 1.11) since the theory assumes a flat membrane outside the pipette and that the membrane tension is negligible compared to that at the pipette tip. This yields the following relation [43]:

$$\Delta P = \left(\frac{\mu}{R_p}\right)\left[\left(\frac{2L}{R_p} - 1\right) + \ln\left(\frac{2L}{R_p}\right)\right] \tag{1.28}$$

Since the $\ln(2L/R_p)$ term is small in the range $1 < L/R_p < 4$ a linear approximation of Equation (1.28) can be made to give

$$\Delta P = \left(\frac{\mu}{R_p}\right)\left[\frac{k_1 L}{R_p - k_2}\right] \tag{1.29}$$

where $k_1 = 2.45$ and $k_2 = 0.63$. This relationship can be rewritten as

$$\frac{L}{R_p} = \frac{\Delta P R_p k_1}{\mu} + \frac{k_2}{k_1}. \tag{1.30}$$

The advantage of the linear approximation is the absolute pressure and tongue length are not required just the change in these parameters. Using this approach Waugh and Evans [43] obtained a value of the elastic shear modulus of $6.6 \times 10^{-6}\,\mathrm{N}m^{-1}$. These relationships assume no contribution of bending resistance. The effect of a bending contribution is to reduce the intercept (k_2/k_2) and this can used to determine the bending modulus.

The bending modulus κ can be determined by two alternative methods. Initial aspiration of the cell membrane into the pipette requires a hemispherical deformation of the portion of membrane entering the pipette causing bending of the membrane.

The intercept of the linear approximation above (1.30) gives a measure of the bending resistance of the membrane: the higher the bending resistance the lower the value for the fitted intercept.

Alternatively, when a flaccid red blood cell is aspirated into a small micropipette, the cell projection inside the pipette increases uniformly with increasing suction pressure. At a specific aspiration length the cell membrane buckles and the cell rapidly enters the pipette (Figure 1.11b). The buckling instability occurs because the membrane bending rigidity is not sufficient to prevent deflections normal to the surface. If the shear modulus of the cell was negligible the cell would not buckle and would deform as a vesicle does. If the bending rigidity was negligible membrane would wrinkle and fold immediately upon entry to the pipette.

The critical pressure at which buckling occurs is a function of the bending modulus and the inner and outer radii of the micropipette and is given by a theory developed by Evans [44]. For a micropipette with an outer radius three times its internal radius buckling would occur at value of

$$\frac{\kappa}{\Delta P R_p^3} \sim \frac{1}{135} \tag{1.31}$$

for pipettes with an outer radius six times the internal radius buckling would occur at

$$\frac{\kappa}{\Delta P R_p^3} \sim \frac{1}{55}. \tag{1.32}$$

Using this method Evans [44] obtained a value for the bending modulus of 1.8×10^{-19} J.

1.4.3 Deformation in High Frequency Electric fields

This method was originally suggested by Helfrich [17]. The red blood cell is fixed on to an electrode by an applied electric field and then deformed by increasing or decreasing electric field strength (figure 1.12). The deformations of the cell are

measured by a fast image progressing method enabling accurate measurement of deformations of the order of 50 nm [8]. The force is generated by the Maxwell-Wagner Polarisation effect due to the difference in conductivity of the cytoplasm of the cell and the surrounding medium, typically by an order of magnitude. The experiments are done in the frequency domain in which the cytoplasm of the cell is conductive and the outside medium is not. This means the force can be calculated by familiar electrostatic principles treating the cell as a conducting body in a dielectric field.

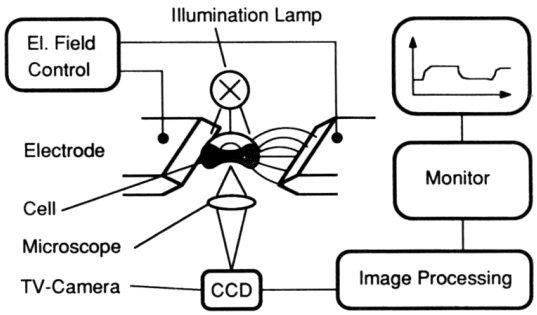

Figure 1.12: Schematic view of the setup for high frequency electrodeformation of red blood cells [8].

The elastic constant is obtained through measurement of the elongation of the cell as a function of electric (Maxwell) tension by applying a triangular pulse with a slow rise time (4 s compared to the response time of the cell ~ 0.1 s). By applying a square wave signal the field strength can rise much faster than the response time of the cell. The membrane viscosity is obtained by measuring the relaxation time of the cell after this rapid deformation. Typical values of the shear modulus μ and membrane viscosity η measured using this technique are $\mu = 6.1 \times 10^{-6}\,\mathrm{Nm}^{-1}$ and $\eta = 3.4 \times 10^{-7}\,\mathrm{Nsm}^{-1}$ [8].

1.4.4 Optical stretcher

An optical stretcher consists of two counter propagating laser beams. Momentum transferred to a cell between the two beams stretches the cell (Figure 1.13). This can be used to determine the elastic properties of the cell membrane. The momentum

transfer occurs because the cell has a higher refractive index that the surrounding medium. Consider a laser incidence on a cell from the front. A small fraction of the light is reflected from the front surface and some momentum is transferred, the rest enters the cell. On the back surface the same fraction is reflected but the light has greater momentum due to the higher refractive index of the cell hence more momentum is transferred to the back surface. The result is a force on the back surface and illumination by two opposing beams results in a stretching of the cell as illustrated in figure 1.13 [9, 45]. This technique has been used to stretch osmotically swollen RBCs producing values for the shear modulus of $(1.3 \pm 0.5) \times 10^{-5}\,\mathrm{Nm}^{-1}$.

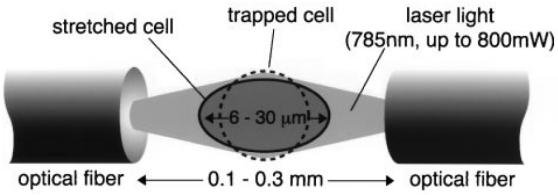

Figure 1.13: Sketch of the Optical Stretcher [9]. The cell is trapped in the middle by the optical forces of the two counter propagating laser beams. The amount the cell is stretched depend upon the laser power and the elastic properties of the cell.

1.4.5 Bead Methods

Another similar technique uses silica beads attached to RBCs as handles and optical laser traps to move the attached beads stretching the cell. A suspension of osmotically swollen spherical red blood cells are incubated with 2.1 µm silica beads in a ratio of approximately two beads per cell and the beads are allowed to non-specifically bind to the red blood cell membrane (Figure 1.14a). Optical tweezers are used to trap the beads and deform the cell. The tweezers allow calibrated force in the pN range to be applied to investigate the viscoelastic properties of the red cell membrane. The measured value of the shear modulus for the red blood cell, obtained with this technique is $\mu = 2.5 \pm 0.4 \times 10^{-6}\,\mathrm{Nm}^{-1}$, approximately half of the value obtained from micropipette techniques [46]. This is attributed to the beads applying point forces to the membrane therefore highly localised stresses and non-linear deformations. Sleep et al. [10] used a very similar technique but used

permeable ghosts and interpreted the results according to the theory by Parker and Winlove [47]. They obtained values for the shear modulus of $2 \times 10^{-6}\,\mathrm{Nm}^{-1}$. A three bead variation of this technique has been used on the free membrane skeleton extracted from the red blood cell [48]. Using this technique it was possible to obtain not only the shear modulus ($\mu = 2.4 \pm 0.7 \times 10^{-6}\,\mu\mathrm{Nm}^{-1}$) but also the area compressibility modulus ($K_c = 4.8 \pm 2.7 \times 10^{-6}\,\mathrm{Nm}^{-1}$). The ratio $K_c/\mu = 1.9 \pm 1.0$ in good agreement with theoretical and numerical predictions for a triangular network of identical springs [48].

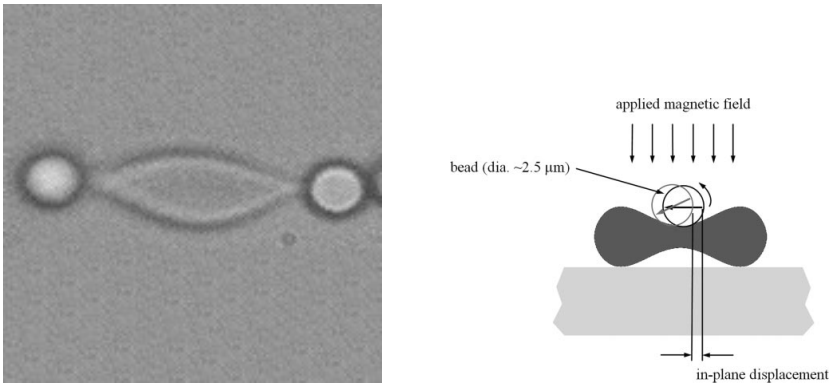

(a) (b)

Figure 1.14: (a) A phase contrast microscope image of a red blood cell with two beads attached. The beads act like handles and are held by laser traps and pulled apart stretching the cell.[10] (b) A schematic the magnetic twisting cytometry technique. A magnetic field is applied to the magnetic bead which generates a torque. This causes it to twist and translate deforming the membrane to which it is bound.[11]

More recently a new technique using magnetic beads has been developed by Puig-de Morales et al. [11]. A functionalised ferrimagnetic microbead (2.5 µm in diameter) is attached to the membrane of a red blood cell and subjected to an oscillating magnetic field. The resulting torque on the bead deforms the cell membrane (see figure 1.14b). The resulting motions of the bead are tracked optically from which the elastic (storage) and frictional (loss) moduli of the cell membrane can be calculated. It was found that the elastic forces dominated and were independent of the frequency, whereas the frictional forces did depend on frequency. The frictional behaviour was non-Newtonian and suggested an origin other that the lipid membrane or the cytosol viscosity. The spectrin network appears to be the prime candidate for the viscous

loss mechanism in the membrane.

1.4.6 Point dark-field microscopy

Point dark-field microscopy involves measuring the fluctuations of the cell edge by focusing light using a dark field microscope arrangement onto a micron sized square spot on the cell edge [49]. The measured variation in intensity is directly related to the displacement of the cell edge. Analysis of such measurements gives the mean height fluctuations, a measure of the viscoelastic properties of the cell membrane. This method has been used in a semi-quantitative way to measure the change in the membrane elastic properties of red blood cells in diabetic individuals with retinopathy. This study showed a significant difference in the membrane fluctuations between normal controls and diabetic individuals with retinopathy, a common complication in long term diabetics [50].

1.4.7 Eigenmode decomposition

In this method the edge fluctuations of the red blood cell are measured to a resolution of 5 nm by combining phase contrast microscopy with fast image processing techniques [51]. Phase contrast microscopy produces strong diffraction halos around the edges of objects. The edge position of the red cell membrane is determined by analysis of the diffraction halo and is defined as a particular threshold value between the minimum and maximum intensity of the halo. The mean square fluctuations of the edge were measured accurately at four equally spaced points around the cell edge and this allowed mode decomposition of first three azimuthal modes ($m = 0, 1, 2$) and the calculation of the corresponding autocorrelation functions (Figure 1.15).

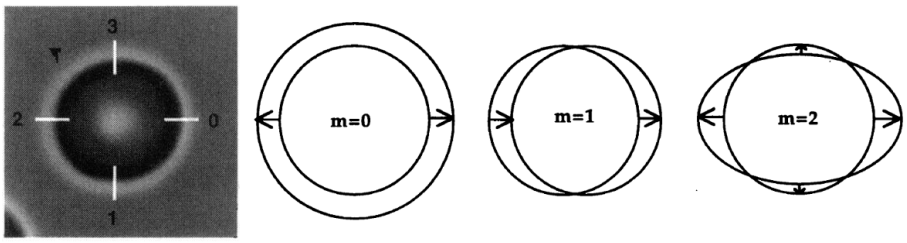

Figure 1.15: Far left is a phase contrast image of a red blood cell showing the four points of measurement from which the azimuthal modes shown on the right $m = 0, 1, 2$ were calculated.

The largest eigenmode (m=1) is the translational mode and this is hindered because the cell is glued to the microscope slide. The theoretical analysis showed that this mode is insensitive to the shear modulus and therefore was used to determine the bending modulus κ of the membrane. Values obtained for the bending modulus covered the range from 2×10^{-19} J to 7×10^{-19} J. The elliptical deformation mode (m=2) was used to determine the shear elasticity as it was shown to be sensitive to the membrane shear modulus. The typical values of the shear modulus μ obtained with this technique were from 0 to $1.6 \times 10^{-7}\,\mathrm{Nm}^{-1}$. This is smaller by a factor of at least 10 from values obtained by mechanical deformation. The small value of the shear modulus and the fact that the values obtained were scattered suggested that thermal fluctuations are essentially shear free.

1.4.8 Reflection interference contrast (RIC) microscopy

The reflection interference contrast (RIC) microscopy method is depicted in Figure 1.16 [12]. Light reflected from the glass plate (the reference beam) interferes with light reflected from the cell surface (the object beam) producing a Newton ring like diffraction pattern due to the cylindrical symmetry of the red blood cell. Two interpretations of the data are made. For long wavelengths the surface profile of the cell can be reconstructed and the difference between two instantaneous surface profiles gives a measure of the surface height fluctuations from which the mean square height fluctuations, $\left\langle \left| U(q) \right|^2 \right\rangle$, can be calculated. For short wavelengths it can be assumed that the resting shape is constant. A direct Fourier transform of the

RIC image is $U(q)$ from which the mean square height fluctuations $\langle |U(q)|^2 \rangle$ can easily be computed. Using the theoretical interpretation of Brochard and Lennon the bending modulus of the cell can be extracted using $\kappa = k_B T/(Sq^4 \langle |U(q)|^2 \rangle)$ where S is the observed surface area. Using this technique the bending modulus was found for normal red blood cells to be $\kappa = 3.4 \pm 0.8 \times 10^{-20}\,\mathrm{Nm}$.

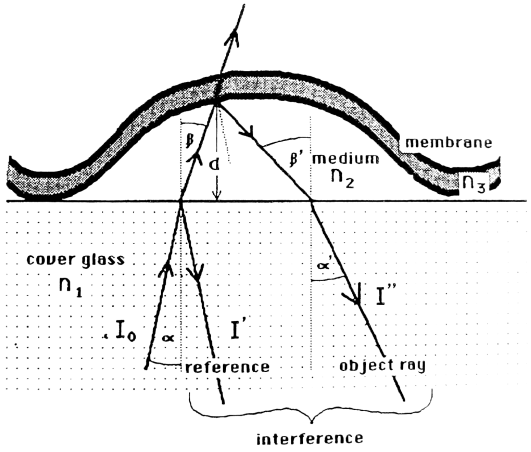

Figure 1.16: Schematic representation of the reflection interference contrast (RIC) microscopy of a red blood cell. I_0 is the intensity of the incident light, I' the intensity of the light reflected form the glass plate and I'' the light reflected from the cell surface [12].

1.4.9 Diffraction phase microscopy

Recently a series of new interferometric techniques have been developed by a group lead by Popescu [52, 53, 54]. The idea is to measure the phase changes in the light passing through the red blood cell using interferometry which in principle is very sensitive to the thickness of the sample ($\sim 1\,\mathrm{nm}$) and hence thermal fluctuations of the membrane. The problem with the interferometry is that it is also very sensitive to external noise from mechanical vibrations and thermal fluctuations which may cause erroneous fluctuations in the path differences between the sample and reference beams. The most successful of these techniques overcame many of these issues by using a common path Mach-Zender interferometer (see figure 1.17). This was achieved by placing a diffraction grating in the image plane and isolating the zeroth and first diffraction orders. Each order contains the full spatial information of the

image and by placing a spatial filter in the Fourier plane the zeroth-order beam is low-pass filtered producing a uniform field at the CCD. The result is that the zeroth-order beam acts as the reference field and the first-order beam as the imaging field and since the two beams have a common path traversing the same optical components the phase noise is significantly reduced.

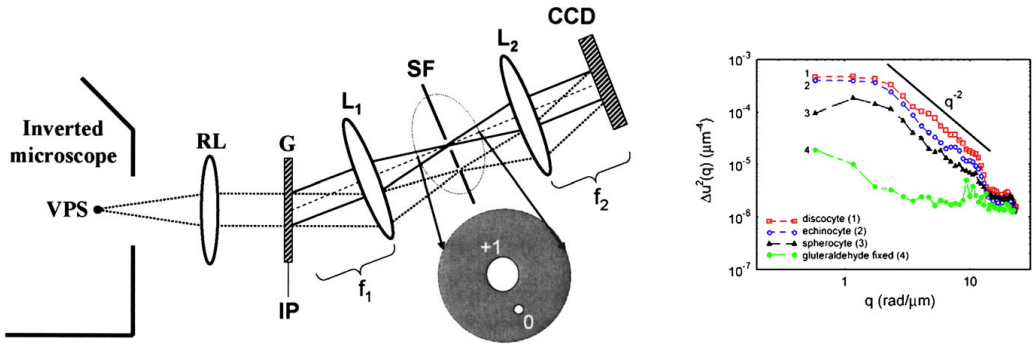

Figure 1.17: Diffraction phase microscopy setup (left) showing the optical arrangement. VPS, virtual source point; RL, A relay lens ; G, grating; SF, spatial filter; IP image plane; $L_{1,2}$, lenses ($f_{1,2}$ respective focal distances). The resultant fluctuation spectra (right) shows cellar differences between normal red cells and echinocytes and spherocytes. The membrane tension σ can be extracted from the q^{-2} section of the spectra.

The thermal fluctuations are then expressed in terms of the mean square displacements of the spatial vector, $\langle |U(q)|^2 \rangle$. By comparing the experimental spectra to the theoretical model by Gov et al. [25] they were able to extract the membrane tension from experimental data on normal discocytes ($\sigma = (1.5 \pm 0.2) \times 10^{-6}\,\mathrm{J/m^2}$), echinocytes ($\sigma = (4.05 \pm 1.1) \times 10^{-6}\,\mathrm{J/m^2}$) and spherocyte cells ($\sigma = (8.25 \pm 1.6) \times 10^{-6}\,\mathrm{J/m^2}$).

1.4.10 Summary

Below is a table summarising the results obtained with the techniques described above. There are orders of magnitude separating the values of the elastic moduli obtained from the different techniques described. For example the shear modulus (μ) varies from zero to $1.3 \times 10^{-5}\,\mathrm{Nm^{-1}}$. For large deformation experiments like

micropipette aspiration and the optical stretcher the measured values of the shear modulus are large $\sim 10^{-6}\,\mathrm{Nm}^{-1}$ whereas for the fluctuation experiments the shear modulus is vanishingly small. The bending modulus also appears to have a large variation in the measured value between the different techniques. This appears due to the length-scale on which it is measured; micropipette aspirations and the eigenmode analysis technique measure the bending modulus at deformations comparable to the cell size and have large values, of up to $7 \times 10^{-19}\,\mathrm{J}$ whereas the thermal fluctuation techniques measuring small deformations such as RIC microscopy report smaller values of the order $10^{-20}\,\mathrm{J}$.

Technique	Author	Results
Micropipette aspiration	Evans et al. [41] Evans [44] Waugh and Evans [43]	$\mu = 6.6 \times 10^{-6}\,\mathrm{Nm}^{-1}$ $\kappa = 1.8 \times 10^{-19}\,\mathrm{J}$ $K_c = 0.45\,\mathrm{Nm}^{-1}$ †
Electrodeformation	Engelhardt and Sackmann [8]	$\mu = 6.1 \times 10^{-6}\,\mathrm{Nm}^{-1}$
Optical Stretcher	Guck et al. [9]	$\mu = 1.3 \times 10^{-5}\,\mathrm{N}m^{-1}$
Optical Tweezers (2 beads)	Sleep et al. [10] Hénon et al. [46]	$\mu = 2.5 \times 10^{-6}\,\mathrm{Nm}^{-1}$
Optical Tweezers (3 beads)	Lenormand et al. [48]	$\mu = 2.4 \times 10^{-6}\,\mathrm{Nm}^{-1}$ $K_c = 4.8 \times 10^{-6}\,\mathrm{Nm}^{-1}$ ‡
Eigenmode fluctuations	Strey et al. [51]	$\mu = 0 - 1.6 \times 10^{-7}\,\mathrm{Nm}^{-1}$ $\kappa = 2 - 7 \times 10^{-19}\,\mathrm{J}$
Reflection Interference Microscopy (RIC)	Zilker et al. [12]	$\kappa = 3.4 \times 10^{-20}\,\mathrm{J}$
Diffraction phase microscopy	Popescu et al. [54]	$\sigma = 1.05 \times 10^{-6}\,\mathrm{Jm}^{-2}$

Table 1.1: Summary of values of the elastic constants of red blood cells obtained using the techniques described above. μ is the shear modulus, κ is the bending modulus, K is the area compressibility modulus and σ is the membrane tension. † is the area compressibility of the whole membrane including the lipid bilayer, whereas ‡ is the area compressibility of just the free cytoskeleton excluding the lipid bilayer.

It is clear from the discussion above that there exist many techniques to investigate

the mechanical properties of the red blood cell membrane. In spite of this the empirical techniques of filtration and ektacytometry are still by far the most popular to investigate the biochemical and clinical implications of the mechanical properties of the red cell. Although many of the techniques listed have been applied to clinical problems this is usually done by the authors who developed them and not generally by the wider clinical and biochemical community.

A number of reasons may contribute to this rather limited utilisation. Generally these techniques require access to specialised/expensive kit or knowledge and or are difficult and very time consuming to implement. There is certainly room for a new technique which is easier to implement and provides more information about the mechanical properties with greater reliability.

There is also a gulf of knowledge between the theoretical mechanics of the red blood cell membrane and the practical measurement. Many new theoretical advances are yet to the implemented or tested by experiment. Certainly much of the fluctuations analysis of experimental data does not extend beyond the theoretical models of Helfrich [17] and Brochard and Lennon [55].

1.5 Red cell mechanical properties and disease

In normal physiology the primary role of the red blood cell is to exchange oxygen and CO_2 between the lungs and the tissues. The link between red cell deformability and the ability of the red cell to perform this primary function has long been well established and has been seen in numerous physiological conditions and diseases including diabetes, malaria, hypertension, atherosclerosis, alcoholism, high altitude sickness, sickle cell, Alzheimer disease, sepsis, trauma and shock. In recent years it has also become apparent that the red cell is not just a transporter of oxygen, but a sensor and modulator of vascular tone [56].

A mechanism of modification of the cell membrane in many for these abnormal conditions is through increased oxidative stress. Oxidative damage to spectrin leads

to vesicle formation due to the unsupported lipid bilayer [57, 58]. In diabetic patients the combined effects of oxidative stress and glycation have been shown to decrease deformability of the cell through modification of the membrane structures [59]. There is strong evidence suggesting these modifications lead to complications such as diabetic retinopathy, the leading cause of blindness in the industrialised world.

Currently nearly all medical studies on the red blood cell mechanical properties focus on the deformability of the cell as a whole, using ektacytometry or laser diffraction methods. While useful, these techniques provide limited information about the mechanical properties of the red cell and are unable to distinguish between the contributions of lipid bilayer and the membrane skeleton.

1.6 Outline of Thesis

The main focus of this project was to develop a new technique to measure the mechanical properties of the red blood cell membrane from its thermal fluctuations. The development of the technique is described in Chapter 3. Chapter 4 goes on to show how the analysis of real red blood cells can be compared to simulated cells and how direct comparison of the two can extract the mechanical properties of the red blood cell. The chapters which follow discuss the practical applications of the technique to study effects of modifying the membrane. Chapter 5 the effects of oxidation of the membrane structure and Chapter 6 the effect of glycation and diabetes.

Chapter 2

Red blood cell fluctuation analysis

2.1 Introduction

Experimental measurements of the membrane bending modulus have given values differing by up to an order of magnitude [51]. Similarly, the shear modulus was found, using different experimental techniques, [51, 60] to range from vanishingly small up to $10^{-5}\,\mathrm{Nm}^{-1}$. It is possible that the discrepancies in the values obtained reflect a dependence of the membrane elastic properties on the length scale over which the deformation occurs and/or the magnitude of the applied strain. For example, analysis of the RBC thermal fluctuations [51] (i.e. at small deformations) suggest that the membrane skeleton is essentially stress free with $\mu \approx 0$, whereas the larger deformations incurred during micropipette aspiration [43] ($\mu = 6.6 \times 10^{-6}\,\mathrm{Nm}^{-1}$), in optical tweezers experiments [46, 61, 62] ($\mu \approx 2.5 \times 10^{-6}\,\mathrm{Nm}^{-1}$, $\mu \approx 3.3 \times 10^{-6}\,\mathrm{Nm}^{-1}$) or in shear flow experiments [60] ($\mu \approx 10 \times 10^{-6}\,\mathrm{Nm}^{-1}$) suggest higher shear stiffness. This implies a non-linear response of the membrane skeleton with respect to shear deformation. Evaluations of the bending modulus based on Brownian flicker analysis similarly seem to suggest a separation in the values of κ depending on the length scale at which the thermal fluctuation is examined. For wavelengths smaller than the overall RBC size [12, 63, 25, 64], $\lambda < R$, the bending rigidity is found to be of the order of $10^{-20}\,\mathrm{J}$, up to an order of magnitude smaller

than the values obtained in the $\lambda \sim R$ regime [51, 65]. The reasons for this separation are not entirely clear, and may partly be due to the theoretical approximations used for the interpretation of the experimental fluctuation spectra.

Recent years have seen significant progress in addressing important questions such as the contribution of non-linear elasticity to RBC shapes, [24] the effects of skeleton-induced tension, confinement [25] and spectrin mesh size [64] on the membrane thermal fluctuation spectrum, as well as producing diverging views on the role of ATP dependent active membrane fluctuations [66, 35, 10]. Despite this, advances in the experimental methods to measure the thermal fluctuations and quantify the red cell elasticity have been relatively few [54, 67]. This arises because while short wavelength fluctuations ($\lambda \ll R$) are relatively easy to interpret, using flat-membrane approximations [55] , they are difficult to measure. In contrast the measurement of long wavelengths is more accessible but the theoretical interpretation is difficult and beyond a purely analytical approach.

Experimentally, the proposed method analyses the thermal fluctuations of a 2D contour of the RBC and uses it to derive the membrane elastic constants by comparing the contour fluctuations to those derived from a coarse-grained particle dynamics simulation of the whole cell.

Full contour analysis techniques have been successful applied to vesicles [5, 29] but limited progress has been made applying this approach to the red blood cell [68, 51]. The advantage of the full contour analysis is that it gives the fluctuation spectrum across all accessible wavelengths. Analysis of the fluctuation spectrum should enable the extraction of the shear (μ) and bending (κ) elastic moduli and the membrane tension (σ).

The main topic of this chapter is the development of the red blood cell fluctuation technique. Discussed is the experimental procedure, contour extraction procedures, and the Fourier analysis of the fluctuating contours, followed by experimental verification of the method by investigating the effects of temperature and osmolarity.

2.2 Experimental method

Fresh blood samples were collected from healthy volunteers by pin pick lancet (Acc-Chek, Roche Ltd). The small volume, $\sim 5\,\mu$l, was immediately suspended in 1 ml of phosphate buffer saline (PBS) (Oxoid Ltd, Basingstoke, UK) with 1 mg/ml bovine serum albumin (BSA) (Sigma-Aldrich, United Kingdom). We chose to work with a simple buffer as it preserves the cell shape while minimising any interaction with the cell membrane, which is an important consideration for the measurement of the membrane mechanical properties. The buffer was adjusted to pH 7.4 and had an osmolarity of 290 mosmol, ensuring the cells maintain their discoid shape. The BSA content inhibits the 'glass effect', a poorly understood phenomenon in which red blood cells change shape in contact with the glass of the microscope slide and form echinocytes.

Suspended cells were placed in an open-sided observation chamber. The observation chamber is a microscope slide with coverclip spaced apart by two strips of Parafilm (Pechiney Plastic Packaging, USA) along the long edges of the slide, bonded together by heating briefly on a hot plate. This chamber allows the exchange of the buffer solution by placing excess solution on one side of the chamber and 'pulling' it through with tissue or filter paper introduced to the opposite side.

2.3 Contour extraction

RBC fluctuation amplitudes are of the order of 10 s of nanometres compared to micrometres for giant vesicles. RBCs are also significantly smaller than giant vesicles, about $6 - 8\,\mu$m in diameter compared to $\sim 50\,\mu$m for vesicles. The size of the cell means the halo and fade-off artifacts in the phase-contrast microscopy are more significant and combined with the small fluctuations make accurately tracing the cell contour and measuring the fluctuations more difficult. Therefore, in order to apply this technique to RBCs significant improvements need to be made to the imaging and contour extraction procedure.

2.3.1 Imaging

The fluctuations of the red blood cells were observed using phase-contrast microscopy (Leica DMLFS upright microscope equipped with a 63×PL FLUOTAR phase contrast objective). The slight difference in the density of the red blood cell and the surrounding buffer stabilises the cells at the bottom of the observation chamber. Video of the fluctuating red cells was taken using a Moticam 2000 (Motic, China) digital microscope camera with a 2 MegaPixel CMOS sensor and USB 2 connection. This was connected to a standard Desktop PC (P4 Dell).

Typically a video of the fluctuating cell is 40 seconds long at a rate of 40-60 frames per second giving 1500-2500 frames in total. The camera records the video to an uncompressed AVI file (Audio Video Interleave) directly to the computer hard drive. Working with the recorded video has the advantage that more computationally intensive contour extraction techniques can be used and therefore the higher frame rates can be exploited.

The computer program to extract the contours from the video was written in Java as a plugin for the open source image processing package ImageJ [69]. ImageJ has an user interface, file handling for uncompressed video, data structures for accessing image data and a built in Java compiler.

2.3.2 Edge determination

A typical frame from a video of a fluctuating red blood cell is shown in Figure 2.1. Phase-contrast microscopy has associated image artifacts, a dark band and light halo around the edges of objects where the refractive index changes. This means it is difficult to define the exact position of the edge.

In order to trace the contour the edge needs to be defined. Previously the edge has been defined by the point at which the intensity gradient is greatest between the dark band and the halo [22], by a point across this band which intersects the mean

intensity of the background and also by the point of minimum intensity in the dark band [70, 71].

The precise criterion used to define the cell edge makes no significant difference in measuring the fluctuations, as long as the same feature is traced consistently with high precision. The minimum of the dark band is the most appropriate choice for the red cell since the contrast between the cell cytosol and the background is much less than in vesicles and the minimum is expected to be less sensitive to noise.

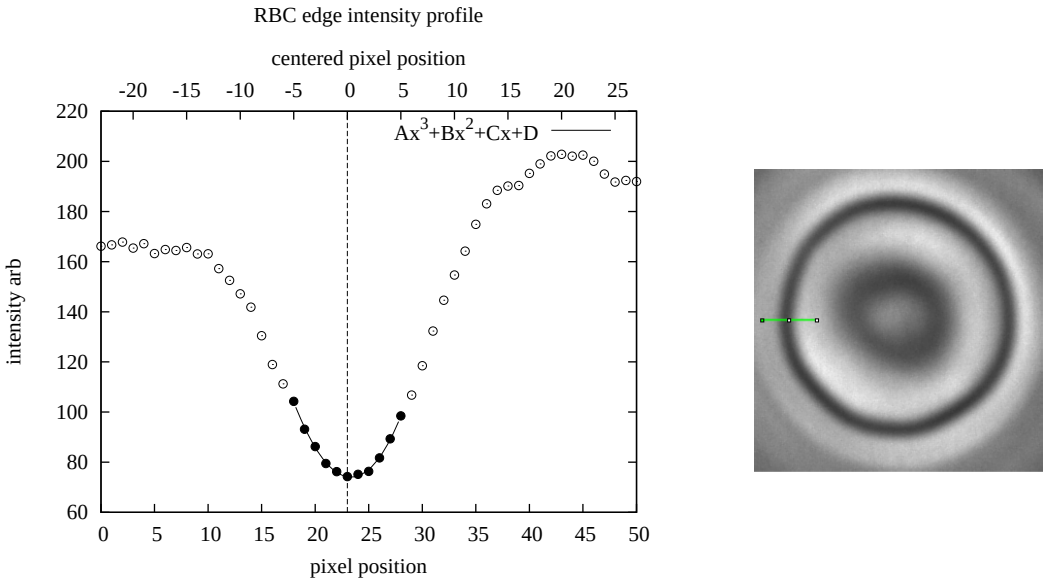

Figure 2.1: (a) Intensity profile across membrane. The solid circles indicate the points used to fit cubic polynomial which is shown as the solid line. The top axis shows the coordinate system with reference to the fitting algorithm. (b) Phase contrast image of red blood cell. The intensity profile in (a) is that for the green line shown. (Scale 30 px = 1 µm)

The process of extracting each point of the contour to subpixel resolution is as follows. First the program scans across the dark band finding the pixel of minimum intensity. This is defined as the zero position along the scan direction for the subpixel algorithm. The algorithm takes 5 pixels either side of the zero position and fits a cubic polynomial using the method of least squares [72, 73] (Figure 2.1). It then searches for the minimum of the polynomial closest to the zero position using the Newton-Raphson method [72] and the solution is defined as the cell edge.

This process of fitting cubic polynomials is computationally intensive and can be sped up by considering the pixel minimum to be at position zero and the pixels intensities either side to be at positions -5 to 5. This considerably simplifies the least-square fitting procedure of the cubic polynomial, since the matrix inversion involved in solving the simultaneous equations can be reduced to a series of multiplications [73]. The sum of the solution of the minimum and the pixel position in the original image coordinates gives the subpixel coordinate of the contour.

2.3.3 Tracing algorithm

The video AVI file is loaded into ImageJ and the stack converted to 8-bit grayscale by deleting the red and blue channels leaving just the green channel. The red and blue channels are discarded since the blue is strongly absorbed by the haemoglobin in the red cell and the signal to noise in the red channel in low due to the infrared filter in front of the imaging sensor. A rectangular region of interest drawn around the cell defines the bounds of the red blood cell to be traced by the plugin. The tracing procedure is then started.

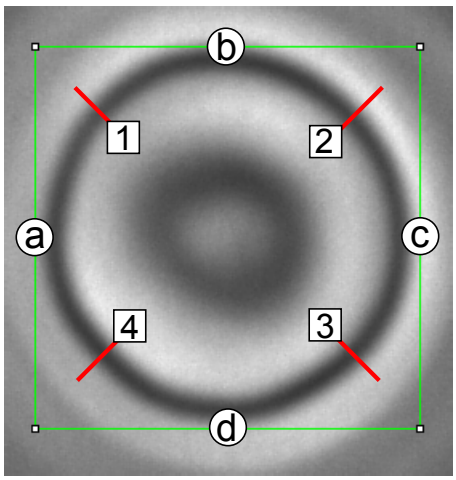

Figure 2.2: The search pattern of the contour tracing algorithm. (a) is the start point and finish point. The red lines points 1-4 indicate the point at which the algorithm switches from scanning the image horizontally to vertically.

The algorithm first finds the contour top, bottom, left and right limits (Figure 2.2 *a-d*) by scanning across from the midpoint of the rectangular selection box in each

direction looking for the point of minimum intensity. Once identified, the points (*a-d*) set the search pattern for the algorithm. The algorithm is designed to scan each pixel line in a direction close to the normal of the recorded contour (Figure 2.2). This means that between the pair of positions (*1-2*) and (*3-4*) it scans the frame vertically, whereas between positions (*4-1*) and (*2-3*) the scanning is along the horizontal direction. This is implemented in order to avoid errors in detecting the contour position when the search direction is nearly collinear with the contour e.g. if the contour is sought in a horizontal direction around point (*b*). The x and y coordinates for the complete contour are then saved to a text file. The procedure is then repeated for all frames of the video file using the previous frame's coordinates as initial guesses. This allows the plugin to account for cell movement. Figure 2.3 shows a typical contour extracted in this way overlayed the corresponding video frame.

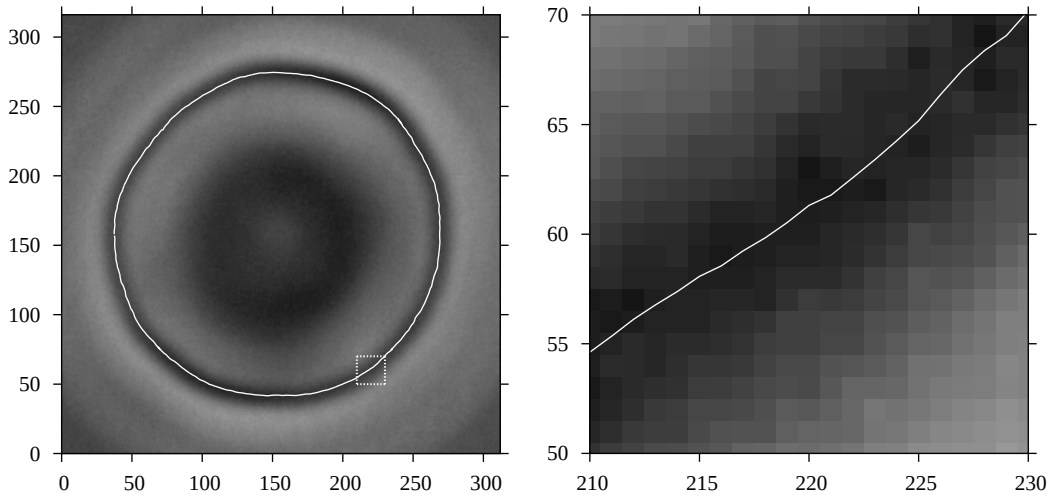

Figure 2.3: (left) A frame from a video of a fluctuating red blood cell with the corresponding extracted contour overlayed. (right) An enlargement of the area indicated in the left image showing the subpixel tracing of the contour. (Scale 30 px = 1 µm)

The result from the contour extraction procedure is a text file with the x and y coordinates of all the contours of a particular video file. This is then used as the input data for the Fourier analysis and radial fluctuation analysis programs described below.

2.4 Fourier Analysis

The Fourier analysis of the contours follows a standard method as used in the analysis of the contours of quasi-spherical [29] and elliptical vesicles [5].

Each coordinate of the contour was converted into polar coordinates with respect to the contour centre of mass, to eliminate any effects of either cell movement or microscope vibration. A Fourier series of the form (2.1) is fitted to each contour, where a_n and b_n are the Fourier amplitudes and r_0 is the mean radius of the red cell contour.

$$r(\theta,t) = R_0(t)\left\{1 + \sum_{n=1}^{\infty}[a_n(t)cos(n\theta) + b_n(t)sin(n\theta)]\right\} \tag{2.1}$$

The time dependence of the Fourier amplitudes $a_n(t),\ b_n(t)$ encodes all the essential information about the shape fluctuations of the contour.

The mean values of the parameters, extracted by fitting equation (2.1) to a set of experimental contours, $\langle R_0\rangle$, $\langle a_n\rangle$ and $\langle b_n\rangle$, describe the mean contour shape (Figure 2.4). It can be seen that if $\langle a_n\rangle = \langle b_n\rangle = 0$, the mean shape is a circle of radius $\langle R_0\rangle$. In all practical cases however , we observe a deviation of the mean shape from circular, i.e. at least for some of the modes $\langle a_n\rangle$ or $\langle b_n\rangle \neq 0$. To characterise the contour elasticity, therefore, it is necessary to define the contour fluctuations around the mean shape. This situation is illustrated by figure 2.5, where the time dependence of two modes (a_3 and a_{11}) is shown. In this case $\langle a_{11}\rangle \simeq 0$, but $\langle a_3\rangle$ is negative suggesting that the mean shape of the contour is not circular.

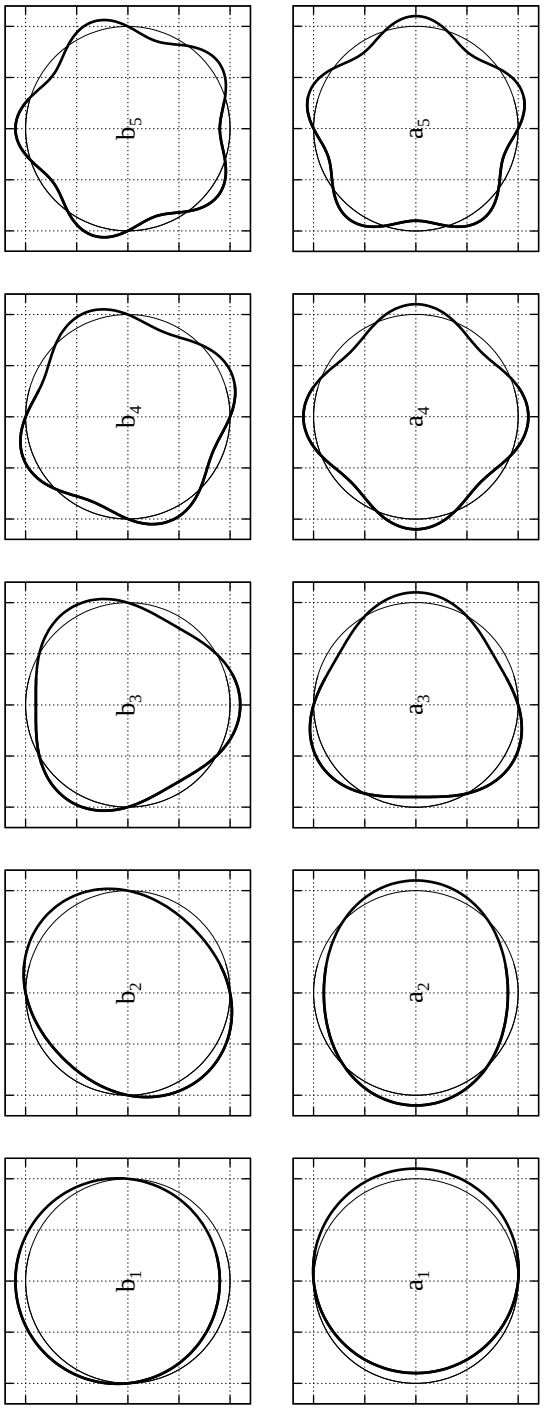

Figure 2.4: Shape deformations corresponding to the first five Fourier modes of equation (2.1). The shapes produced by a_n and b_n differ by $\pi/4$ rotation.

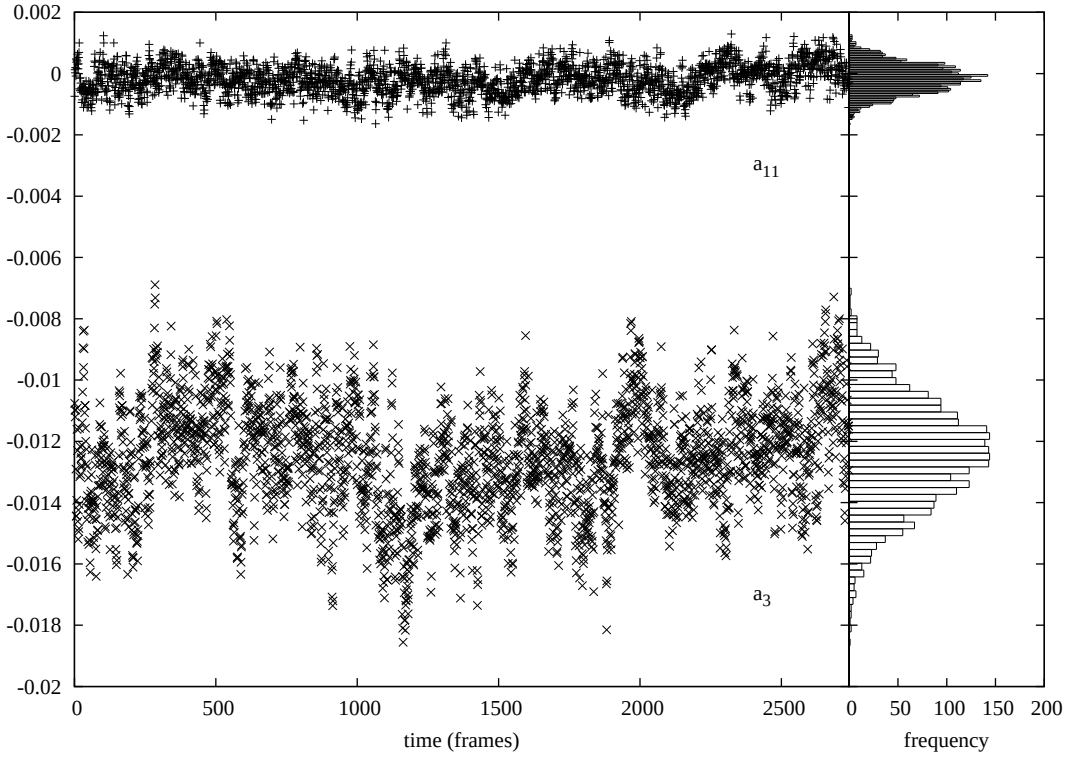

Figure 2.5: Typical distribution of the Fourier coefficients. Here are shown the time trends of the Fourier coefficients a_3 and a_{11}.

Figure 2.5 clearly shows that the fluctuation amplitudes of the high mode a_{11} is significantly less than that of a_3. It is important to note that there is structure in the fluctuations of modes, particularly for the low modes as seen in a_3. This highlights that in order to obtain a statistically meaningful mean it is important to record the fluctuations for long enough to explore the modes fully. An estimate of the fluctuation lifetime τ_n of the modes can be obtained from $\tau_n = \eta_c \lambda_n^3 / \kappa$ [55], where η is the viscosity of the red cell cytoplasm, κ the bending modulus and λ_n the wavelength at mode n. For the longest wavelength mode $n = 2$ using $\eta_c = 6 \times 10^{-3}\,\mathrm{Pa{\cdot}s}$ and $\kappa = 10^{-19}\,\mathrm{J}$, the a fluctuation lifetime is $\tau \approx 10\,\mathrm{s}$. The modes also show a normal distribution around a constant mean value (Figure 2.5), suggesting a period 40 s of recording is sufficient to describe the statistics of the modes.

The contour shape fluctuations around the mean shape can then be quantified by the mean square values of the amplitudes for each mode n, $\langle \delta_n^2 \rangle = \left[\langle a_n^2 \rangle - \langle a_n \rangle^2 \right] + \left[\langle b_n^2 \rangle - \langle b_n \rangle^2 \right]$, as in the analysis of fluctuating vesicles [74].

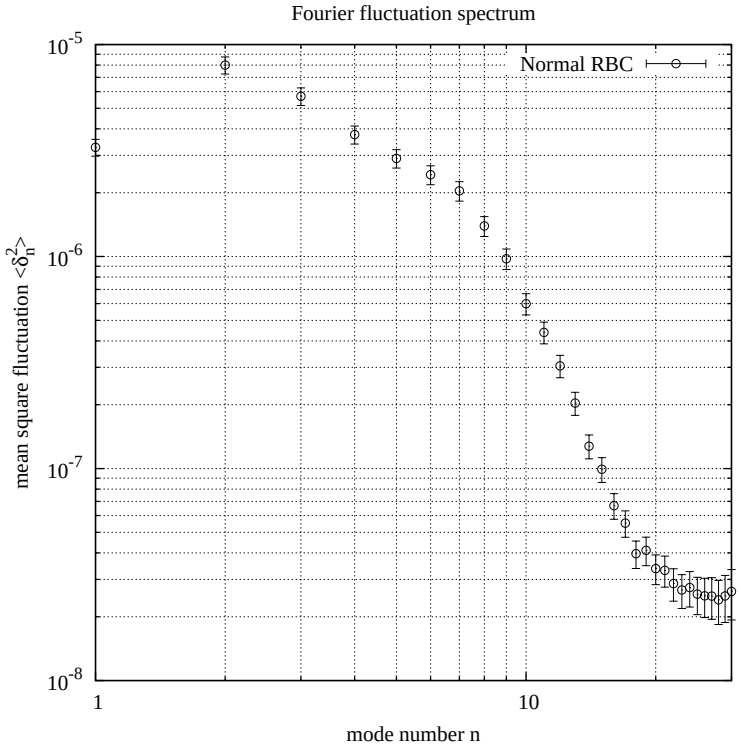

Figure 2.6: Typical spectrum obtained from the Fourier analysis of the contours of a normal RBC. The error bars show the rms for 10 observations of the same cell.

A typical fluctuation spectrum for a normal cell is shown in Figure 2.6. As expected, the mean square fluctuations drop for increasing mode numbers n. For intermediate values of n (between 7 and 18) there appears to be a power-law dependence. For lower mode numbers ($n \leq 6$) the mean square amplitudes deviate progressively from this scaling. This deviation originates from the closed topology of the membrane and has already been comprehensively analysed for the long-wavelength modes of lipid vesicles [29]. In addition, this part of the spectrum could be affected by constraints reflecting the composite nature of the RBC membrane (i.e. a lipid bilayer coupled to a spectrin mesh) through skeleton-induced membrane tension and, importantly, suppression of bilayer fluctuations due to the confining effect of the membrane skeleton [25] (which, in turn, is related to its shear modulus, μ); the latter is expected to have a stronger effect on the longest wavelength modes [25]. The uncertainties shown in Figure 2.6 are typical and for clarity are omitted from future graphs of the mean square fluctuations $\langle \delta_n^2 \rangle$.

The ability to detect short wavelength fluctuations using this optical method is fundamentally limited by the optical resolution, camera noise and fluctuation lifetimes of the short-lived high frequencies [29] (the fluctuation lifetime for the bending-dominated part of the spectrum scales with the cube of the wavelength, $\tau_n = \eta_s \lambda_n^3 / \kappa$). With the current system short wavelength modes, $n \geq 18$, cannot be detected reliably.

2.5 Edge displacement histogram

The edge displacement histogram is an alternative way to analyse the fluctuations of red blood cell contours. This analysis does not provide more information about the fluctuations but does provide a more sensitive measure of the overall fluctuations.

The process of analysis is as follows. Starting with a series of contours centred around their centre of gravity, the radius at fixed angles, $r(\theta)$, is calculated by determining the point of intersection between a line from the centre of gravity at an angle θ and the contour. These are then normalised to the mean radius at that angle $\langle r(\theta) \rangle$. The normalised radii $r(\theta)/\langle r(\theta) \rangle$ for all angles are combined into one histogram describing the fluctuations of the mean radius.

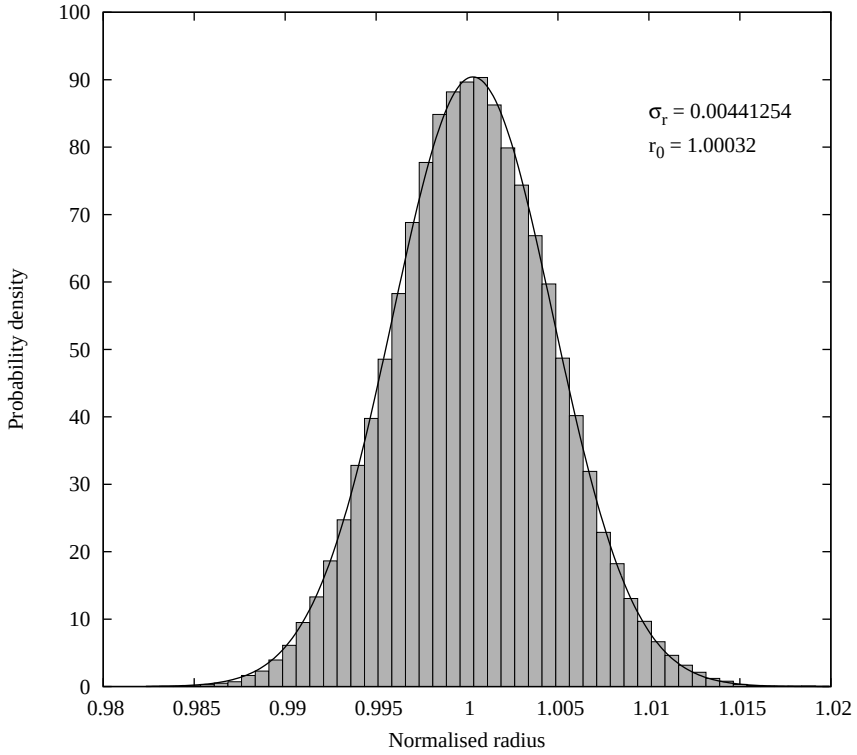

Figure 2.7: Histogram curve fitted with a normal distribution, fitting parameters σ_r standard deviation of the radius and r_0 the mean radius.

A normalised histogram of the fluctuations in the instantaneous radius of the contour for a normal red blood cell is shown in Figure 2.7. The calculation is performed over all contours in the sample for 360 values of the polar angle θ.

The resulting histogram is fitted with the probability density function for a normal distribution of the form

$$p(x) = \frac{1}{\sigma_r\sqrt{2\pi}} \exp\left(-\frac{(r-r_0)^2}{2\sigma_r^2}\right) \tag{2.2}$$

where σ_r is the standard deviation and r_0 is the mean radius. As shown in Figure 2.7 the fluctuations in the radius are clearly normally distributed. The overall degree of fluctuations is given by σ_r. Since this is a very sensitive measure of the overall degree of fluctuations, the parameter σ_r can be used to detect changes in membrane stiffness.

2.6 Method validation

Presented below is a set of experiments done to verify that the thermal fluctuations of the red blood cell membrane were responsible for the spectrum observed and that changes in the red blood cell elasticity can be observed using this technique.

2.6.1 Gas bubble test

A gas bubble provides an essentially rigid test object to compare the red blood cell fluctuations to and find the limits of measurement of the technique. A gas bubble with a diameter of 8 µm was recorded and analysed in the same way as a red blood cell. The gas bubble was created by trapping air in water between a microscope slide and a coverslip.

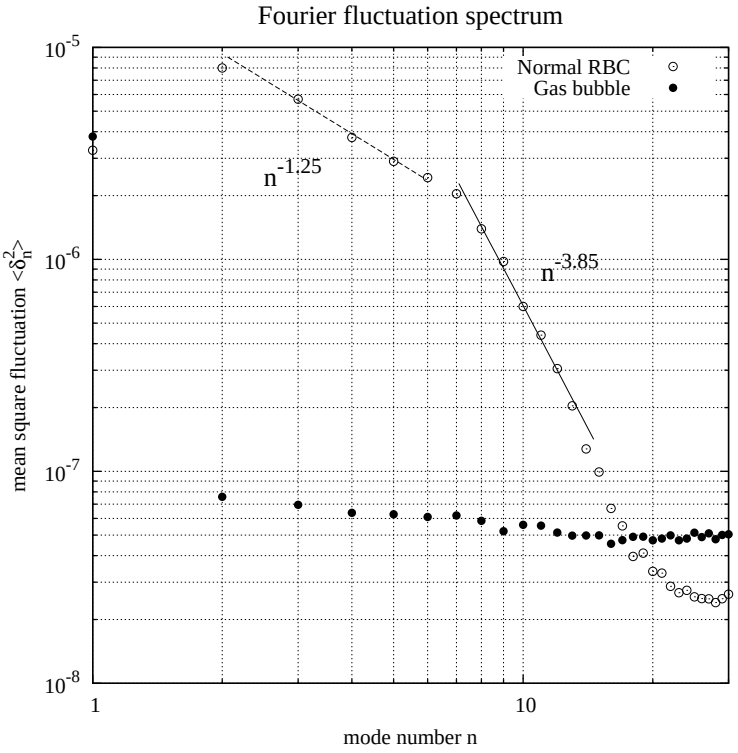

Figure 2.8: Fluctuation spectra of a red blood cell (hollow symbols) and a gas bubble (solid symbols). With n^x fittings for low modes ($n < 6$) dashed line and high modes ($n > 6$) solid line.

The fluctuation spectrum of the gas bubble was calculated and compared to that of

a typical red blood cell. Figure 2.8 clearly shows that the difference is significant. The recording of the gas bubble had noticeably less contrast than the red cell image and this accounts from the large apparent fluctuations for high modes $n \geq 18$. This demonstrates that the RBC fluctuations are responsible for the mode dependence observed in RBC fluctuation spectra.

2.6.2 Variation in Normal Cells

Using the procedure described earlier (Section 2.2), the fluctuations were recorded for 141 RBCs from healthy individuals with no known metabolic or circulatory disorders and the fluctuation spectra and edge displacement histograms were calculated. All the fluctuation spectra from the recorded cells feature the traits seen in Figure 2.6.

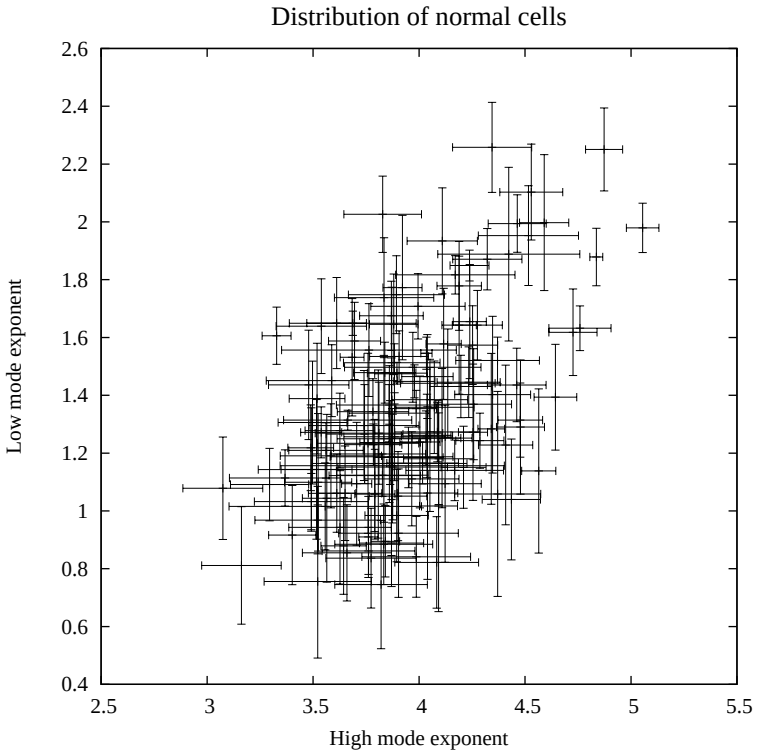

Figure 2.9: Distribution of the exponents of the the high mode dependence $7 \leq n \leq 18$ against the low mode dependence $n < 6$, for 141 normal cells.

In order to obtain a measure for the variation between the fluctuation spectra,

power laws were fitted to the low mode number region ($n \leq 6$) and the high mode number region ($7 \leq n \leq 18$) for all the cell spectra (Figure 2.8). Figure 2.9 is a plot of the exponents of these powers laws for the high mode number region against the exponent of low mode number region, for all cells in the sample. In the high mode region the fluctuation dependence was $\langle \delta_n^2 \rangle \propto n^{-3.95 \pm 0.36}$, which suggests that this part of the fluctuation spectrum is dominated by bending. For lower mode numbers ($n \leq 6$) the mean square amplitudes deviated progressively from this scaling, $\langle \delta_n^2 \rangle \propto n^{-1.34 \pm 0.33}$, suggesting an influence of the membrane skeleton and or the closed topology of the cell.

The standard deviation σ_r of the edge displacement histogram, for 141 cells is shown in Figure 2.10. The standard deviation varies as $\sigma_r = (5.0 \pm 0.5) \times 10^{-3}$ across the population of cells.

Figure 2.9 and 2.10 demonstrate a degree of variability in the membrane elastic properties within the cell population. This suggests that subtle differences in the membrane mechanical properties may be observed, making the investigations of a cell population response less reliable. In studying the effects of modifications of the cell on its mechanical properties, this undesirable effect can be avoided by performing single cell studies, i.e. monitoring the changes of a particular cell with respect to its own initial state. This is the approach in the rest of the work reported in this thesis.

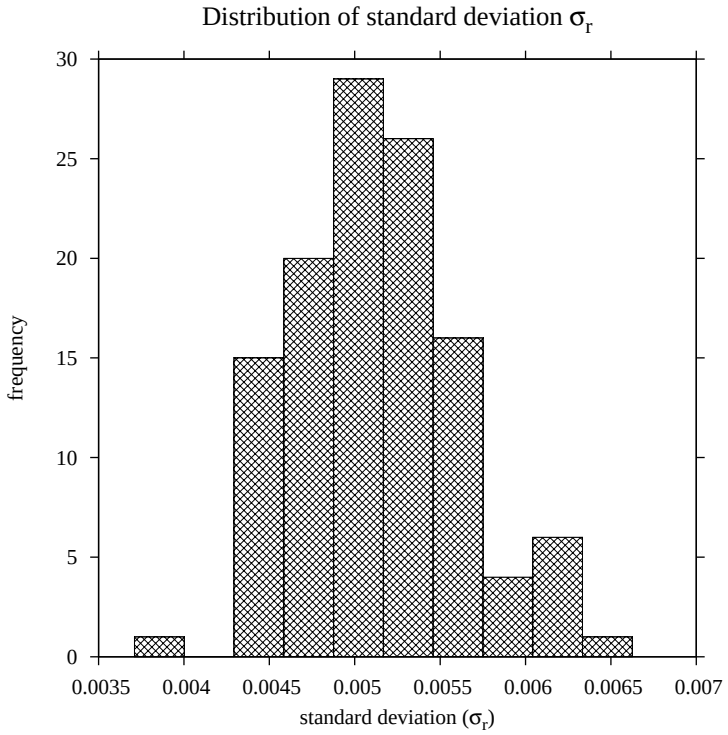

Figure 2.10: Distribution of histogram standard deviation σ_r for 141 cells

2.6.3 Effect of Temperature

The only other parameters other that the mechanical properties of the membrane which enter into the theoretical calculations of the thermal fluctuations of the membrane are temperature and excess area.

For the investigation of the temperature effects, red blood cells samples were prepared using the procedure described previously. The observation chamber was sealed with wax to prevent evaporation of the sample. Individual cells were observed and the fluctuations recorded while increasing the temperature using a temperature controlled stage.

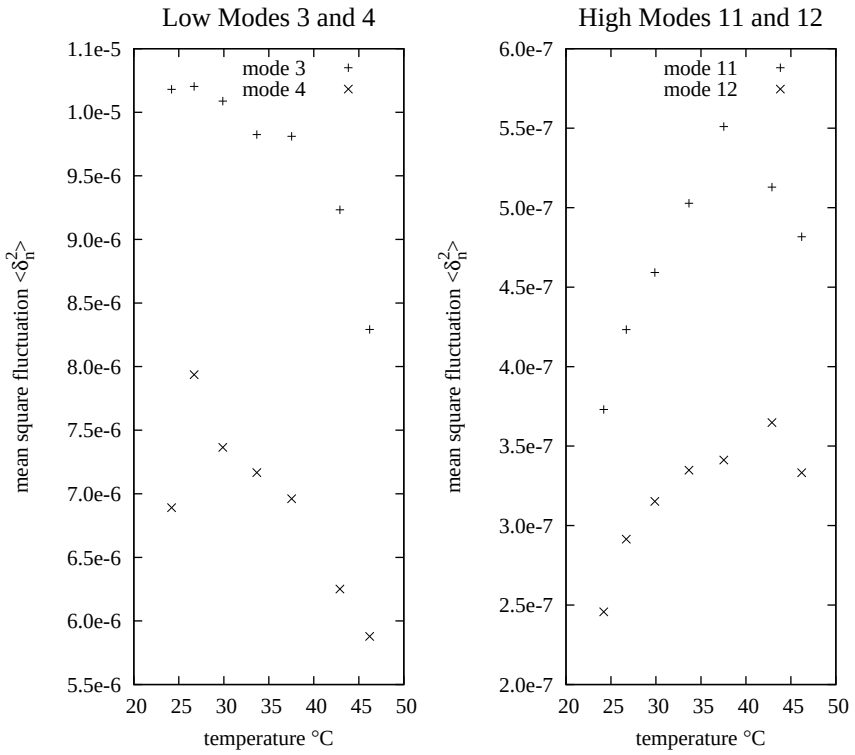

Figure 2.11: The temperature dependence of the low modes (the long wavelength fluctuations $\sim 8\,\mu m$) and the high mode (the short wavelength fluctuations $\sim 2\,\mu m$)

Figure 2.11 shows the temperature dependence of the mean square fluctuations of two modes ($n = 3, 4$) of the low-mode region and two modes ($n = 11, 12$) from the high mode region. As can be seen from the figure, for $n = 3, 4$ $\left\langle \delta_n^2 \right\rangle$ decreases with temperature, whereas for $n = 11, 12$ $\left\langle \delta_n^2 \right\rangle$ increase with temperature. whilst at first sight this maybe surprising, the reason for such a trend maybe found in the sensitivity of the different modes to different membrane properties. For $n \geq 7$, the fluctuations are controlled predominately by bending. Assuming that the bending modulus has only a weak dependence on the temperature [75, 71], one can expect a linear increase of $\left\langle \delta_n^2 \right\rangle$ with temperature according to equation (1.20). This is in agreement with figure 2.11.

Whilst such an effect must also affect the lower modes (Figure 2.11), the experiment suggests a mechanism that not only compensates, but reverses the low mode fluctuations temperature dependence: the increase of temperature suppressing the fluctuations of the first several modes. The most probable explanation of this ef-

fect is in the composite nature of the RBC membrane, consisting of a lipid bilayer coupled to a membrane skeleton. The relatively rigid membrane skeleton in close proximity to the lipid bilayer suppresses its longest wavelength fluctuations. This has theoretically been modelled by the use of a confining potential [25] introduced in the elastic free energy function. The confining potential has its greatest effect on the long-wavelength part of the fluctuation spectrum, and is temperature dependent, $\gamma = (k_B T)^2/\kappa d^4$, where d is the mean distance between the lipid bilayer and the skeleton mesh. An increase in temperature will increase γ, thus suppressing the first several modes, as observed in figure 2.11. This interpretation suggests that the recorded contour fluctuation spectrum is sensitive to the interactions between the two major structural components of the red cell membrane, the lipid bilayer and the spectrin membrane skeleton.

For temperatures above $\sim 40\,^{\circ}\mathrm{C}$, the temperature dependencies of the high modes are reversed (Figure 2.11) and those of the low modes change their gradient (Figure 2.11). This is most probably a sign of protein denaturing of the membrane skeleton with associated changes in membrane stiffness. [76, 77]

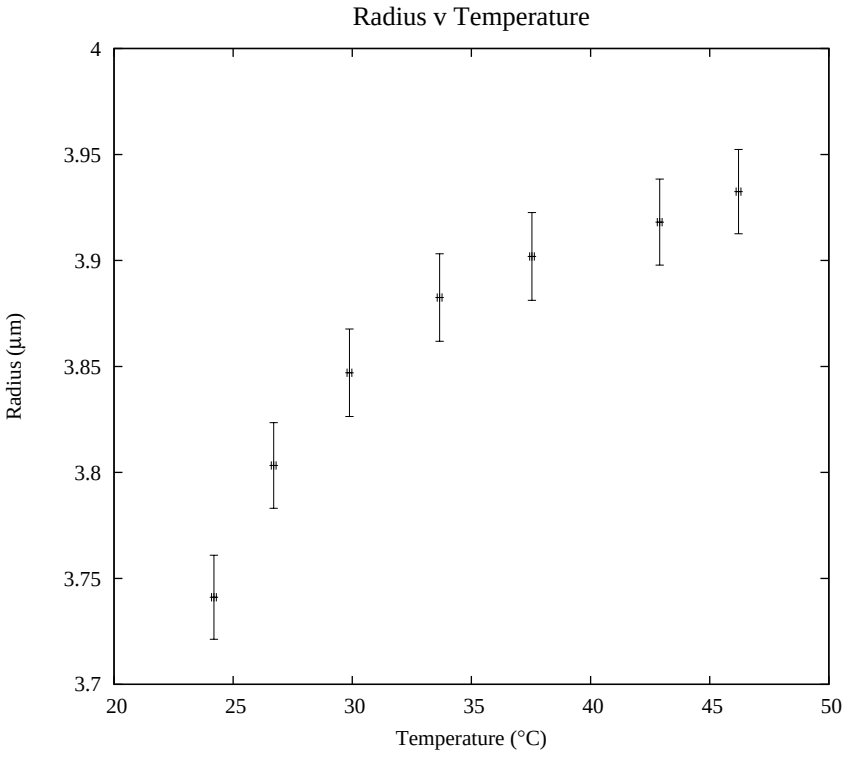

Figure 2.12: Red cell radius as a function of temperature.

The mean radius of the contour increases with temperature as can be expected from the thermal expansion of the membrane. In pure lipid bilayers the thermal expansion coefficient has been measured to be $\alpha_A = (2-6) \times 10^{-3}\,\mathrm{K}^{-1}$ [43]. Calculation of the thermal expansion coefficient from the results shown above (Figure 2.12) gives an upper limit value of $\alpha_A = 4.09 \times 10^{-3}\,\mathrm{K}^{-1}$. This suggests indeed the change in radius is due to the thermal expansion of the membrane.

2.6.4 Effect of buffer osmolarity

Previous studies have investigated the effects of changing the osmolarity of the medium on the thermal fluctuations of the red blood cell [78, 79, 68]. We performed similar experiments in order to validate our methodology.

We used the method described earlier but this time changed the osmolarity of the buffer solution. This was done by adding $\sim 20\,\mu\mathrm{l}$ volumes of water to 10 ml of the buffer solution and exchanging buffer between recording of the fluctuations. The osmolarity of the buffer was measured using a cryoscopic osmometer (Osmomat 030, Gonotec GmbH, Germany). The cell can quickly adjust to changes in osmolarity by transporting water rapidly across the membrane [80]. When exposed to buffers with reduced osmolarity, compared to physiological levels, the red cell swells, increasing its volume-to-area ratio. This in turn reduces the available excess area, which, is expected to lead to a reduction of the membrane thermal fluctuations.

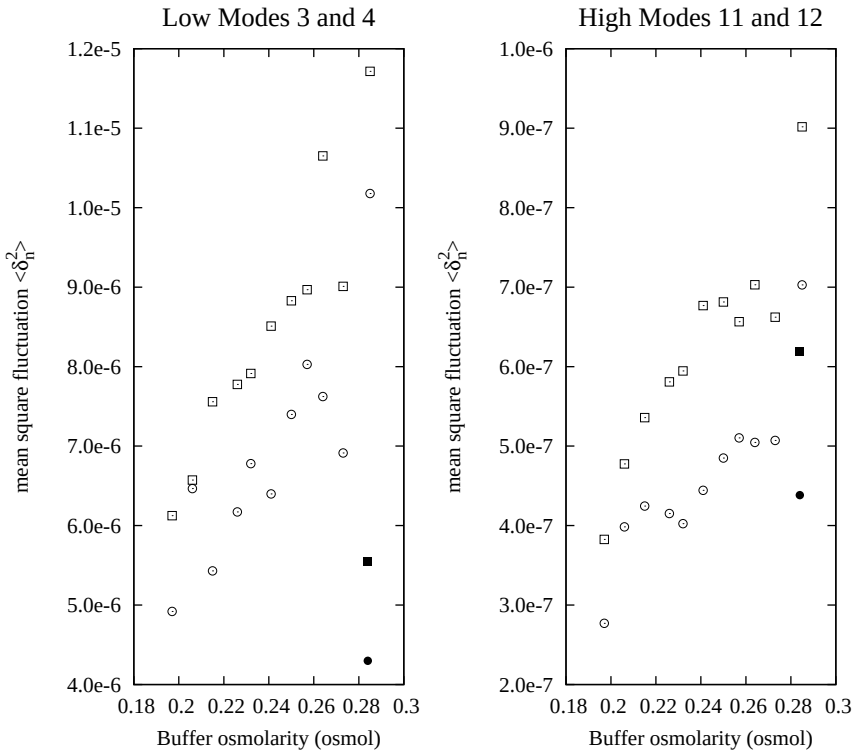

Figure 2.13: The buffer osmolarity dependence of the low modes (the long wavelength fluctuations $\sim 8\,\mu m$) and the high mode (the short wavelength fluctuations $\sim 2\,\mu m$). Buffer osmolarity decreased during the experiment (hollow symbols). The cell was returned to normal osmolarity at the end of the experiment (solid symbols).

A significant reduction in the thermal fluctuations for both the low and high modes can be clearly seen (Figure 2.13). When the cell returned to physiological osmolarity the fluctuations in the high modes recover to some degree, but the fluctuations in the low modes do not recover. Since the low modes are affected most, this points to irreversible interaction between the lipid bilayer and the membrane skeleton. Other reasons, however, cannot be ruled out, and a thorough explanation of this observation requires additional experimental work.

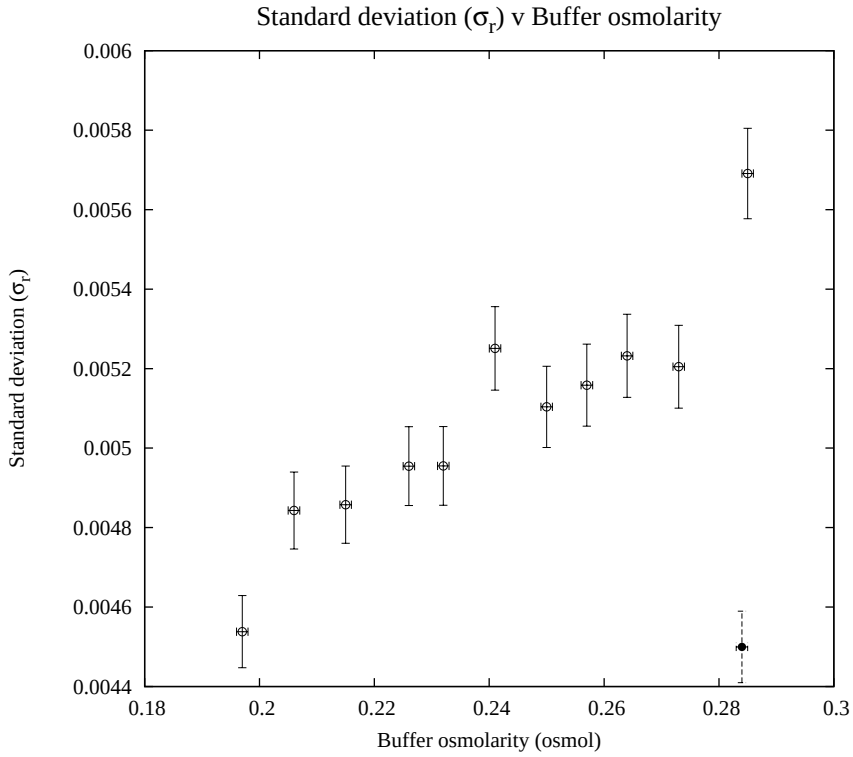

Figure 2.14: Standard deviation σ_r of the radial fluctuations as a function of buffer osmolarity. The buffer osmolarity decreased during the experiment (hollow symbols). The cell was returned to normal osmolarity at the end of the experiment (solid symbols)

The overall fluctuations of the red blood cell measured by the standard deviation of the radial fluctuations decrease with decreasing osmolarity (Figure 2.14). This agrees with the observations made with the Fourier analysis and is expected. However the fluctuations of the cell fail to return to their original level when the buffer is restored to normal osmolarity, again suggesting irreversible disruption of lipid bilayer-membrane skeleton interaction.

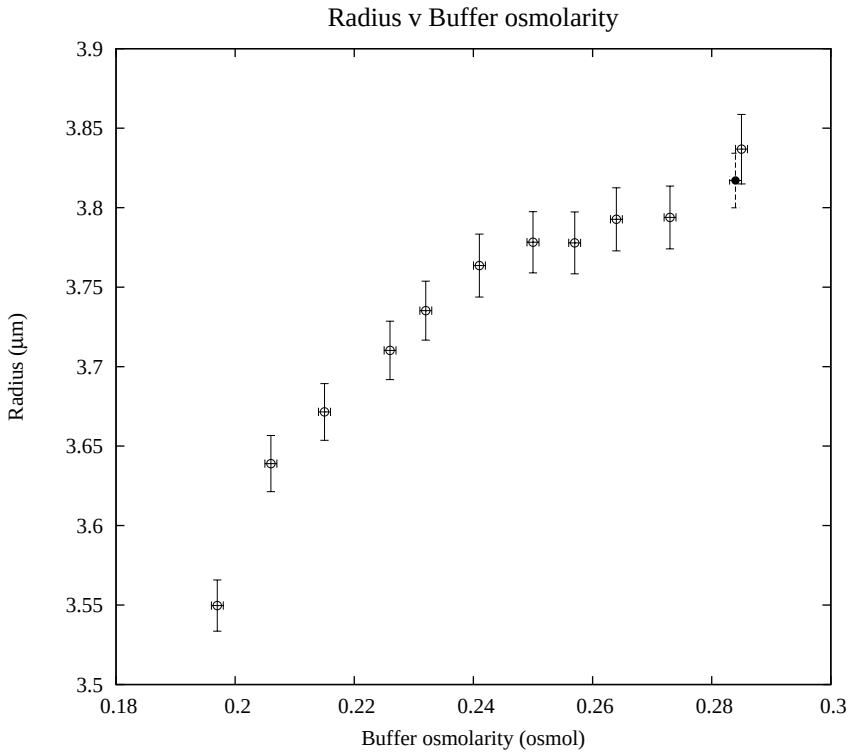

Figure 2.15: Contour radius as a function of buffer osmolarity. The buffer osmolarity is decreased during the experiment (hollow symbols). The cell was returned to normal osmolarity at the end of the experiment (solid symbols).

Progressively decreasing the osmolarity of the buffer causes the cell radius to decrease as seen in Figure 2.15. The cell swells approaching a spherical shape decreasing the radius of the projected area. The initial contour radius was fully recovered when the cell was returned to a normal physiological osmolarity at the end of the experiment despite irreversible change in the lipid bilayer-membrane skeleton interaction.

2.7 Conclusions

In this chapter we described the development and implementation of a new technique to extract the elastic properties of the red blood cell membrane from its thermal fluctuations. A robust image analysis techniques was developed to reliably and precisely extract the equatorial contours. Also described was the analysis of the

contours to determine the fluctuation spectra from which it is possible to extract the elastic properties of the red blood cell membrane.

We demonstrated the sensitivity of this method in single cell measurements which revealed the wide variation in the fluctuation spectra across a population of cells. We went on to investigated the effects of temperature and excess area on the fluctuation spectra, since these are the only other parameters other that the membrane mechanical properties which enter into the theoretical calculations of the thermal fluctuations of the membrane. We observed a decrease in the thermal fluctuations with reduction of the excess area as expected. However, results for the temperature dependence of the thermal fluctuations were unexpected in showing increases in the thermal fluctuations in the bending dominated part of the fluctuation spectrum ($n > 6$) but a reduction in the fluctuations in the low mode regime dominated by the confinement potential ($n < 6$).

However, these results are consistent with the theoretical models for the interaction between the membrane skeleton and the lipid bilayer [25]. Supporting experimental evidence for fluctuation suppressing interaction of the membrane skeleton on the lipid bilayer as proposed by Gov et al. [25].

Chapter 3

Comparison to molecular dynamics simulation

3.1 Introduction

New experimental methods for quantifying red blood cell membrane elasticity through analysis of membrane fluctuations (besides the pioneering works of Brochard and Lennon [55] and Sackmann's group [51, 12, 63, 65]) are relatively few. [67, 54] Part of the problem is that whilst the short wavelength regime ($\lambda < R$) is somewhat easier to analyse theoretically (using planar-membrane approximations [25]), short wavelengths are difficult to access experimentally. Long wavelengths ($\lambda \sim R$) are far easier to monitor and analyse, but the price to pay is that fluctuation amplitudes are affected by membrane geometry and volume and area constraints, [63] which makes a purely analytical approach untenable.

Recent successes in simulating quantitatively various aspects of RBC membrane behaviour such as thermal fluctuations, [31] large deformations, [81, 82, 83] equilibrium shapes [24] and deformations in shear flow [84], offer a way to circumvent difficulties associated with a purely analytical theory. Our approach is based on a comparison between experimentally recorded thermal fluctuation spectra and their

theoretical counterparts determined from a finite temperature particle-dynamics simulation. Since one has full control over the elasticity of the simulated mesh through the parameters of the interaction potentials, the relevant elastic constants can be evaluated by matching the fluctuation spectra. The approach is similar to that used recently simultaneously to measure the bending rigidity and effective spontaneous curvature of fluid membranes. [5]

3.2 Simulation

We used a coarse-grained particle dynamics simulation to investigate the thermal fluctuations of a 2D network (embedded in a 3D closed surface) consisting of 5762 particles arranged in a regular triangulation. The basis of the method is presented in detail elsewhere, [31] and Chapter 1. In addition to the global surface area constraint, we also implemented volume constraints, to better reflect the experimental situation. This allowed us to keep a constant volume-to-area ratio,$v = 3V/(4\pi R_A^3)$, where V is the cell volume and R_A is the equivalent radius, calculated from the cell surface area, [5] $R_A = (A/4\pi)^{1/2}$. In accordance with the experimental values for the RBC volume and surface area, [24] we used $v = 0.65$ throughout the simulations. Each pair of neighbouring particles (i, j) is allowed to interact with a harmonic potential

$$V_{ij}^{spring} = \frac{1}{2} k_s \left[(r_i - r_j) - r_0\right]^2 \tag{3.1}$$

where k_s is the spring constant (equal for all interactions), $r_{i,j}$ is the particle position and $r_0 = 100\,\mathrm{nm}$ is the equilibrium distance between two connected particles. In addition, a dihedral angle potential is applied between each two adjacent triangles, of the form

$$V_{ijml}^{dihedral} = D\left[1 + cos(\varphi_{ijml})\right] \tag{3.2}$$

where D is the relevant dihedral constant and φ is the angle between each triangle. The area constraint is implemented using Lagrange's method of undetermined mul-

tipliers. The volume is kept constant by applying an external pressure to the cell surface. The pressure is applied inwards when the volume exceeds the desired value and inwards in the opposite case. The choice of interaction potentials, along with the constant area constraint, endows the 2D mesh with finite bending and shear moduli whilst making it effectively incompressible. In order to incorporate effects from the surrounding environment, a Nosé–Hoover thermostat is employed to keep a constant temperature. The thermostat mimics the exchange of energy between the simulated cell and the environment. Viscous effects are not taken into account, as (according to the fluctuation dissipation theorem) they cannot affect the equilibrium fluctuation spectrum. The system is allowed to evolve towards equilibrium and the equations of motion for the virtual particles are solved using the molecular dynamics technique.

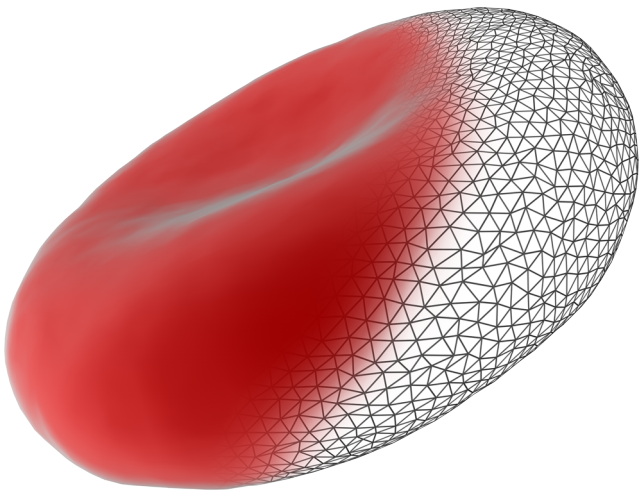

Figure 3.1: A snapshot of the red blood cell mesh in the equilibrium regime of the simulation

We find that after an equilibration phase the simulation reaches a constant temperature and the cell model steadies into a fluctuating discocyte, thus correctly approximating the mean shape of real RBCs (Figure 3.1).

3.3 Contour extraction

The equilibrium part of the simulation can be used to analyse the thermal shape fluctuations of the mesh. Equilibrium is reached when the shape reaches the required volume-to-area ratio and the average temperature is constant. Typically, we perform, 10^7 steps, or terminate the simulation if the thermostat fails resulting in large temperature fluctuations (Figure 3.2). It was also established that there was no correlation between the temporal behaviour of the applied pressure and that of the fluctuations, therefore the fluctuations are not affected by the external pressure.

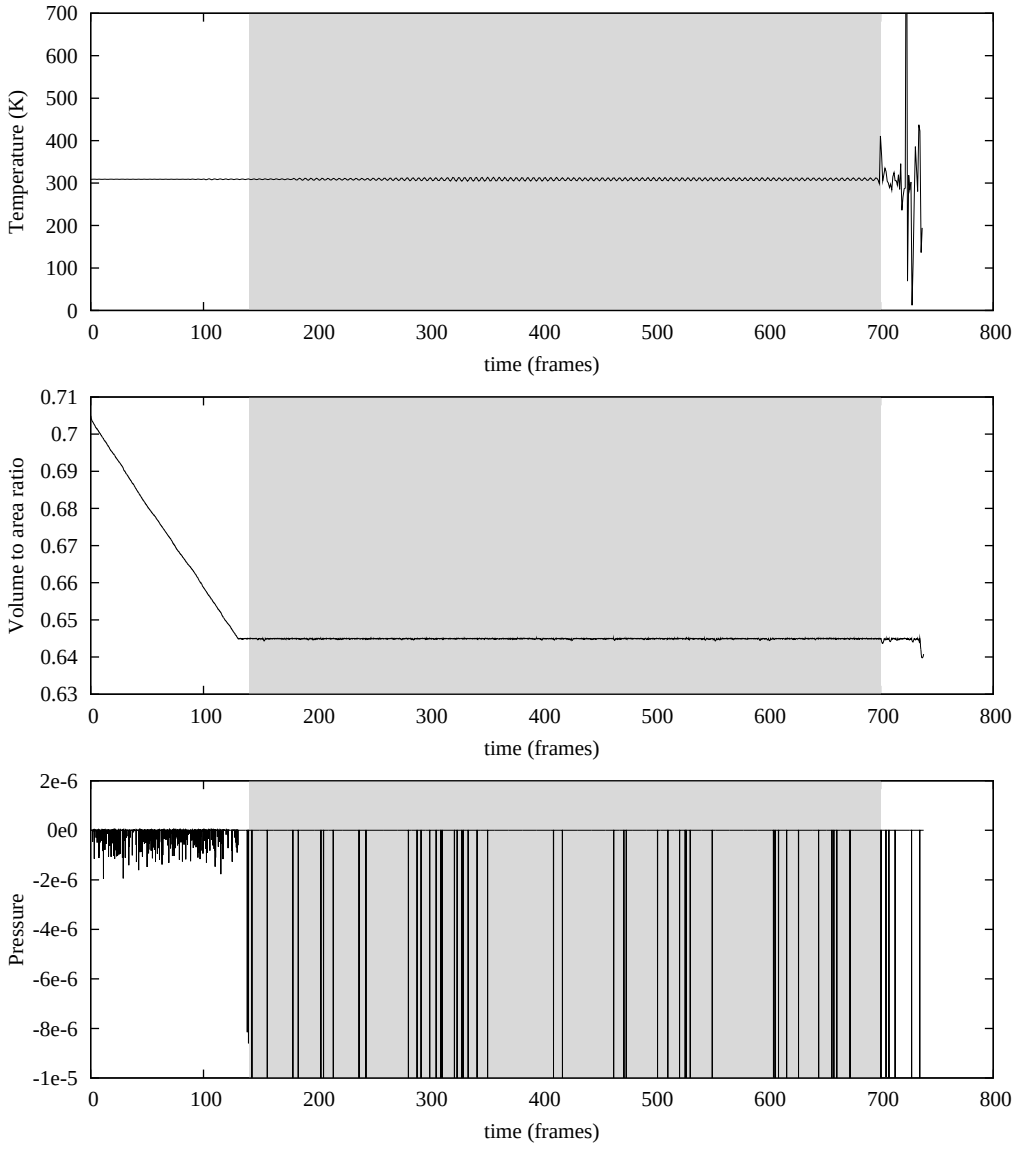

Figure 3.2: The volume and temperature as a function of simulation run-time. The grey block indicates the equilibrium part of the simulation which can be used to analyse the equilibrium fluctuation spectrum. During frames 0-100 the simulation is approaching equilibrium and therefore omitted. The temperature graph shows a failure of the thermostat beyond frame 700 and therefore these are discarded as well. The pressure graph shows an intermittently applied external pressure which maintains the volume constraint.

In order to correctly compare the mesh fluctuations to those of the experimental RBCs, 2D equatorial contours are obtained by intersecting the shape with a plane passing through the centre of mass. The simulated cell often rotates during the period of the simulation. This is due to the conservation of angular momentum in the system: as the cell collapses to the discoid shape it beings to rotate. In order to

extract the contour this rotational motion needs to be subtracted.

To do this the cell is split into two halves above and below the x-y plane through the origin. The centre of gravity of the whole cell is invariant since no net force acts on the mesh and it is positioned at (0,0,0). The centre of gravity of the sections of the mesh above and below the x-y plane is calculated. The mesh is rotated about a line perpendicular to the line connecting the centre of gravity of the section above the x-y plane and the origin in the x-y plane (Figure 3.3). The process is repeated iteratively until the difference in the (x,y) coordinates of the centre of gravities of the sections above and below the x-y plane are within ~ 0.01 Å (small compared to the spectrin lengths 100 Å). Once all frames of the simulation have been reorientated level in the x-y plane the contours can be extracted by calculating the intersection points of the bonds with the x-y plane. A typical outcome of this procedure is shown in figure 3.3.

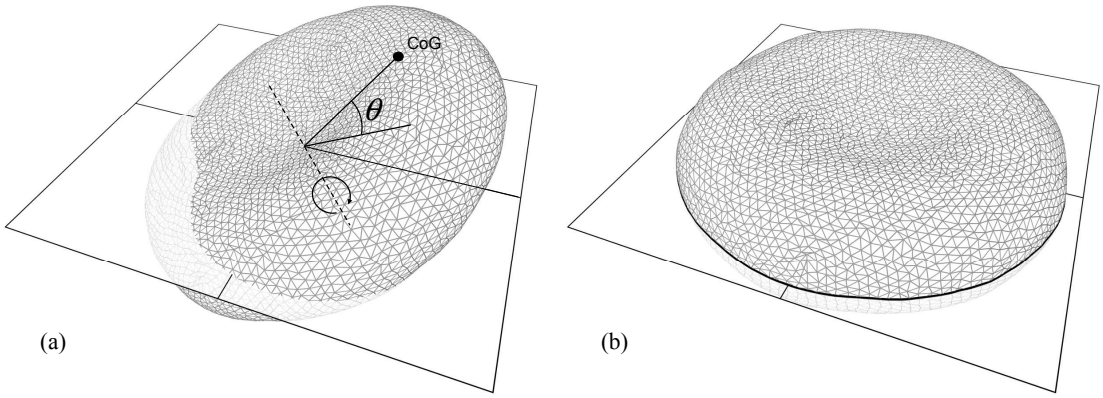

Figure 3.3: (a) Rotation of the simulated cell. CoG is the centre of gravity of the section of cell above the x-y plane. The dashed line is the axis of rotation and θ the rotation angle between the centre of gravity and the x-y plane. (b) The rotated cell with the extracted contour shown as thick black line.

This procedure results in 2D contours typically consisting of ~ 300 points each. Once extracted, we use about 300 contours at a time to calculate the fluctuation spectrum of the simulated contours, $\langle \delta_n^2 \rangle$, in exactly the same way as for the experimental contour sets. This allows a direct comparison of the contour shape fluctuations obtained experimentally and computationally.

3.4 Height fluctuations

Since the simulation provides the full shape of the red cell it is possible to extract other observables and compare these with other techniques. For example height fluctuations of the membrane can be extracted and compared to the Brochard and Lennon [55] analytical model.

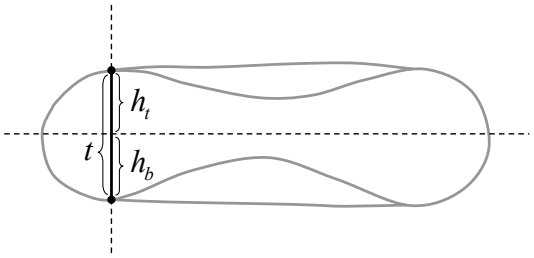

Figure 3.4: Sketch showing the measurement of the height fluctuations of the simulated red blood cell. The dashed horizontal line is the x-y plane, h_t is the height of the membrane above the x-y plane and h_b the distance below the plane.

The height of the membrane above and below the x-y plane is measured by computing the intersection of a line normal to the x-y plane with the top surface of the mesh (Figure 3.4). This is done for an array of 80×80 points giving image maps of the top surface. This is done for all frames, and the mean square height is computed of the each point. The mean square fluctuations of the height is equivalent to the measurements made by [78, 12, 63] who used the theory by Brochard and Lennon [55] to estimate the bending modulus of the red blood cell. To compute the mean square heights and thicknesses the arrays of positions are loaded into ImageJ as a series of 32-bit float images.

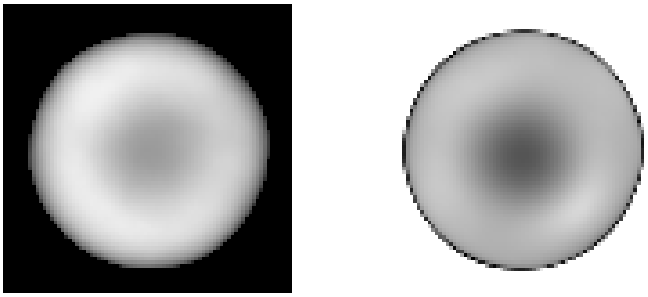

(a) (b)

Figure 3.5: (a) An image map of the top surface of the simulated red blood cell. (b) The height standard deviation image map for 300 frames of the simulation, where the brighter areas indicate larger mean square height fluctuations $\langle h^2 \rangle$.

In the first approximation, these can be interpreted by using the flat membrane approximation. Integrating equation (1.20) across all wavelengths from $q_{min} = 2\pi/L$ to $q_{max} = 2\pi/a$ (where L is the the linear dimension of the membrane and a is the membrane thickness) the folowing expression for overall mean square height fluctuations $\langle h^2 \rangle$ can be found [55, 85]:

$$\langle h^2 \rangle \approx \frac{k_B T}{16\pi^3 \kappa} L^2 \tag{3.3}$$

where κ is the bending modulus and L the linear dimensions of the membrane. The should be considered as an order of magnitude estimation only, as it takes into account just the bending properties of the membrane.

3.5 Results

3.5.1 Histograms

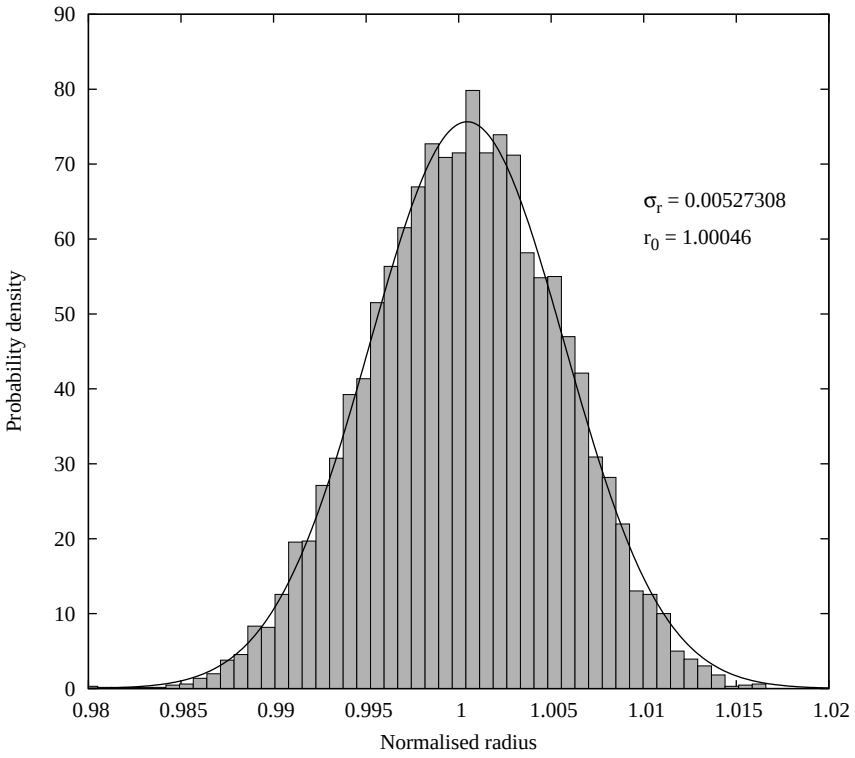

Figure 3.6: Radial distribution fluctuation histogram for simulation data. Clearly the data is Gaussian distributed as the real cell data and has comparable width and height distribution as a real cell.

Figure 3.6 shows the histogram of the radial fluctuations of the simulated shape, $r(\theta)/\langle r(\theta)\rangle$, as defined in Chapter 2.

The radial standard deviation in this particular case is $\sigma_r = 5.3 \times 10^{-3}$, which compares well to those obtained from normal cells in experiments, $(5.0 \pm 0.5) \times 10^{-3}$. The fluctuations are also normally distributed as in real cells suggesting that the overall fluctuations of the simulated cell are equilibrium and the shape behaves in the same way as a real cell.

3.5.2 Height Fluctuations

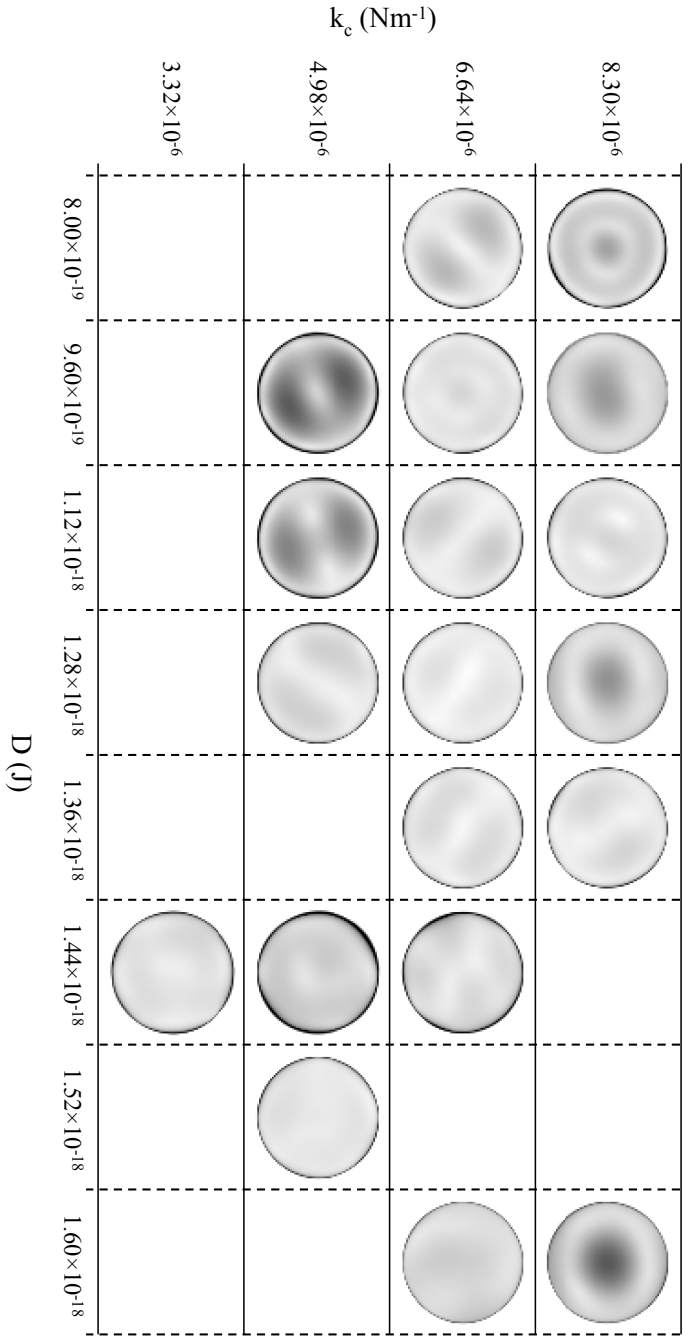

Figure 3.7: Height fluctuation maps for the simulation for varying harmonic potential, k_s, and dihedral potential constants, D, constants. Brighter areas indicate larger mean square height fluctuations $\langle h^2 \rangle$.

Figure 3.7 shows height fluctuation maps derived from the simulation at different values of the harmonic and dihedral constants. As seen in Figure 3.7 there appears to be no consistent trends in the height fluctuations. Clearly the mean square

fluctuations are in most cases not evenly distributed. This is not unexpected as the fluctuations are predicted to be largest over the cell rim than the centre [65].

Using average mean square height fluctuations across the simulated cell surface the bending modulus is calculated using equation (3.3). Overall all the values form the bending modulus are within range of those obtained by other similar methods ($\kappa = (1.74 \pm 0.53) \times 10^{-19}$ J).

3.5.3 Contour fluctuations

A direct comparison between an experimentally obtained fluctuation spectrum of a normal RBC and its simulation counterpart is shown in figure 3.8. An estimation of the (zero-temperature) shear and bending moduli can be obtained by using the approximate relationships reported in the literature, [36, 33] $\mu \approx (\sqrt{3}/4)k_s$ and $\kappa = D/\sqrt{3}$. Using the values of the spring and dihedral constants for the simulated cell in figure 3.8, $k_s = 8.3 \times 10^6\,\mathrm{Nm}^{-1}$ and $D = 1.3 \times 10^{18}$ J, gives value a of shear modulus $\mu = 3.6 \times 10^6\,\mathrm{Nm}^{-1}$ and a bending modulus $\kappa = 7.5 \times 10^{19}$ J.

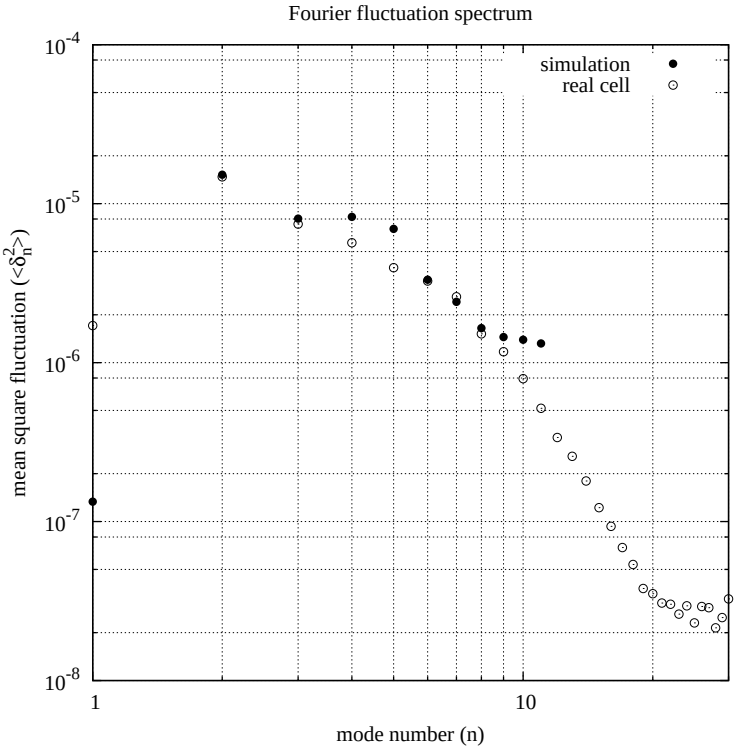

Figure 3.8: Mean square fluctuations of the equatorial 2D contour, $\langle \delta_n^2 \rangle$, as a function of the mode number, n, for a normal RBC (hollow symbols) and a matched simulation (solid symbols). Values of the interaction parameters: $k_s = 8.3 \times 10^6\,\mathrm{Nm}^{-1}$ and $D = 1.3 \times 10^{18}\,\mathrm{J}$.

Generally it was found that for the limited number of contour points in the simulation contour only modes up to $n \approx 10$ can reliably be obtained.

The external pressure acting as a volume constraint in the model does not affect the shear modulus as calculated by the equation above. The external pressure could give rise to membrane tension only via changes in the density of the membrane (as compared to the stress-free state), which in our model is prevented by the area constraint. We also established that there was no correlation between the temporal behaviour of the applied pressure and that of the fluctuation modes, which means that the fluctuation modes (and therefore the membrane bending modulus) are not affected by the external pressure.

3.6 Conclusions

Comparison between experimentally and computationally obtained fluctuation spectra shows that they are in agreement with values of the spring constant $k_s \sim 8.3 \times 10^{-6}\,\mathrm{Nm}^{-1}$ and the dihedral constant $D = 1.3 \times 10^{-18}\,\mathrm{J}$. This allows an order of magnitude estimation of the (zero-temperature) shear and bending moduli using the approximate relationships reported in the literature, [36, 33] $\mu \approx (\sqrt{3}/4)k_s$ and $\kappa = D/\sqrt{3}$. We obtain $\mu = 3.6 \times 10^{-6}\,\mathrm{Nm}^{-1}$ and $\kappa = 7.5 \times 10^{-19}\,\mathrm{J}$.

The value for the bending modulus compares favourably with previous experiments in the same wavelength regime ($\lambda \sim R$) [51, 65]. For example, the theoretical interpretation performed by Peterson et al. [65] for RBC thickness fluctuations suggests a bending modulus of (1.4–4.3) $\times 10^{-19}\,\mathrm{J}$, depending on the elastic model used. Strey et al. [51] analysed RBC membrane flicker at four orthogonal points around the membrane at wavelengths comparable to the cell dimensions. For the bending modulus they obtained a mean value of $4 \times 10^{-19}\,\mathrm{J}$, with individual measurements covering the range from $2 \times 10^{-19}\,\mathrm{J}$ to $7 \times 10^{-19}\,\mathrm{J}$.

Whilst the values obtained for the membrane bending rigidity are of the same order of magnitude as those reported in previous studies of the long-wavelength regime, the shear modulus obtained, $3.6 \times 10^{-6}\,\mathrm{Nm}^{-1}$, is closer to the values reported in static deformation experiments, such as micropipette aspiration [43] and optical tweezers studies [46, 61, 62]. This seems to contradict previous conclusions [51] that freely flickering RBCs, i.e. at small shear deformations, have negligible (less than $\sim 10^{-7}\,\mathrm{Nm}^{-1}$) shear modulus. Our results support the notion that the RBC membrane skeleton may not necessarily show vanishingly small shear rigidity at small deformations. Further evidence for this conclusion could be drawn from previous Monte Carlo polymer chain simulations of the erythrocyte cytoskeleton [86] which suggest a shear modulus as high as $\sim 10^{-5}\,\mathrm{Nm}^{-1}$. It is interesting to note that recent models of the RBC membrane that explicitly consider its composite nature lead to similar conclusions. For example, Gov et al. [25] take into account the influence of the spectrin network through two parameters in the free energy functional, an effec-

tive surface tension, σ, and a confining parameter, γ, both related to the stiffness of the spectrin filaments. The confining parameter γ, which serves to constraint the bilayer fluctuations due to the proximity of the (rigid) membrane skeleton, can be seen to depend on the bending and shear membrane moduli, [25] $\gamma \approx \mu^2/\kappa$. Analysing experimental short-wavelength fluctuation data [62] for two RBCs, these authors find $\gamma = 1.0 \times 10^7\,\mathrm{Jm}^{-4}$ and $\gamma = 7.5 \times 10^7\,\mathrm{Jm}^{-4}$. This, in turn, suggests that the skeleton shear modulus could reach a value of the order of $10^{-6}\,\mathrm{Nm}^{-1}$ even when a small value of $\kappa = 2 \times 10^{-20}\,\mathrm{J}$, characteristic for the short-wavelength regime, is used.

The feasibility for interpretation of the long-wavelength part of the RBC membrane fluctuation spectrum through a coarse-grained particle dynamics simulation has been demonstrated. The simulation faithfully reproduces the average cell discotic shapes and correctly describes the mean square fluctuations of the equatorial contours of RBCs, returning physically meaningful values for the elastic membrane parameters.

Further work is underway in our laboratories exploring comprehensively the parameter space of the simulation through variations in the values of the interaction potential parameters, volume to area ratio and the size of the simulated mesh, which will allow fast quantification of the elastic constants of any RBC.

Chapter 4

Oxidative Stress

4.1 Introduction

Oxidative stress results from an imbalance in the production of reactive oxidative species (ROS) such that it exceeds the cell antioxidant defence. The resulting cell damage is believed to be the main cause of cell death and dysfunction in disease and the cumulative effect of oxidative damage over longer time periods could to be the driving force in the process of cell ageing. As a result oxidative stress has been implicated in numerous age related diseases such as Alzheimer disease [13], atherosclerosis [87] and diabetes mellitus [59].

4.1.1 Reactive Oxygen Species and the RBC

Reactive Oxygen Species (ROS) include hydrogen peroxide (H_2O_2), superoxide ($O_2^{\bullet -}$) and hydroxyl radical ($^{\bullet}OH$). In most cells the primary source of ROS are the mitochondria. Despite lack of mitochondria, ROS are continuously produced in the red blood cell due to autoxidation of haemoglobin. Even a small rate of autoxidation of haemoglobin can produce a substantial amount of $O_2^{\bullet -}$ [88, 89]. Superoxide rapidly

disappears in aqueous solution because of its dismutation reaction

$$2O_2^{\bullet -} + 2H^+ \rightarrow H_2O_2 + O_2 \tag{4.1}$$

Any system producing superoxide will, as a result of the dismutation reaction, will also produce hydrogen peroxide.

Ferrous iron in haemoglobin can donate electrons to hydrogen peroxide generating hydroxyl radicals in a process called the Fenton reaction [90].

$$Fe^{2+} + H_2O_2 \rightarrow Fe^{3+} + {}^{\bullet}OH + OH^- \tag{4.2}$$

The hydroxyl radical is a very aggressive oxidant that can attack most biological molecules at almost diffusion controlled rate [91]. In lipids, hydroxyl radicals can attack polyunsaturated fatty acid chains to produce lipid peroxides and lipid radicals initiating lipid peroxidation.

4.1.2 RBC defence mechanisms

In performing its physiological role the red blood cell is exposed to continuous oxidative stress and requires exceptional antioxidant defences. The main antioxidant defence mechanisms are concerned with the removal of superoxide radicals, accelerating the decomposition of hydrogen peroxide and the scavenging of hydroxyl radicals.

The enzyme superoxdismutase (SOD) accelerates the dismutation of $O_2^{\bullet -}$radicals producing hydrogen peroxide. Hydrogen peroxide is removed by the enzymatic antioxidants catalase (CAT), glutathione peroxidases (GSHPx) and the peroxiredoxin Prx 2. The relative importance and effectiveness of these enzymes of catalysing the decomposition of H_2O_2 is complex and still a matter of debate. Before the discovery of glutathione peroxidase, catalase was assumed to be responsible for H_2O_2 scavenging. Glutathione peroxidase however was found to have higher affinity to H_2O_2 and therefore likely to be primarily responsible for H_2O_2 scavenging at physiological

(low) concentrations of H_2O_2. More recent studies have shown that the reaction rate of H_2O_2 with Catalase is exponential and more effective at low concentrations than previously thought. Nagababu et al. [92] suggested that the role of GSHPx is to protect the membrane since it is a better scavenger of H_2O_2 close to the membrane than Catalase, and can also decomposition lipid hydroperoxides. Prx 2 is very sensitive to reversible oxidation by H_2O_2 at micromolar concentrations reducing hydrogen peroxide and alkyl hydroperoxides to alcohol and water. But since Prx 2 is one of the most abundant proteins in the erythrocyte ($\sim 250\,\mu M$ in the cytosol equivalent to 10^7 copies per cell), it can handle equivalent concentrations of H_2O_2 without recycling. This suggests that Prx 2 does not act as a classical antioxidant protein but rather as a very effective H_2O_2 scavenging protein.

There are two main groups of non-enzymatic antioxidants, lipophylic (i.e. partition in the membrane) (vitamin E, caroteniods, ubiquinon, melatonin, etc.) and water soluble (vitamin C, glutahione, uric acid, etc.). Vitamin E is the most widely distributed antioxidant in nature and works together with Vitamin C to inhibit lipid peroxidation in the membrane by converting lipid peroxyl radicals into lipid hydroperoxides by the action of Vitamin E [93].

4.1.3 Effects of ROS on the RBC

Much of the damage to the red blood cell structures can be associated with the initial oxidation of haemoglobin. Oxidative injury to haemoglobin (Hb) leads to the formation of methemoglobin (MetHb), reversible hemichromes (rHCRs), and irreversible hemichromes (iHCRS) [94, 95]. Binding of oxidatively denatured haemoglobin disrupts the spectrin network and causes band 3 clustering [96, 97, 98, 99]. Denatured haemoglobin releases free hemin which promotes the formation of lipid radicals leading to lipid peroxidation [100, 95, 93].

Membrane protein oxidation

Jarolim et al. [95] showed that haemoglobin and methemoglobin stabilised isolated membrane skeletons by promoting the self association of spectrin dimers into tetramers. The heme iron of the spectrin-bound haemoglobin catalyses intermolecular covalent bonding through generation of hydroxyl radicals from H_2O_2 forming cross-linked haemoglobin-spectrin complexes [101]. Whereas further oxidation of MetHb to iHCR and rHCR destabilised the membrane by decreasing the formation of the spectrin-protein 4.1-actin complex. Kriebardis et al. [102] have reported a correlation between membrane bound haemoglobin and increased oxidation of the membrane skeletal proteins. Oxidation modifies the sulfydryl groups of spectrin which results in a reduced ability of spectrin to bind to protein 4.1 and structurally causes the spectrin to acquire a circular conformation. Either of these changes would result in failure of the red cell membrane skeleton and only require oxidation of one or two of the 35 sulfydryl groups in spectrin [103]. The effects of these processes have been observed. For example Wagner et al. [58] showed that oxidation of spectrin in stored blood cells correlated with increased vesiculation. The micro vesicles contained the anchor proteins 4.1 and 4.2 but were spectrin free suggesting the spectrin had detached from the membrane which resulted in budding. The progressive loss of cell area and cell dehydration are characteristic features of RBC ageing [104].

Band 3 clustering

Low et al. [96] showed that as haemoglobin begins to denature it cross-links band 3 into aggregates and these aggregates constitute the antigenic determinate recognised by the antibodies to senescent the cells. Hemichromes have a high affinity for band 3. Antigen IgG binds thereby signalling the removal of the RBC by the reticuloendthelial system. Band 3 clustering suggests this protein has greater lateral mobility within the membrane plane i.e. it is not restricted by the constraint of the spectrin network. The haemoglobin-spectrin complex inhibits the spectrin dimer self-association and provides a relaxation on the lateral constraint of Band 3

[96, 101].

Lipid Peroxidation

The first step in the chain reaction of peroxidation in the membrane is the abstraction of hydrogen ($H^{\bullet}$) by a sufficiently reactive species from a methylene ($-CH_2-$) group. Abstraction of the hydrogen leaves behind a unpaired electron on the carbon ($-{}^{\bullet}CH-$). The presence of a double bond in the fatty acid weakens the (C-H) bonds on the carbon atom adjacent to the double bond and thus facilitates ($H^{\bullet}$) removal. This makes the polyunsaturated fatty-acid side chains of membrane lipids particularly sensitive to peroxidation. The following is the reaction of the hydroxyl (${}^{\bullet}OH$) radial with the lipid chain (LH):

$$\begin{aligned} LH + {}^{\bullet}OH &\rightarrow L^{\bullet} + H_2O \\ L^{\bullet} + O_2 &\rightarrow LOO^{\bullet} \\ LOOH^{\bullet} + LH &\rightarrow LOOH + L^{\bullet} \end{aligned} \tag{4.3}$$

Reduced iron (Fe^{2+}) react with lipid peroxides (LOOH) to give alkoxyl radicals, as follows

$$LOOH + Fe^{2+} \rightarrow LO^{\bullet} + Fe^{3+} + OH^{-} \tag{4.4}$$

whereas oxidised iron (Fe^{3+}) react more slowly to give peroxyl and alkoxyl radicals by

$$LOOH + Fe^{3+} \rightarrow LOO^{\bullet} + Fe^{2+} + H^{+}. \tag{4.5}$$

Both alkoxyl and peroxyl radicals stimulate the chain reaction of lipid peroxidation by abstracting further hydrogen atoms. Extensive lipid peroxidation causes loss of membrane fluidity, falls in transmembrane potential and increased permeability to H^{+} and other ions and eventual cell rapture hemolysis. [88] Propagation reactions of lipid peroxidation in a biological membrane do not proceed far before they reach a protein; thus lipid peroxidation in biological membranes causes substantial damage to membrane proteins.

4.1.4 Oxidative stress and RBC membrane mechanical properties

As evident from the above summary, oxidative stress can inflict wide-ranging damage to the main structural components of the RBC (lipid bilayer, membrane skeleton) responsible for the integrity and mechanical properties of the membrane. Several studies investigate changes in the membrane due to oxidation and related changes in membrane rigidity [97, 98, 105, 106]. They conclude that the main contributor to the membrane stiffening was the increased rigidity of the membrane skeleton due to the formation of haemoglobin-spectrin complexes [97]. Changes in membrane mechanical properties are typically reported by measuring changes in cell deformability (as measured, for example using ektacytometry [98]). These methods, however are capable of characterising only the integral response of the membrane to imposed strain. Detailed studies of the effect of oxidation on the mechanical properties of each membrane structural component (lipid bilayer, membrane skeleton) and in terms of the relevant elastic constants (bending modulus, shear modulus, elastic interactions between the lipid bilayer and membrane skeleton) have not been undertaken. This is therefore the aim of the present chapter. We show that different oxidative agents can damage differently the lipid and protein content of the RBC, leading to clear signature in the membrane elastic behaviour.

4.2 Experimental method

Fresh blood samples were collected from healthy volunteers by pin pick lancet (Acc-Chek, Roche Ltd). The small volume, $\sim 5\,\mu$l, was immediately suspended in 1 ml of PBS buffer pH 7.4 (Oxoid Ltd, Basingstoke, UK) with 1 mg/ml BSA (Sigma-Aldrich, United Kingdom).

The cells were first video recorded while in normal PBS, the buffer was then exchanged with a PBS buffer containing either hydrogen peroxide (H_2O_2) or cumene

hydroperoxide (cumOOH) (Sigma-Aldrich, United Kingdom). The buffers were exchanged by placing excess solution on one side of the chamber and 'pulling' it through with tissue or filter paper introduced to the opposite side. H_2O_2 is a water soluble oxidant permeable to the cell membrane while cumene hydroperoxide an organic oxidant insoluble in water which partitions into it. To dissolve the cumene hydroperoxide in the PBS buffer solution it was shaken vigorously and then sonicated in ultrasonic bath for a few minutes. After the buffer was exchanged the cells were recorded at regular intervals (~ 10 minutes) for a period of ~ 90 minutes. For each recording a complete analysis of the fluctuation spectra and radial fluctuations was performed.

4.3 Results

4.3.1 Fluctuation spectra

Figure 4.1 shows the fluctuation spectra of a red blood cell exposed to 100 µM of H_2O_2 for a period of ~ 90 minutes and another exposed to 100 µM of cumOOH for a similar period of time. Figure 4.1 shows the considerable effect of the oxidants on the membrane fluctuation dynamics. Within the first hour, cells exposed to H_2O_2 show at first a steady decrease in the mean square fluctuations of the low modes ($n < 6$) suggesting modifications to the membrane skeleton. This is accompanied by initially little if any change in the high mode regime ($n > 6$) suggesting limited modification to the bending elasticity and therefore the lipid bilayer. The cells exposed to cumene hydroperoxide however show different behaviour. The low modes again shows a steady decrease but this is accompanied by a reduction in the fluctuation amplitudes of the high modes beginning from the outset of the cumOOH addition. This shows that the cumene hydroperoxide is not only affecting the membrane shear elasticity, but also the bending rigidity suggesting that not only the membrane skeleton but also the lipid bilayer are modified.

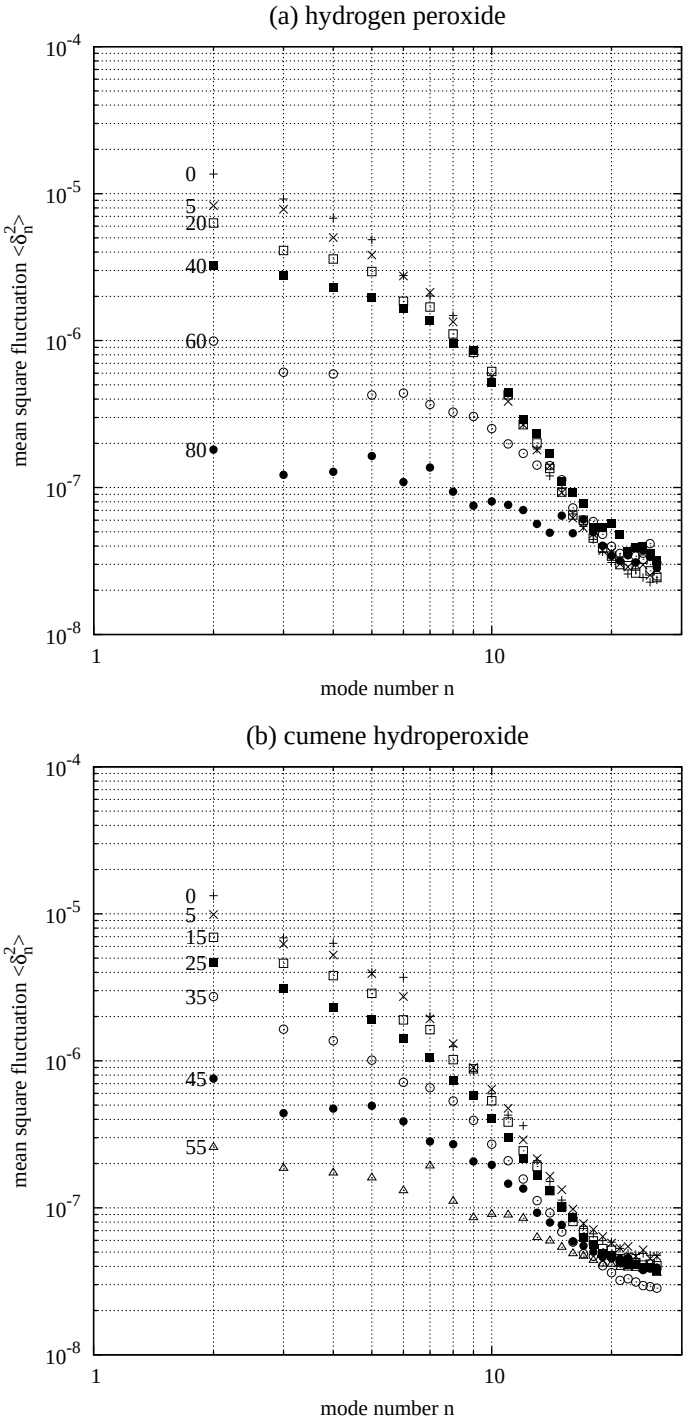

Figure 4.1: (a) Fluctuation spectra of H_2O_2 treated red blood cell. The fluctuation spectrum of the untreated cell is shown with (+). Subsequent recording are made at times, indicated at first data point (in minutes), from addition of H_2O_2. With increased exposure the fluctuation spectra flattens out the low modes are affect most with the high modes appearing to be unaffected until later in the exposure. (b) Fluctuation spectra of cumene hydroperoxide treated red blood cell. The fluctuation spectrum of the untreated cell is shown with (+). Subsequent recording are made at times, indicated at first data point (in minutes), from addition of cumene hydroperoxide . With increased exposure the whole fluctuation spectra decreases with both high and low mode effected.

4.3.2 Kinetics

The radial fluctuations histograms are sensitive to changes in overall fluctuations. Figure 4.2 shows the effect of hydrogen peroxide on the overall fluctuations of the membrane.

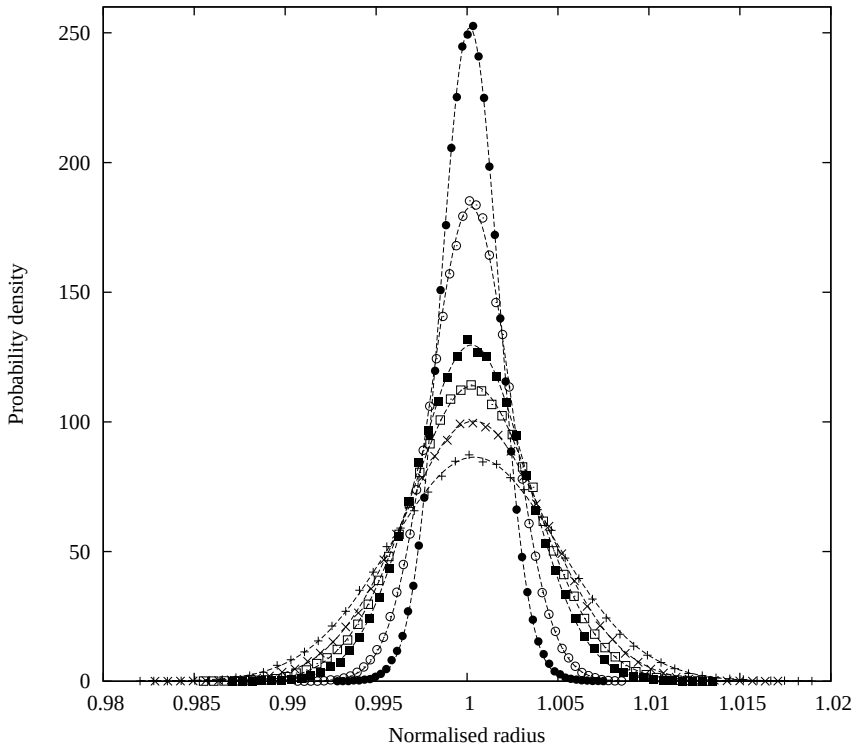

Figure 4.2: Radial displacement histograms of a cell treated with H_2O_2 over a period of ~ 90 minutes. The histogram of the untreated cell is shown with (+).

The radial fluctuation histograms of cells treated with cumene hydroperoxide show identical trends. Comparison of the standard deviation of the distribution (σ_r) over time enables the quantification of the kinetics of the reactions of the different hydroperoxides (Figure 4.3).

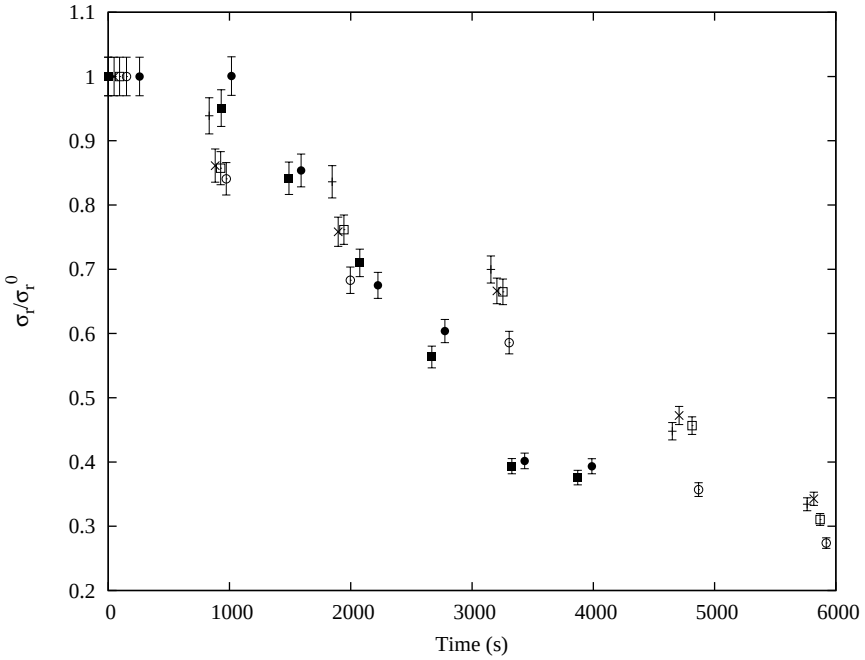

Figure 4.3: Normalised cell radial standard deviation σ_r as a function of time. The hollow symbols are four H_2O_2 treated cells and the solid symbols show two cumene hydroperoxide treated cells. The errorbars are the uncertainty in the fitting of σ.

The rate of decrease in the overall fluctuations for cells treated with cumene hydroperoxide is significantly greater than that of the H_2O_2 treated cells (Figure 4.3). This suggests that the cumene hydroperoxide is either a more potent oxidant or the structures oxidised by the cumene hydroperoxide have great influence on the overall elastic properties of the cell and therefore the fluctuations. A third alternative would be an increased effective cumOOH concentration due to the fact that all of it is in the membrane.

Evaluating the relevant elastic moduli from the fluctuations by comparison with the simulation is not yet possible. The simulation currently shows instabilities when the values of the bending and shear moduli are high. We will therefore present a semi-quantitative analysis based on the analytical theory by Gov et al. [25] who considered the RBC fluctuations in the flat membrane approximation.

4.4 Alternative analysis theory

The Helfrich energy of the flat membrane can be modified to include an addition term to describe the interaction between the cytoskeleton and the lipid bilayer [25] to give

$$F \simeq \int dS \left[\frac{1}{2}\sigma(\nabla h)^2 + \frac{1}{2}\kappa(\nabla^2 h)^2 + \frac{1}{2}\gamma h^2\right] \tag{4.6}$$

where κ is the bending modulus, σ is the membrane tension and γ is the confinement potential which is a measure of the interaction of the membrane skeleton with the lipid bilayer and is related to the spectrin stiffness, $\gamma \backsimeq \mu^2/\kappa$. In this model the main contribution to σ comes from the membrane skeleton therefore is larger than the membrane tension in bilayer model where the only contribution is the entropic tension.

Equation (4.6) allows the fluctuation spectrum of a flat membrane to be derived [25] using a very similar approach to the one described in the introduction to give

$$\left\langle \left|\tilde{h}(q)\right|^2 \right\rangle = \frac{k_B T}{\gamma + \sigma q^2 + \kappa q^4} \tag{4.7}$$

Since in experiment we monitor only the fluctuations of a line (the contour), equation (4.7) can be used to calculate the fluctuation spectrum along a line though the membrane, $\left\langle \left|h(q_x, y=0\right|^2 \right\rangle$. Taking into account that $\left\langle \left|h(q_x, y=0)\right| \right\rangle = \frac{\pi \left\langle R \right\rangle^3}{2} \left\langle \left|c_n\right|^2 \right\rangle$ for our contour representation [29], the following expression for the Fourier amplitudes of the contour is obtained:

$$\left\langle \left|c_n\right|^2 \right\rangle = \frac{1}{2\pi}\frac{k_B T}{\kappa}(\tilde{\sigma}^2 - \tilde{\gamma})^{-1/2}\left[(\tilde{\sigma} + n^2 - \sqrt{\tilde{\sigma}^2 - \tilde{\gamma}})^{-1/2} - (\tilde{\sigma} + n^2 + \sqrt{\tilde{\sigma}^2 - \tilde{\gamma}})^{-1/2}\right] \tag{4.8}$$

where

$$\tilde{\sigma} \equiv \frac{\sigma \left\langle R \right\rangle^2}{2\kappa} \qquad \tilde{\gamma} \equiv \frac{\gamma \left\langle R \right\rangle^4}{\kappa} \qquad q_x = \frac{n}{\left\langle R \right\rangle} \tag{4.9}$$

Thus the fluctuation spectra of red blood cells can be fitted with equation 4.8 in order to extract estimates of the material properties of the membrane. We need to emphasise the approximate character of this treatment, as equation (4.7) and (4.8)

are strictly valid for flat membranes. whereas we measure fluctuation wavelengths comparable with the cell size ($\lambda \sim R$). This analysis, therefore can only serve to compare relative changes in the course of oxidation, without affirming absolute values for the elastic constants.

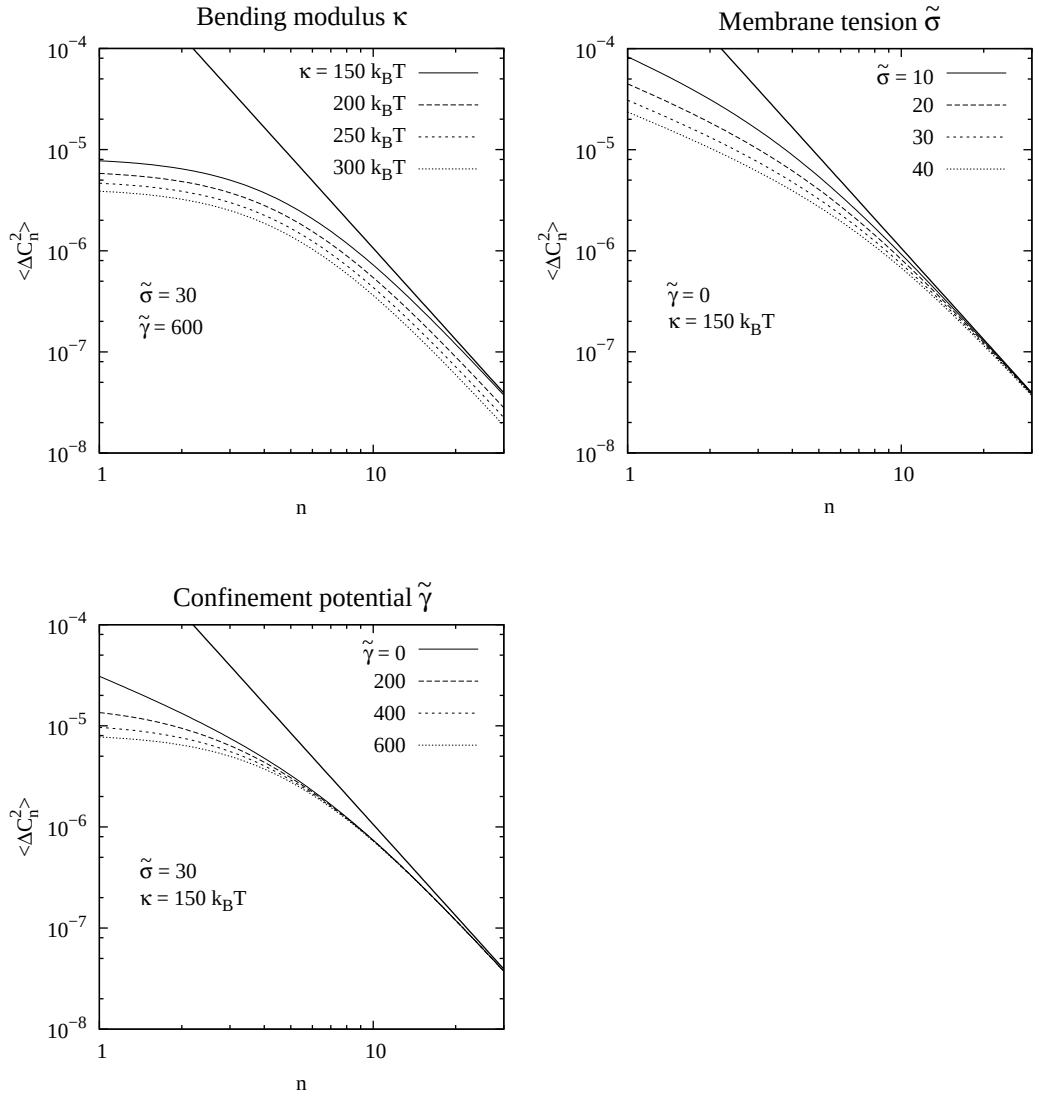

Figure 4.4: A series of curves showing the behaviour of the fluctuation spectrum on modification of the membrane tension ($\tilde{\sigma}$), bending modulus (κ) and confinement potential ($\tilde{\gamma}$) parameters.

Figure 4.4 shows the effect of changing the parameters on the fluctuation spectra. Increasing the bending modulus shifts the entire spectrum down and is the only parameter to effect the high modes ($n > 7$). This is expected since at the limit of

vanishing σ and γ the Helfrich derived fluctuation spectrum ($\sim 1/n^3$) is recovered. The effect of the membrane tension is most significant in the low mode regime but still significant in modes $n = 10 - 15$ as it approaches the maximum measurable mode limit of the experimental technique. The most dominant effect in the low mode regime ($n < 6$) is the confinement potential which significantly suppresses the first few modes. This model does not account for the membrane geometry and assumes no difference in curvature in the plane of the contour and perpendicular to it, i.e. around the red blood cell edge and across the rim of the cell. The model also considers the membrane to be a homogeneous structure which is only appropriate on length scales greater than the spectrin length ($> 200\,\mathrm{nm}$), this corresponds to modes less than $n = 50$ which is beyond the limits imposed by optical resolution.

4.5 Material properties of membrane

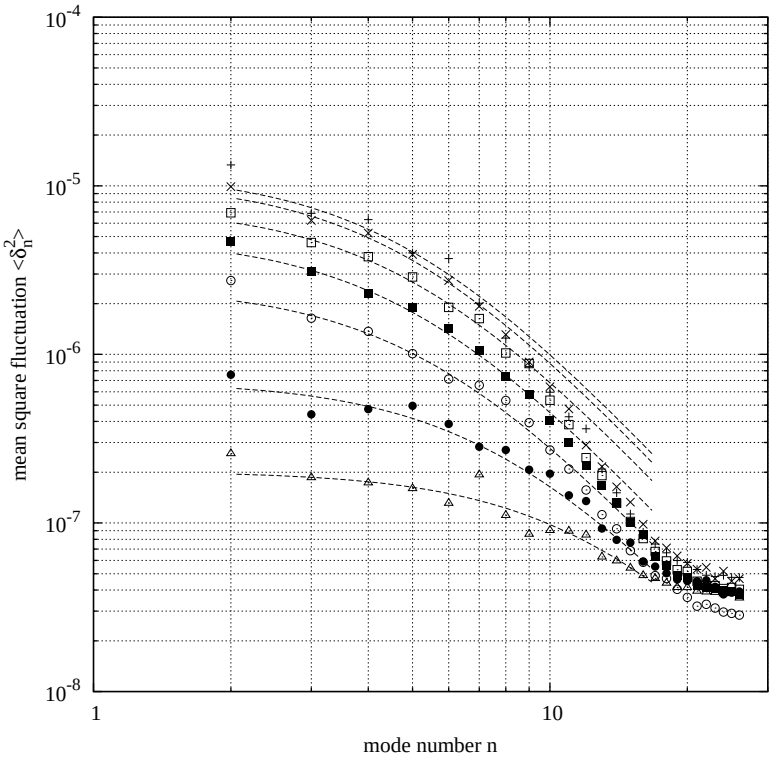

Figure 4.5: Mean square fluctuations of a cell treated with cumene hydroperoxide. Equation 4.8 is fitted to each spectrum.

Figure 4.5 shows the fitting of equation (4.8) to the fluctuation spectra of a cell treated with cumene hydroperoxide. From the fitting values of the confinement potential (γ), membrane tension (σ) and bending modulus (κ) can be extracted. The confinement potential and membrane tension are primarily effected by the membrane skeleton and changes in these parameters would reflect structural changes in the membrane skeleton. The bending modulus reflects only the state of the bilayer as the membrane skeleton has a lower resistance to bending.

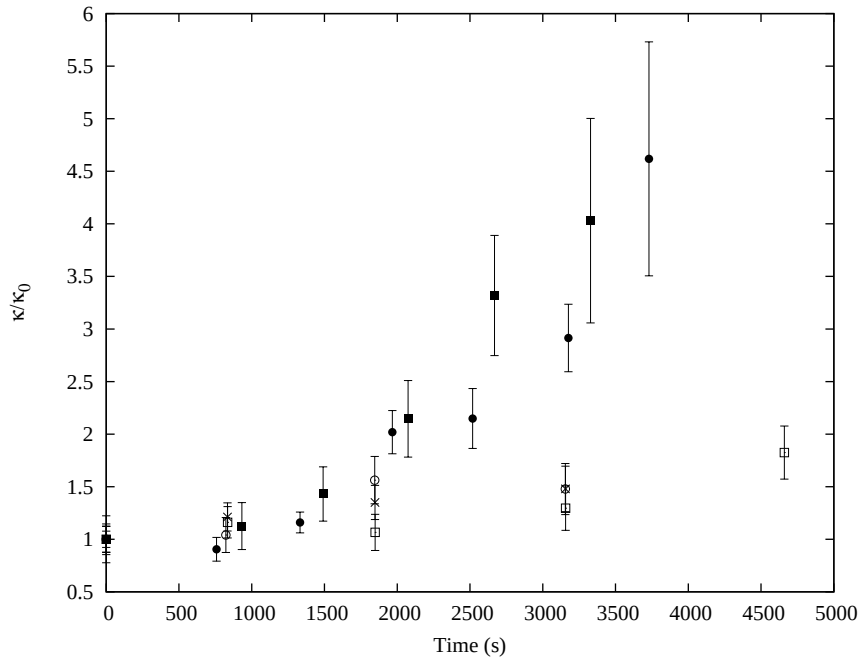

Figure 4.6: Bending modulus as a function of peroxide exposure time. The crosses and open symbols are H_2O_2 treated cells and the solid symbols are cumene hydroperoxide treated cells.

Despite the approximations made in comparing equation (4.8) to the experiment, the values of the bending modulus for the untreated cells are physically reasonable ($\kappa = (5.6 \pm 0.6) \times 10^{-19}$ J for six cells) and close to those obtained from the fitting of the simulation ($\kappa = 7.5 \times 10^{19}$ J).

The change in the bending modulus of the hydrogen peroxide treated cell is significantly smaller than that for the cumene hydroperoxide (Figure 4.1).

Cumene hydroperoxide is hydrophobic and preferentially inserts into the membrane, therefore its proximity to lipids is likely to initialise lipid peroxidation. Lipid per-

oxidation by the cumene hydroperoxide would saturate lipids resulting in higher packing densities and an increased bending modulus [107].

This picture is supported by the observations of the normalised mean contour radius $\langle R \rangle / \langle R_0 \rangle$ (Figure 4.7). The hydrogen peroxide treated cells show small and non-systematic change in their radius whereas the cumene hydroperoxide treated cells show a significant decrease in the mean radius. A decrease in the membrane area due to increased lipid packing density as a result of saturation of the fatty acid chains would explain the decrease in mean cell radius.

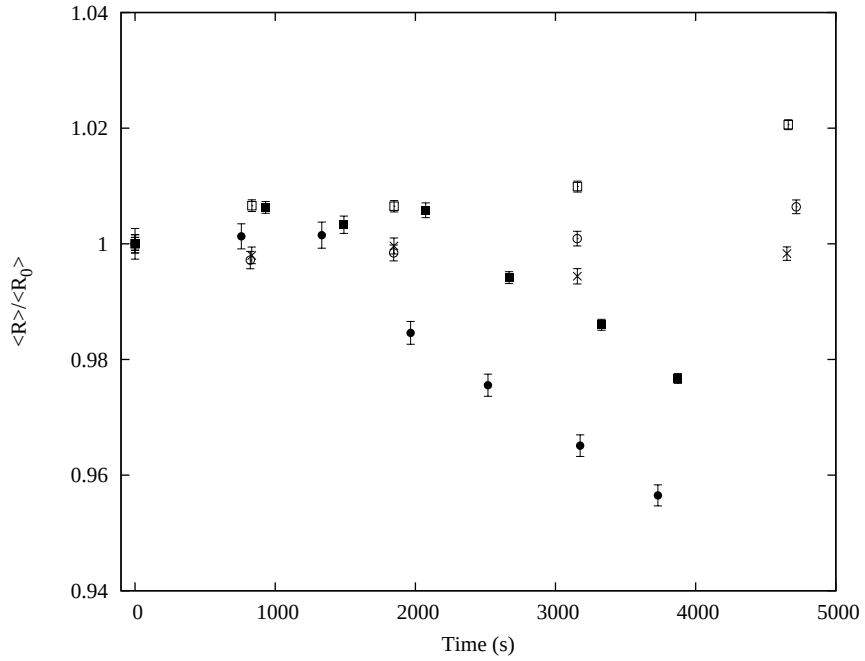

Figure 4.7: The normalised cell radius as a function of hydroperoxide exposure time. The crosses and open symbols are H_2O_2 treated cells and the solid symbols show cumene hydroperoxide treated cells.

In the later stages of oxidation, loss of area could be also due to vesiculation of the bilayer caused by spectrin detachment and band 3 clustering [96]. Our observations of the changes in the membrane bending modulus caused by the two oxidising agents agree well with results from biochemical studies. It was shown by [93, 97] that H_2O_2, being permeable to the membrane, causes only partial lipid peroxidation in the RBC. We see its signature in the two fold increase of κ (Figure 4.6). CumOOH, in contrast, oxidises the lipids to much greater extend [108, 93] due to its localisation

in the hydrophobic part of the lipid bilayer. We detect this through the ~ 5 fold increase in κ (Figure 4.6) accompanied with loss of membrane area (Figure 4.7).

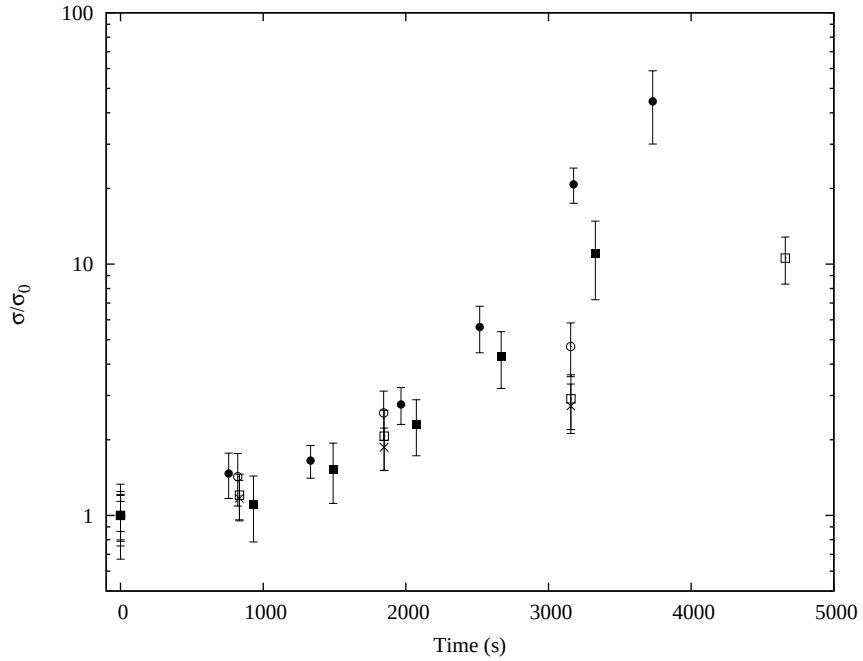

Figure 4.8: Membrane tension as a function of the peroxide exposure time. The crosses and open symbols are H_2O_2 treated cells and the solid symbols show cumene hydroperoxide treated cells.

Membrane tension increases in the course of oxidation in both cases. Most probably, this is caused by oxidation of the skeletal proteins (mainly spectrin), oxidation of haemoglobin and/or formation of haemoglobin-spectrin complexes which would result in the increase of the spectrin network shear modulus.

Again the effect of cumOOH appears to be more significant than that of H_2O_2. The membrane tension of the cumOOH treated cells increases to a value $\sim 80\times$ that of the untreated cell. Cells treated with H_2O_2 show an increase of only $\sim 10\times$ there initial value. This suggests the membrane skeletal proteins are oxidised more by the cumOOH than H_2O_2. This could be due to either different oxidising ability of the two peroxides or the increased effective concentration of cumOOH in the membrane close to the protein skeleton.

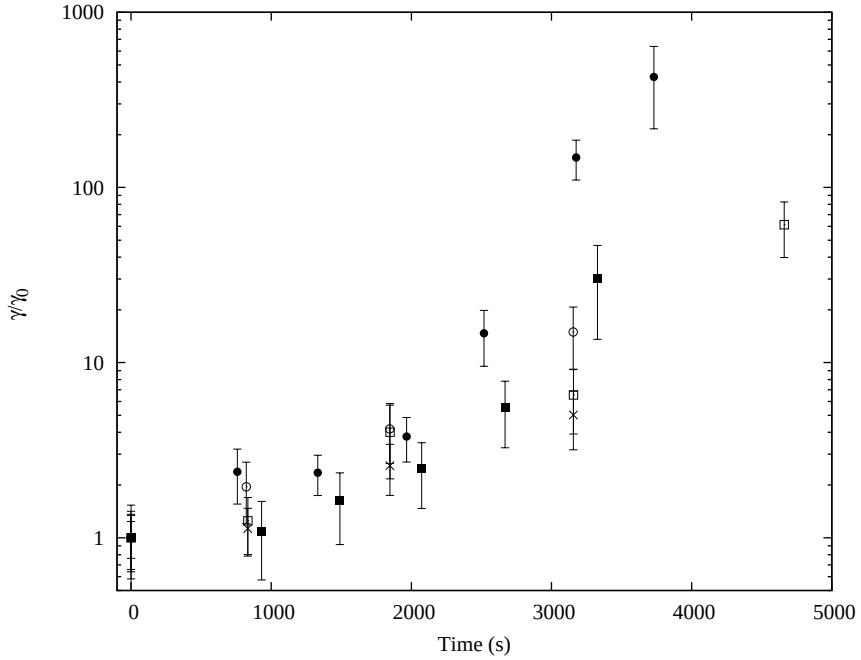

Figure 4.9: Confinement potential as a function of the peroxide exposure time. The crosses and open symbols are H_2O_2 treated cells and the solid symbols show cumene hydrogen peroxide treated cells.

The confinement potential follows a similar trend to the membrane tension. The reason appears to be the increased rigidity of the membrane skeleton ($\gamma \simeq \mu^2/\kappa$) most probably due to peroxide induced formation of haemoglobin-spectrin complexes [98].

4.6 Conclusion

Using the techniques developed in chapter 2 we were able to show it is possible to discriminate between the actions of different oxidising agents from their effect on the fluctuation spectra and radial fluctuations histograms of the cells.

We extracted comparative measures of the material properties by adapting a flat membrane theory [25] to provide a model for the fluctuation spectra. Using this approximate model we were able to show the effects of the different agents on the individual parameters and demonstrate clearly their effect on the different structural components of the membrane.

In the low mode number regime dominated by the effects of the confinement potential and membrane tension, both oxidants decrease the mean square fluctuations. These are parameters primarily associated with the properties of the membrane skeleton. These observations can be explained by the formation of spectrin haemoglobin complexes which increase the membrane skeleton rigidity.

However in the high mode regime, dominated by the bending rigidity which is primarily a property of the lipid bilayer, only cumene hydroperoxide has a significant effect on the fluctuations. This shows that to cumene hydroperoxide and hydrogen peroxide react differently with the lipid bilayer. Whilst H_2O_2 has a limited oxidising effect during the time of permeation through the membrane, cumOOH is able to affect the lipid bilayer to a greater extent (~ 5 fold increase in κ) due to the fact that it is membrane soluble.

The radial fluctuation histograms showed that the cumene hydroperoxide increased the rigidity of the membrane faster than hydrogen peroxide. Three possible conclusions could be drawn from this. Cumene hydroperoxide either is a more powerful oxidant or the structures oxidised by it have a greater effect of reducing the fluctuations or it is due to the high effective concentration in the membrane.

We can conclude the cumOOH, in equal concentration, oxidises the lipid bilayer significantly more than the hydrogen peroxide since cumOOH increases the bending modulus of the membrane significantly more than hydrogen peroxide. This is supported by the mean radius data indicating a decrease in the membrane area probably due to increased lipid saturation.

The confinement potential and membrane tension showed similar trends for both oxidants although the effect of cumene hydroperoxide was more pronounced. The reasons for these trends is that both oxidants target the spectrin mesh in a similar way and both oxidise haemoglobin close to the membrane proteins with the subsequent formation of spectrin-haemoglobin complexes.

The reproducibility of these results suggest the technique can provide a reliable means to access the damaging effects of ROS on the red blood cell and distinguish

differences between their effect on the membrane skeleton and the lipid bilayer. It would also provide a method to assess the potential protective properties of antioxidant agents, as demonstrated in the next chapter.

Chapter 5

Glycation and Diabetes

5.1 Introduction

Diabetes-specific microvascular disease is a leading cause of blindness, renal failure and nerve damage, and diabetes-accelerated atherosclerosis leads to increased risk of myocardial infarction, stroke and limb amputation [109]. There are currently over 2.5 million people with diabetes in the UK and there are more than half a million people with diabetes who have the condition and do not know it [110].

Insulin is a hormone produced by the pancreas and regulates the uptake of glucose into the cells. In diabetic individuals the body either fails to produce enough insulin, or does not respond to insulin, or both. As a result glucose accumulates in the blood and often leads to vascular complications [110].

These complications are believed in some part to be caused by the decreased deformability of the red blood cell due to glycation and oxidation of the structures of the membrane. Several studies report significant differences in the deformability of red cells in individuals with diabetes and diabetic complications compared to normal individuals [39, 111, 59, 112].

5.1.1 Glycation in the RBC

Reducing sugars such as glucose, react non enzymatically with amino groups in proteins, lipids and nucleic acids through a series of reactions involving the formation of Schiff bases and Amadori products to produce advanced glycation end-products (AGE). This process is also known as the Millard reaction and was described in the 1900s when it was noted that amino acids heated in the presence of reducing sugars developed a characteristic brown colour [113].

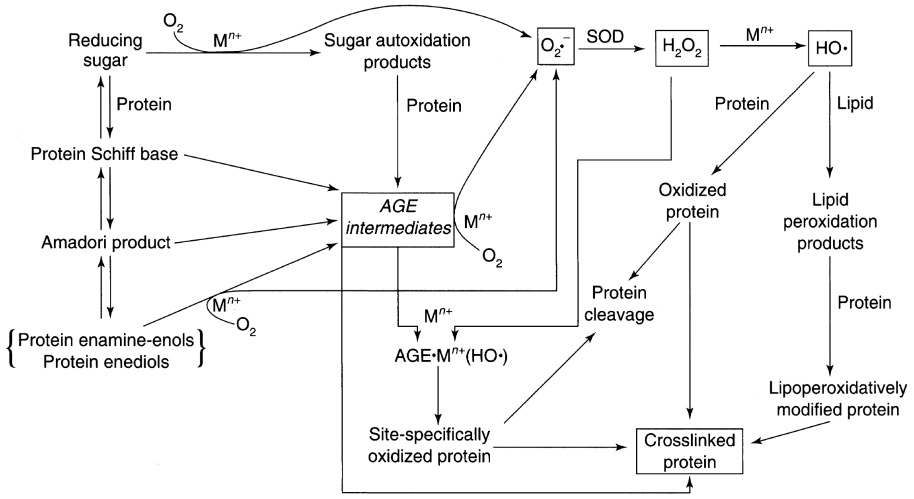

Figure 5.1: Flow diagram of AGE formation process [13]

Glycation begins with the reaction of a sugar carbonyl group with a primary amino group to form a Schiff base, followed by a rearrangement into the stable Amadori products. Whereas the mechanism of the early steps is well understood, the intermediate and late steps in the formation of AGEs and the influence of oxidative processes on the stages following the Amadori rearrangement are neither fully elucidated nor fully understood [114].

Formation of AGE is a slow reaction occurring over a period of weeks, thereby primarily affecting long lived proteins [113]. The most widely known Amadori product is a modification of haemoglobin (HbA1c), and this is used clinically as an indicator for cumulative exposure to elevated blood glucose in the context of diabetes [115]. This is due to the highly predictable relationship between plasma glucose

levels and the glycated form of haemoglobin (HbA1c) [116]. It has been shown that most, if not all, membrane proteins of the red blood cell that are separable on SDS gels (sodium dodecyl sulfate polyacrylamide gel electrophoresis) are modified with ketoamine linkages (an Amadori Product, see figure (XX)) by glucose [117].

Advanced glycation end products (AGEs) contribute to changes in protein conformation, loss of function, and irreversible cross-linking [114]. It is therefore likely that any such modifications of the membrane skeleton, in particular the spectrin mesh or its binding junctions to the bilayer, could have a significant impact on the shear modulus and consequently the deformability of the red blood cell. Schwartz et al. [59] using ektacytometry measured decreased deformability in diabetic individuals with complications and showed it also correlates with the amount of oxidised spectrin, which they hypothesise is due to glycation.

The lipid bilayer is also affected by glycation since phospholipids such as phosphatidylethanolamine and phosphatidylserine also possess reactive amino groups which can form lipid-linked AGEs and promoting fatty acid oxidation. Bucala et al. [118] have shown that lipid-advanced glycation and oxidation increase during the chronic hyperglycemia of diabetes, supporting the concept that AGE oxidation plays an important and perhaps primary role in initiating lipid oxidation in vivo. It is expected that lipid oxidation which would increase the level of lipid saturation would increase the bending modulus of the lipid bilayer [107].

It is likely that detailed study of the mechanical properties of the red blood cells affected by the high glucose will determine the effects of the associated glycation and oxidation on membrane structures and should elucidate the causes of decreased deformability in red cells of diabetic individuals. This chapter describes the application of the fluctuation analysis technique to this problem studying the effects simulated hyperglycemia on the membrane mechanical properties. We also present results on the response of such cells to oxidative damage, as well as the effects of one of the major anti-diabetic drugs, metformin, on the membrane mechanical properties.

5.2 Experimental Methods

5.2.1 Effect of different sugars

The time-course of glycation induced changes was established for glucose and ribose. Ribose is widely used in model studies to increase the rate of glycation by eliminating delays associated with breaking the ring structure of glucose.

Fresh blood samples were collected from healthy volunteers by pin pick lancet (Acc-Chek, Roche Ltd). The small volume, $\sim 5\,\mu$l, was immediately suspended in 1 ml of PBS buffer pH 7.4 (Oxoid Ltd, Basingstoke, UK) with 1 mg/ml BSA (Sigma-Aldrich, United Kingdom). Aliquots of equal concentrations of red cells were then resuspended in PBS buffers with glucose and ribose (Sigma-Aldrich, United Kingdom) at concentrations of 20 mM (corresponding to hyperglycemic concentrations: normal glucose concentrations $5 - 10$ mM). These were then incubated at 37 °C. Over a period of 3 days at regular intervals samples were taken and the fluctuation analysis performed. Each sample was then treated with 100 µM H_2O_2 and recorded at regular intervals of 10 minutes for a period of 90 minutes.

5.2.2 Effect of metformin

To investigate possible effects of metformin, we used the same procedure as above but resuspended the cells in PBS buffers containing 20 mM glucose or 20 mM glucose with 100 µM metformin (physiologically relevant concentration [119, 120]). All samples were then placed into an incubator at 37 °C. Over the period of 3 days samples from both preparations were taken and the fluctuation analysis performed. Each sample was then treated with 100 µM H_2O_2 and recorded at regular intervals of 10 minutes for a period of 90 minutes

5.2.3 Micropipette aspiration experiments

This method was used to obtain the static shear modulus of the cells from all preparations.

Micropipette fabrication

The micropipettes were pulled from borosilicate glass capillaries (Sutter Instrument Co, USA) with outer diameter of 1 mm on a Flaming/Brown micropipette puller Model P-87 (Sutter Instrument Co, USA). Using a trough element and the following three-stage program (Table 5.1). This consistently produced micropipettes with internal tip diameters of $0.5 - 2\,\mu m$ uniform over $100\,\mu m$ suitable for red blood cell aspiration.

Heat	Pull	Velocity	Time
RAMP	0	25	5
RAMP	0	25	5
RAMP+15	40	25	5

Table 5.1: Micropipette pulling program. The units are the arbitrary internal units of the puller and RAMP indicates the heat value of the "Ramp Test"

Pipette tips can be broken by impact on a hard surface but the chance of obtaining a square tip of the desired diameter are very small. A more successful method is described by Merrill and Ainsworth [121] and used to cut the pipette tip. This method uses a handmade forge consisting of a soda glass bead on a platinum wire under a microscope. The tip of the micropipette is brought into contact with the molten soda glass bead, the current is switched off and the tip is then cleanly broken as the molten glass bead solidifies and retracts.

Tip filling is a non-trivial task and many techniques exist in the literature. The most common technique relies simply on dipping the tip in the filling solution and leaving it overnight. Boiling under pressure or large suction exerted by a syringe followed by back filling with a syringe with a narrow needle is another approach

[122]. This technique has many problems, such as the long times required leading to buffer contamination with bacteria or dust blocking the pipettes. Ideally a more rapid technique is required. One technique tried in the process of this research with limited success involved back-filling and centrifuging the pipette as described by Cerf and Cerf [123]. A faster and more reliable method was developed for filling micropipettes as follows.

Pipettes were back filled using a "MicroFil" (World Precision Instruments (WPI), Inc, UK) syringe tip, dipped in the filling solution and then mounted on the forge. The micropipette tip was then filled by bring the tip close to the hot glass bead. This caused the solution in the tip to vapourise and the back fill solution to flow fully to the end of the pipette tip. The result is micropipettes that can be pulled, forged and filled in about 15 minutes. This reduces the risk of contamination due to dust and bacteria which often block the micropipette tips.

The observation chamber is a microscope slide with coverclip separated by a U-shaped section of Parafilm (Pechiney Plastic Packaging, USA), bonded together by heating briefly on a hot plate.

The micropipette is attached to a precisely adjustable pressure head, consisting of a reservoir of the buffer solution whose height can be varied by a micrometer. Finding the zero pressure is done by placing the tip close to a cell and changing pressure such that the cell neither moves towards nor away from the tip. The micropipette and microscope is earthed to avoid development of a potential across the tip, which could lyse the red blood cell. Hydraulic micromanipulators (Narishige, Japan) are used to precisely manoeuvre the micropipette tip. The microscope (Leica DMLFS upright microscope equipped with a 63×PL FLUOTAR phase contrast objective) and micromanipulators were all placed on an optical bench to avoid vibrations.

Experimentally the shear elastic modulus (μ) is measured by aspirating a small portion of the membrane into a micropipette with internal radius, R_p, of $0.5 - 0.75\,\mu m$. The length of tongue L in the micropipette is measured at increasing values of the applied pressure, ΔP. The theoretical model assumes the cell is aspirated

from the centre of the flat side of the red blood cell. The analysis yields the equation [124, 43, 122]

$$\frac{\Delta P R_p}{\mu} = \frac{2L}{R_p} - 1 + \ln\left(\frac{2L}{R_p}\right) \tag{5.1}$$

In the region $1 < L/R_p < 4$ a linear approximation can be made since the $\ln(2L/R_p)$ term has little influence. Therefore (5.1) becomes

$$\Delta P R_p = \mu\left(\frac{k_1 L}{R_p} - k_2\right) \tag{5.2}$$

with $k_1 = 2.45$ and $k_2 = 0.63$.

Observation with high numerical aperture optics is required to measure the small deformations of the order of 1 µm. Optical resolution is about 0.5 µm and therefore changes in dimensions can be more accurately determined than absolute dimensions. Magnification is increased using a digital video camera and although this does not increase resolution it does facilitate measurements.

It can be difficult to accurately measure the tip internal diameter using phase contrast microscopy. The micropipette acts as a cylindrical lens which leads to errors in the measurement to the internal diameter. A systematic over-estimate of 10 % generally occurs with direct microscopic observations [125]. Since the experiments are comparative this would not alter the trends, but does lead to errors in the absolute values for parameters such as the membrane shear modulus.

5.2.4 Diabetic samples

Fresh blood samples was taken from patients and immediately suspended in 1 ml of PBS buffer (pH 7.4) with 1 mg/ml BSA. The samples were kept refrigerated until analysis was performed. All analyses of the cells were carried out within 12 hours of the acquisition of the blood samples.

The fluctuation analysis was performed on 20 cells per sample and a total of 22 samples were used for the study. The study group consisted of a combination of 15

controls and 8 diabetic samples of which 16 were fasted and 7 non-fasted. All the samples diabetic and controls were obtained from the Peninsula Medical Centre for Diabetes Research, Exeter using a double blind procedure, by Dr. Jackie Whatmore.

5.3 Results

5.3.1 Effect of Glycation

Glucose is the least reactive of the aldose monosaccharides. The high stability of its ring structure (Figure 5.2) limits the potentially harmful effects of non-enzymatic glycation of proteins and has been linked to its role as the primary metabolic fuel [126]. Ribose is a more reactive analogue of glucose and is commonly used to investigate the rapid glycation of proteins [126]. The reaction rate for the fast stage of the Millard reaction from the protein amino group to the schiff base, k_1 is $0.6 \times 10^{-3}\,\mathrm{mM}^{-1}\mathrm{hr}^{-1}$ and $10.0 \times 10^{-3}\,\mathrm{mM}^{-1}\mathrm{hr}^{-1}$ for glucose and ribose respectively.

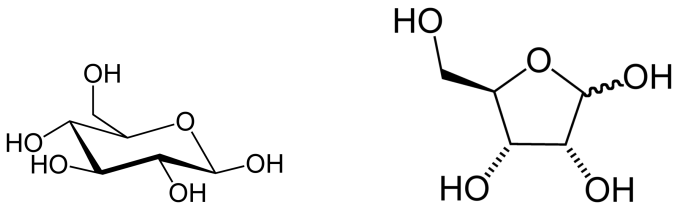

(a) D-Glucose (b) D-Ribose

Figure 5.2: Molecular structures of the sugars D-Glucose and D-Ribose

Glucose and ribose both glycate proteins via the Millard reaction. The aim of the following was to determine if the technique could detect a difference in glycation between the two sugars. The effect of glucose and ribose alone was shown to not significantly change the thermal fluctuations of the cell. But in combination with hydrogen peroxide the effects were obvious.

The fluctuation spectra were fitted with the equation (4.8) and comparative measures of the mechanical properties extracted.

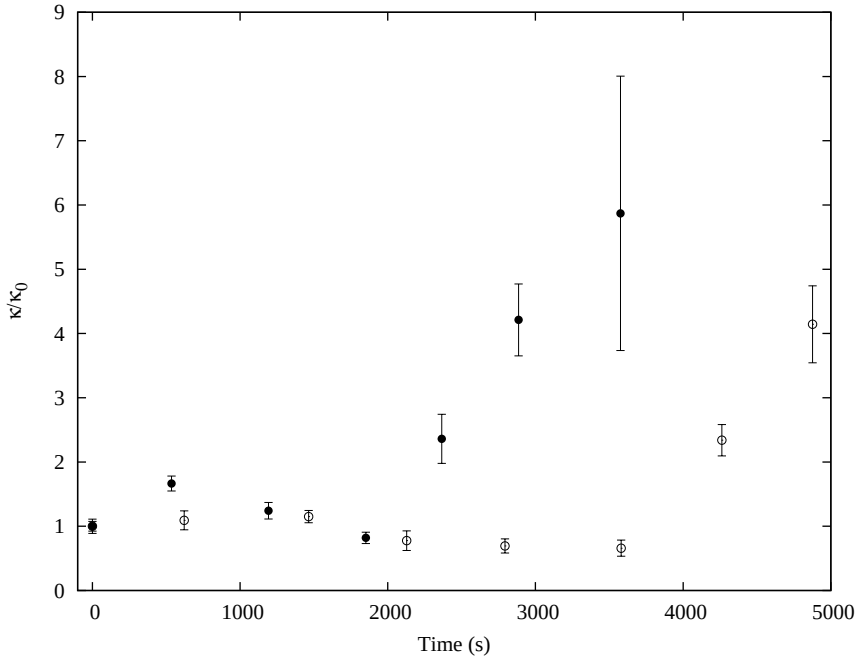

Figure 5.3: Bending modulus κ as a function of the exposure time to 100 µM H_2O_2. A cell incubated in a buffer of 20 mM glucose is shown by hollow symbols and a cell incubated in the an identical buffer but with 20 mM of ribose is shown with solid symbols.

The bending modulus κ is shown in figure 5.3, the most apparent difference between the ribose and glucose is the delay in the increase in the bending modulus. The bending modulus of the ribose treated cells starts to increase about 2000 seconds before the glucose treated cells. This suggests the glycation effect of ribose on the lipids is more extensive than that of glucose, which is not entirely unexpected since ribose is a more reactive sugar.

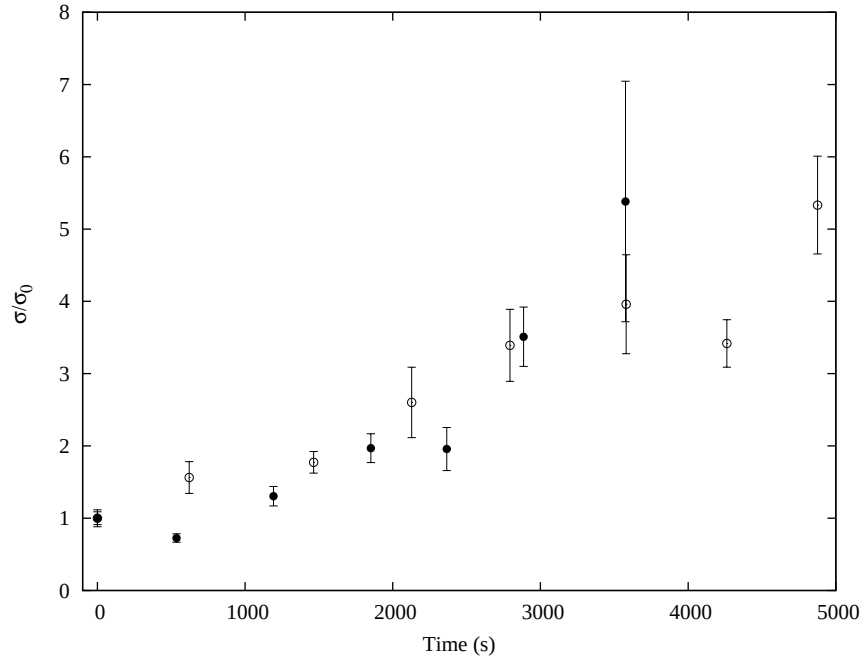

Figure 5.4: Membrane tension σ as a function of the exposure time to 100 µM H_2O_2. A cell incubated in a buffer of 20 mM glucose is shown by the hollow symbols and a cell incubated in the an identical buffer but with 20 mM of ribose is shown with solid symbols.

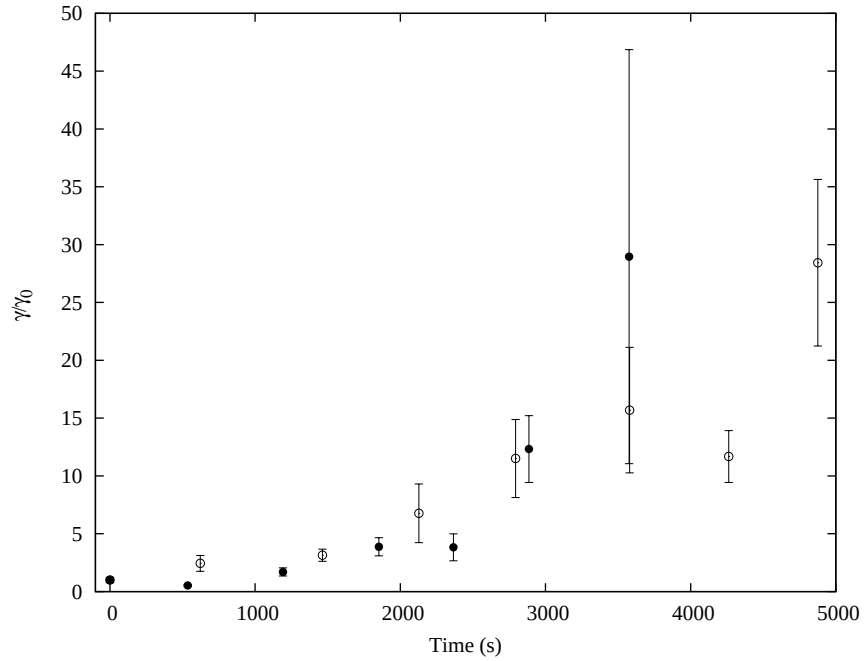

Figure 5.5: Confinement potential γ as a function of the exposure time to 100 µM H_2O_2. A cell incubated in a buffer of 20 mM glucose is shown by the hollow symbols and a cell incubated in the an identical buffer but with 20 mM of ribose is shown with solid symbols.

Membrane tension also increases on exposure to sugars but the difference in the effect of glucose and ribose on the membrane tension (Figure 5.4) and confinement potential (Figure 5.5) is less apparent as both show steady but significant increases.

The changes in the membrane tension and confinement potential are dominated by the membrane skeleton and so the results suggest that in this case opening of the glucose ring is not the rate limiting step. It is probable that intercellular reaction rates depend on the rate of transport across the membrane. Both ribose and glucose can cross the lipid bilayer directly; although the membrane is 10 times more permeable to ribose than glucose [127]. Glucose is also transported across the membrane via a protein as ribose is not [80].

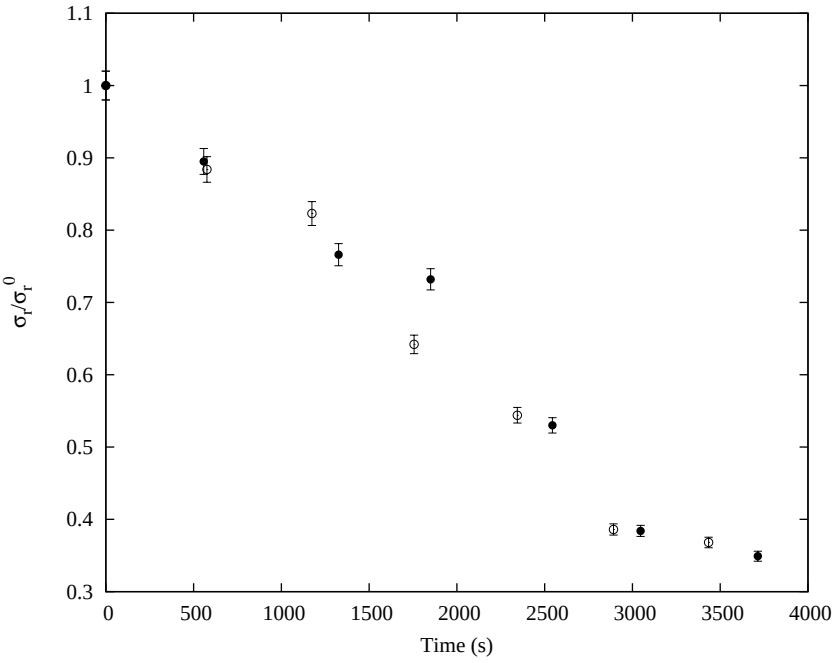

Figure 5.6: Normalised radial standard deviation as a function of the exposure time to 100 µM H_2O_2. A cell incubated in a buffer of 20 mM glucose is shown by the hollow symbols and a cell incubated in the an identical buffer but with 20 mM of ribose is shown with solid symbols. The errorbars are the uncertainty in the fitting of σ.

The normalised radial standard deviation of ribose and glucose treated cells appear not to deviate greatly from each other. This is due the dominate effect of the membrane tension on the radial fluctuations and for ribose and glucose and these differ little from each other.

5.3.2 Metformin

Metformin (N^1,N^1-dimethylbiguanide) is a common anti-diabetic drug and the first-line treatment of type 2 diabetes. Metformin is still a relatively new drug; first used in 1979 and only received approval in the US in 1994. Metformin increases the sensitivity of peripheral tissues to insulin. Recently it has been suggested that metformin has additional properties as an anti-glycation [128, 129, 130] and anti-oxidant agent [131].

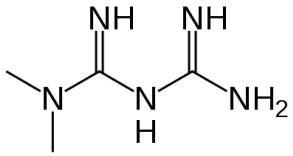

Figure 5.7: Molecular structure of Metformin

Here we have examined the effect of metformin on the glucose induced changes in the mechanical properties of the red blood cell membrane.

Figure 5.8 shows graphs of the normalised bending modulus as a function of exposure time to 100 µM H_2O_2 treatment. For the glucose treated cell κ remains relatively constant up to about 3500 seconds then increases rapidly to 4 times the cell's initial value. The metformin treated cell exhibits similar behaviour to the untreated cell except the rapid increase in bending occurs later at about 4500 seconds.

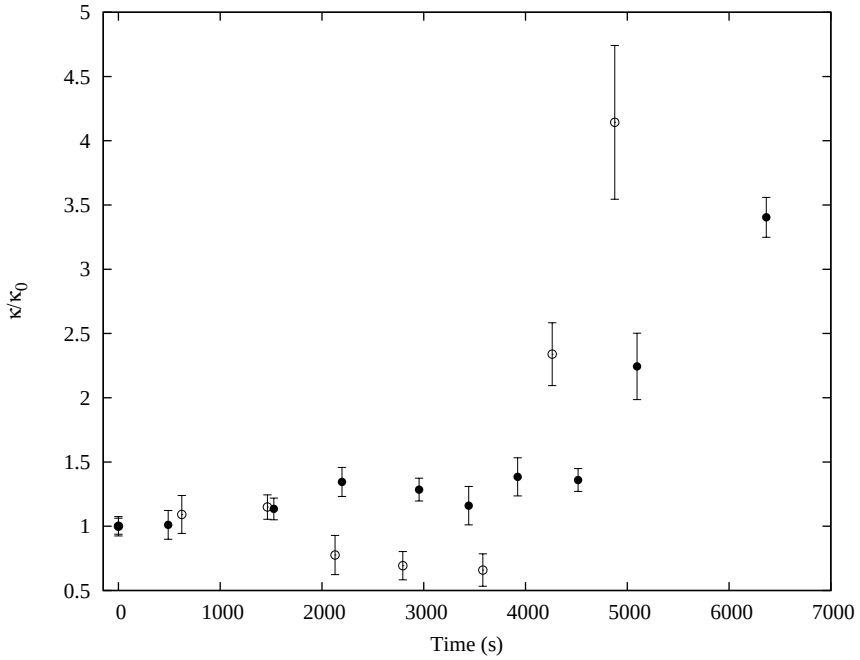

Figure 5.8: The bending modulus κ as a function of the exposure time to 100 µM H_2O_2. A cell incubated in a buffer of 20 mM glucose is shown by the hollow symbols and a cell incubated in the an identical buffer but with the addition of 100 µM metformin is shown with solid symbols.

Since the bending modulus is dominated by the lipid bilayer this would suggest the metformin is protecting the lipid part of the membrane, from either glycation by glucose or oxidation by H_2O_2. Metformin is known to accumulate in the red blood cell membrane and has been shown to effect the membrane fluidity [132]. It is possible therefore that metformin could act as a lipid soluble antioxidant in the same way as Vitamin E.

In Figure 5.9 the membrane tension σ for the cell incubated with glucose increases steadily in a linear fashion during the exposure increasing to 5 times its initial value. The cell treated with metformin shows a less pronounced increase, increasing to approximately 2.5-3 times its initial value.

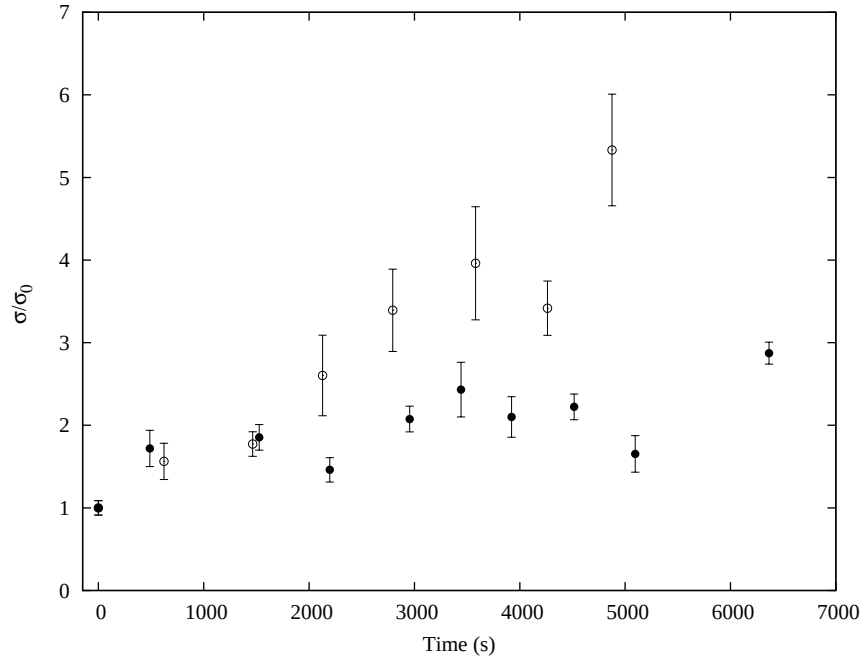

Figure 5.9: The membrane tension σ as a function of the exposure time to 100 µM H_2O_2. A cell incubated in a buffer of 20 mM glucose is shown by the hollow symbols and a cell incubated in the an identical buffer but with the addition of 100 µM metformin is shown with solid symbols.

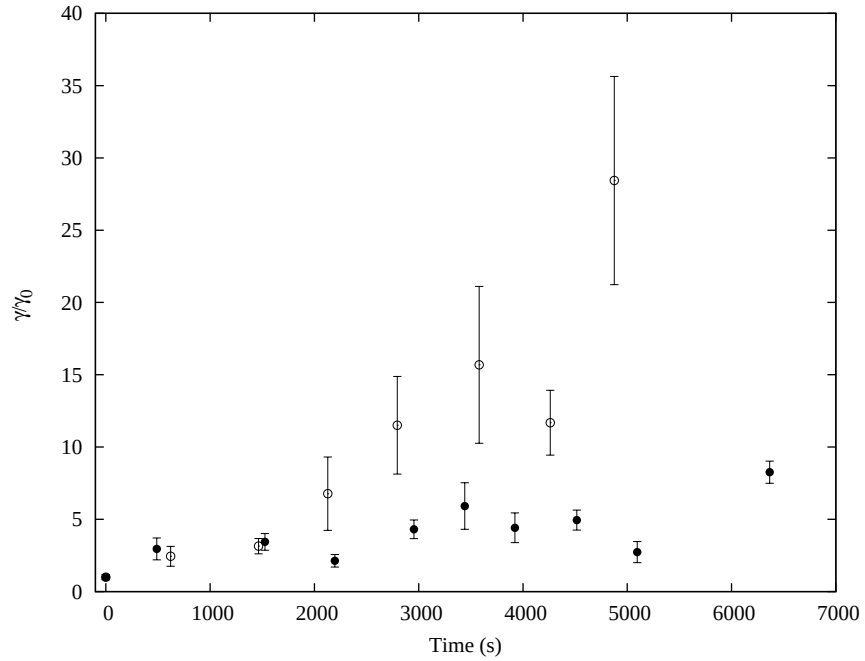

Figure 5.10: The membrane tension γ as a function of the exposure time to 100 µM H_2O_2. A cell incubated in a buffer of 20 mM glucose is shown by the hollow symbols and a cell incubated in the an identical buffer but with the addition of 100 µM metformin is shown with solid symbols.

This suggests the metformin is having a significant effect on the rate at which the membrane skeleton is being oxidised by the H_2O_2. This could be because metformin in the membrane is protecting the membrane skeleton by scavenging the H_2O_2 before it is able to penetrate the membrane.

The radial fluctuation histogram is an accurate measure of the overall fluctuation of the membrane and very sensitive to any stiffening of the membrane.

Figure 5.11 shows the standard deviation of the radial fluctuation histogram, as a function of time of H_2O_2 exposure, of glucose incubated cells treated and untreated with metformin. These graphs clearly show the untreated cell stiffens much faster than the metformin treated cell; the untreated cell radial fluctuations have decreased to half there initial value by approximately 3000s while the metformin treated cell fluctuation only decrease after about 6000s.

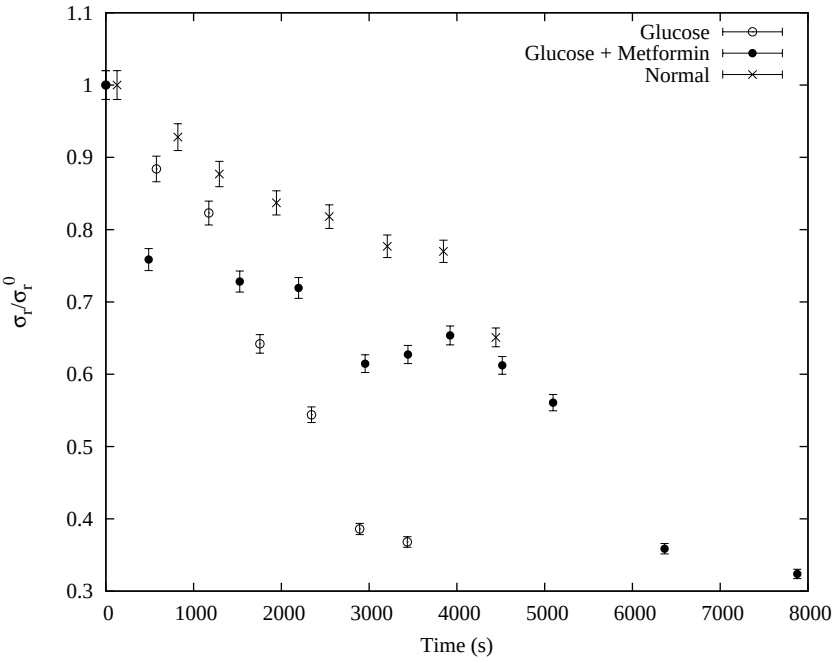

Figure 5.11: Normalised radial standard deviation σ_r/σ_r^0 as a function of the exposure time to 100 µM H_2O_2. A cell incubated in a buffer of 20 mM glucose is shown by the hollow symbols and a cell incubated in the an identical buffer but with the addition of 100 µM metformin is shown with solid symbols. The crosses are a control incubate for the same period without glucose or metformin.

5.3.3 Micropipette Aspiration

The shear modulus, μ, of cells incubated in glucose was measured and the effect of treatment with metformin examined. Typical micropipette aspiration results for red cells incubated in glucose treated and untreated with metformin are shown in figure 5.12.

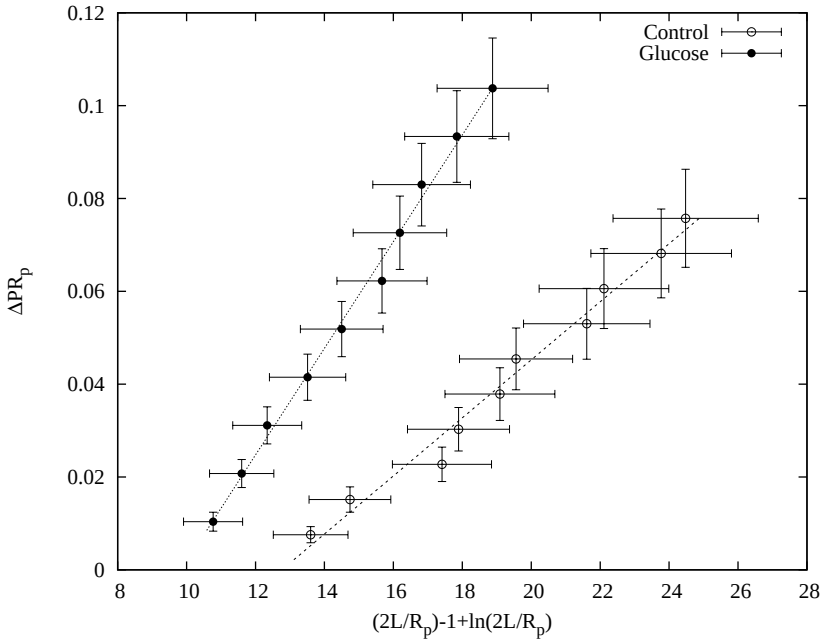

Figure 5.12: Typical micropipette aspiration results. (•) cell treated with 20 mM glucose, $\mu = 11.5\,\mathrm{mN/m}$ (○) untreated control $\mu = 11.5\,\mathrm{mN/m}$.

Below is table summarising the results of the experiments. Cells incubated with glucose have a much higher shear modulus that the normal controls suggesting than the membrane skeleton is stiffened by the glycation of the glucose. The cells treated with metformin alone show a small increase which may be due to an interaction between the metformin and the membrane skeleton. There is a large difference between the shear moduli of those of the metformin-treated and untreated cells incubated in glucose for 4 days.

Sample	μ shear modulus (mN/m)
Control	6.05 ± 0.66
Glucose	11.6 ± 1.34
Metformin	7.19 ± 0.45
Glucose + Metformin	9.37 ± 0.58

Table 5.2: Summary of shear moduli obtained using the micropipette aspiration technique for cells incubated with glucose and/or Metformin.

This clearly supports the results obtained from analysis of the thermal fluctuations suggesting a protective role of metformin, hindering glycation of the membrane skeleton proteins.

5.3.4 Diabetic cells

As discussed above the importance of the deformability of red cells in type 2 diabetes is widely reported. In the following experiments the fluctuations of cells from diabetic patients were examined to provide a comparison with normal cells subjected to acute exposure to glucose.

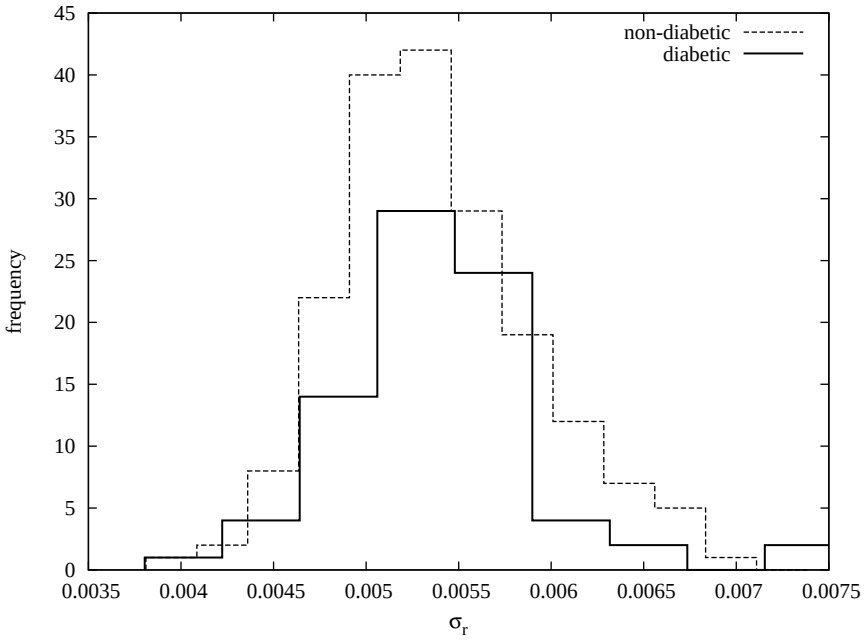

Figure 5.13: Histograms of the radial standard deviations σ_r for all cells from diabetic and non-diabetic samples. (80 cells from 8 diabetics, 180 cells from 15 normal controls)

Figure 5.13 shows the histogram of the radial standard deviation σ_r for all diabetic cells and another for all non-diabetic cells. There is no significant difference between the two groups of cells suggesting no difference in the mechanical properties of red bloods cell from diabetic individuals to those from non-diabetics.

This is still seen if the sample is split to fasting and non-fasting groups, the cells from diabetic individuals still appear not to differ from those of non-diabetics.

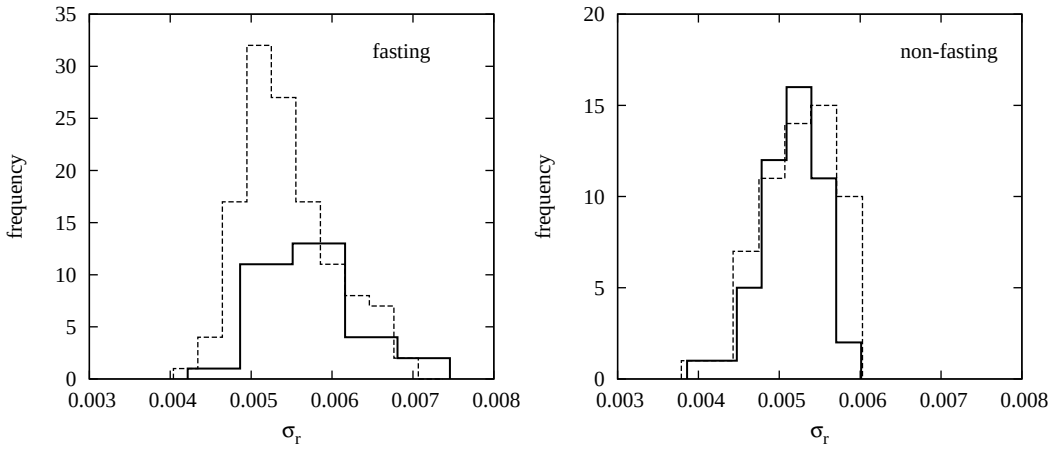

Figure 5.14: histograms of radial standard deviations σ_r. The data from figure 5.13 split into the fasting and non-fasting samples. The histograms on the left show the fasting sample (31 cells from 3 diabetics, 126 cells from 13 normal controls) and on the right the non-fasting sample (59 cells from 4 diabetics, 48 cells from 3 normal controls).

5.4 Conclusion

Glycation alone did not significantly change the measured thermal fluctuations of the cell, but in combination with hydrogen peroxide the effects of glycation were obvious. Cells incubated with glucose concentrations comparable to those in diabetic individuals stiffened significantly more rapidly than those which were not.

On treatment with hydrogen peroxide, the bending modulus increased significantly sooner for cells incubated in ribose rather than glucose. However, there is little difference in the reaction time of the confinement potential and membrane tension

between the two sugars. Suggesting while ribose reacts faster with the lipid bilayer than glucose the reaction rate of the two sugars with the membrane skeleton is very similar. More experiments are required to determine a mechanism for this effect which is probably due to the rate of transport across the membrane of the two sugars.

The different in the way ribose and glucose interact with membrane could potentially be use as a diagnostic to investigate glycation in the same way the cumene hydroperoxide and hydrogen peroxide for oxidative stress. It is also consistent with the long standing clinical observation that there is no significant changes in red cell deformability in patients without diabetic complications but an increase in those with complications [39, 59], which are likely to be associated with higher levels of oxidant activity [133]. The observations using fluctuation spectroscopy were consistent with micropipette measurements. Using this technique the shear moduli of the membrane skeleton was measured, the shear modulus increased dramatically in cells incubated in glucose, yet addition of metformin reduced this effect significantly.

The addition of metformin was found to protect cells incubated in glucose from the effects of accelerated oxidation. We believe the mechanism involves the inhibition of the glycation, by metformin [130]. Rahbar et al. [134] have shown metformin to be a potent inhibitor of glycation, possibly by its interaction with dicarbonyl compounds generated during the glycation process. Using assay methods specific for the early (Amadori) and late stages of glycation (post-Amadori) they have shown that metformin is a multistage inhibitor of glycation with greater effects in the post-Amadori stages. It has also been shown that metformin can act as a scavenger of ROS in particular hydroxyl and superoxide radicals [131]. This would prevent oxidation of the membrane lipids and the proteins of the membrane skeleton and therefore membrane stiffening. These results demonstrate the value of the technique in assessing the effects of drug induces changes to the red blood cell.

In our limit study of diabetics there was no statistical significant difference between the mechanical properties red bloods cells of diabetic subjects from those of normal controls. In hindsight this is probably not unexpected since the patient group was

selected not to have diabetic complications. Measurements on such a group would be a valuable extension of the present study.

Chapter 6

Conclusions and Future work

Described in this thesis is the development and application of a new technique to measure the mechanical properties of the red blood cell membrane.

Chapter 1 introduces the red blood cell describing the structures of the red blood cell membrane with an overview of the current understanding of how they relate to the mechanical properties and physiological function. The theoretical analysis of the red blood cell shapes and fluctuations are then discussed, which shows that with full consideration of the elastic properties of both the lipid bilayer and the membrane skeleton both properties can be faithfully modelled. This is followed by a review of the current techniques used to experimentally measure the elastic properties of the red blood cell membrane. Together, these sections suggest that, properly applied, an analysis of the fluctuation spectrum of the red blood cell can provide a comprehensive description of its mechanical properties their structural determinants under normal and pathological conditions.

In Chapter 2 the development and implementation of a new technique to extract the elastic properties of the red blood cell membrane from its thermal fluctuations is presented. A robust image analysis techniques is developed to reliably and precisely extract the equatorial contours. Also described is the analysis of the contours to determine the fluctuation spectra from which it is possible to extract the elastic properties of the red blood cell membrane.

We demonstrated the sensitivity of this method in single cell measurements which revealed the wide variation in the fluctuation spectra across a population of cells. We went on to investigate the effects of temperature and excess area on the fluctuation spectra, since these are the only other parameters other that the mechanical properties of the membrane which enter into the theoretical calculations of the thermal fluctuations of the membrane. We observed a decrease in the thermal fluctuations with reduction of the excess area as expected. However, results for the temperature dependence of the thermal fluctuations were unexpected in showing increases in the thermal fluctuations in the bending dominated part of the fluctuation spectrum ($n > 6$) but a reduction in the fluctuations in the low mode regime dominated by the confinement potential ($n < 6$).

However, these results are consistent with the theoretical models for the interaction between the membrane skeleton and the lipid bilayer[25]. Supporting experimental evidence for fluctuation suppressing interaction of the membrane skeleton on the lipid bilayer as proposed by Gov et al. [25].

In chapter 3 we simulated the equilibrium thermal fluctuations of the red blood cell using coarse grained molecular dynamics computer simulations. The simulations faithfully reproduces the average cell discotic shapes and correctly describes the mean square fluctuations of the equatorial contours of RBCs. Applying the analysis procedures developed in Chapter 2 we were able to directly compare the fluctuation spectra derived from experimental data to those from simulated cells, obtaining physically meaningful values for the elastic membrane parameters.

Comparison between experimentally and computationally obtained fluctuation spectra shows that they are in agreement with values of the spring constant $k_s \sim 8.3 \times 10^{-6}\,\mathrm{Nm}^{-1}$ and the dihedral constant $D = 1.3 \times 10^{-18}\,\mathrm{J}$. This allows an order of magnitude estimation of the (zero-temperature) shear and bending moduli using the approximate relationships reported in the literature, [36, 33] $\mu \approx (\sqrt{3}/4)k_s$ and $\kappa = D/\sqrt{3}$, giving $\mu = 3.6 \times 10^{-6}\,\mathrm{Nm}^{-1}$ and $\kappa = 7.5 \times 10^{-19}\,\mathrm{J}$. This represents good agreement with the literature.

In the chapters that followed we employed the technique to investigate the changes of the mechanical properties of the red blood cells in response to oxidative stress, hyperglycemic conditions, an anti-diabetic drug and diabetes.

In Chapter 4 we showed that using these techniques developed in Chapter 2 we were able to show that it is possible to discriminate between the actions of different oxidising agents from their effect on the fluctuation spectra and radial fluctuations histograms of the cells. We extracted comparative measures of the material properties by adapting a flat membrane theory [25] to provide a model for the fluctuation spectra. Using this approximate model we were able to quantify the effects of the different agents on the individual parameters and demonstrate clearly their effect on the different structural components of the membrane. In the low mode number regime, dominated by the effects of the confinement potential and membrane tension, both oxidants decrease the mean square fluctuations. These are parameters primarily associated with the properties of the membrane skeleton. These observations can be explained by the formation of spectrin-haemoglobin complexes which increase the membrane skeleton rigidity. However in the high mode number regime, dominated by the bending rigidity which is primarily a property of the lipid bilayer, only cumene hydroperoxide has a significant effect on the fluctuations. This shows that cumene hydroperoxide and hydrogen peroxide react differently with the lipid bilayer. Whilst hydrogen peroxide has a limited oxidising effect during the time of permeation through the membrane, cumene hydroperoxide is able to affect the lipid bilayer to a greater extend (~ 5 fold increase in κ) due to its much greater partition coefficient in the membrane. We conclude the cumene hydroperoxide, in equal molar concentration, oxidises the lipid bilayer significantly more than the hydrogen peroxide since it increases the bending modulus of the membrane significantly more. This is supported by the data on changes in mean radius of the cell indicating a decrease in the membrane area probably due to increased lipid saturation. The radial fluctuation histograms further confirmed that the cumene hydroperoxide increased the rigidity of the membrane faster than hydrogen peroxide.

In Chapter 5 we showed that the technique can also discriminate between the actions

of different sugars. On treatment with hydrogen peroxide, the bending modulus increased significantly sooner for cells incubated in ribose than glucose. However, there is little difference in the reaction time of the confinement potential and membrane tension between the two sugars. Suggesting while ribose reacts faster with the lipid bilayer than glucose the reaction rate of the two sugars with the membrane skeleton is very similar. More experiments are required to determine a mechanism for this effect which is probably due to the difference in membrane transport and relative membrane permeability of the two sugars.

Glycation alone did not significantly change the measured thermal fluctuations of the cell, but in combination with hydrogen peroxide the effects of glycation were obvious. Cells incubated with glucose concentrations comparable to those in diabetic individuals stiffened significantly more rapidly than those which were not. This suggests that glycation of the proteins of the membrane skeleton in particular spectrin makes them more susceptible to oxidation. The different in the way ribose and glucose interact with membrane could potentially be use as a diagnostic to investigate glycation in the same way the cumene hydroperoxide and hydrogen peroxide for oxidative stress. It is also consistent with the long standing clinical observation that there is no significant changes in red cell deformability in patients without diabetic complications but an increase in those with complications [39, 59], which are likely to be associated with higher levels of oxidant activity [133]. The observations using fluctuation spectroscopy were consistent with micropipette measurements. Using this technique the shear moduli of the membrane skeleton was measured, the shear modulus increased dramatically in cells incubated in glucose, yet addition of metformin reduced this effect significantly.

The addition of metformin was found to protect cells incubated in glucose from the effects of accelerated oxidation. We believe the mechanism involves the inhibition of the glycation, by metformin [130]. Rahbar et al. [134] have shown metformin to be a potent inhibitor of glycation, possibly by its interaction with dicarbonyl compounds generated during the glycation process. It has also been shown that metformin can act as a scavenger of ROS in particular hydroxyl and superoxide radicals [131]. This

would prevent oxidation of the membrane lipids and the proteins of the membrane skeleton and therefore membrane stiffening.

In our limited study of diabetics there was no statistical significant difference between the mechanical properties red bloods cells of diabetic subjects from those of normal controls. In hindsight this is probably not unexpected since the patient group was selected not to have diabetic complications. Measurements on such a group would be a valuable extension of the present study.

In summary in we have developed and demonstrated a new technique to determine the mechanical properties for the red blood cell and this technique reveals subtle changes that occur due to oxidative stress and glycation in a hyperglycemic diabetic red cell. The technique provides a reproducible means to assess the effects of ROS on the red blood cell and distinguish between effects on the membrane skeleton and the lipid bilayer. Fluctuation spectroscopy is of potential value in monitoring the effects of drug induced changes hence assessing the antioxidant or anti-glycation properties of drug treatments in diabetes or other conditions.

6.1 Future Work

6.1.1 Methodological Refinements

RBC fluctuation analysis

It may be possible in future to improve the quality of the fluctuation spectra by taking advantage of technological improvements. The camera employed in the present work employed a relativity insensitive CMOS sensor. The rapid development in the consumer market for cheap effective cameras has resulted modern CMOS chips which are much better. More expensive low light CCDs chips camera would also offer significant improvement over the current device. This improved optical sensitivity would enable faster shutter speeds improving the accuracy of the fluctuation

spectrum at high modes. Also improved dynamic range would reduce any errors in determining the membrane position. Many advanced CCD devices also offer very high frame rates and the possibility of investigating the rapid dynamics of the thermal fluctuations of the membrane.

Simulation

Coarse grained molecular dynamics modelling was invaluable in interpreting the fluctuation spectra. Further work is underway in our laboratories exploring comprehensively the parameter space of the simulation through variations in the values of the interaction potential parameters, volume to area ratio and the size of the simulated mesh, which will allow fast quantification of the elastic constants of any RBC.

The computer simulation did not perform as a well as hoped the uncertainties in the simulation results were greater than those of the experiment data. The present model struggled to maintain constant temperature with large values of the dihedral and spring constants, which maybe solved by either less restrictive or improved area and volume constraints and modification to the thermal bath.

Monte Carlo methods have been applied to fluctuating vesicles [135, 5] and Lattice Boltzmann techniques to model the large deformations in optical tweezers experiments [136]. Employing of these alternative simulation methods to the simulation of red blood cell fluctuations may offer improvements over the current method.

6.1.2 Applications

Membrane mechanics

Another important area of research would be to explore the relationship between changes in the mechanical properties determining the fluctuation spectrum and

changes in other physical properties such as membrane fluidity and membrane potential. This could be done using the range of fluorescent probes now available such as the molecular rotor DCVJ [137] to investigate membrane fluidity and probes such as di-8-ANEPPS to investigate membrane potential changes [138].

Oxidative stress

Oxidative stress is a major area of research in both biology and medicine and comprehensive understanding of its effects as the cell membrane is urgently required. We have shown fluctuation spectroscopy is able to distinguish the effects of different oxidants. This could be used to probe the antioxidant properties of molecules in different parts of the membrane. Useful to study the natural antioxidant defences of the red blood cell or the effects of endogenous agents such as drugs and antioxidant supplements.

Glycation and diabetes

As shown in Chapter 6 the red bloods cell fluctuation analysis technique can readily monitor the effects of the diabetic drug metformin. Obvious extensions of the project would be to extend the use of the technique into a clinical environment monitoring the effect of diabetic drugs on patients at various stages of the disease.

The relative simplicity of implementation of this method and the possibility of full automation would make it feasible to study large populations in a clinical environment, opening a range of possible screening, monitoring and research applications.

Bibliography

[1] B. Alberts. *Essential cell biology.* Garland Science, 2003.

[2] W.T. Tse and S.E. Lux. Red blood cell membrane disorders. *British Journal of Haematology*, 104(1):2–13, 1999.

[3] T. J. Byers and D. Branton. Visualization of the protein associations in the erythrocyte membrane skeleton. *Proceedings of the National Academy of Sciences*, 82(18):6153–6157, 1985.

[4] H. G. Döbereiner. Properties of giant vesicles. *Current Opinion in Colloid & Interface Science*, 5(3-4):256–263, 2000.

[5] H. G. Döbereiner, G. Gompper, C. K. Haluska, D. M. Kroll, P. G. Petrov, and K. A. Riske. Advanced flicker spectroscopy of fluid membranes. *Physical Review Letters*, 91(4), 2003.

[6] J. Stuart. Erythrocyte rheology. *British Medical Journal*, 38(9):965–977, 1985.

[7] R. E. Waugh and P. Agre. Reductions of erythrocyte-membrane viscoelastic coefficients reflect spectrin deficiencies in hereditary spherocytosis. *Journal of Clinical Investigation*, 81(1):133–141, 1988.

[8] H. Engelhardt and E. Sackmann. On the measurement of shear elastic moduli and viscosities of erythrocyte plasma membranes by transient deformation in high frequency electric fields. *Biophysical Journal*, 54(3):495–508, 1988.

[9] J. Guck, R. Ananthakrishnan, H. Mahmood, T. J. Moon, C. C. Cunningham,

and J. Kas. The optical stretcher: A novel laser tool to micromanipulate cells. *Biophysical Journal*, 81(2):767–784, 2001.

[10] J. Sleep, D. Wilson, R. Simmons, and W. Gratzer. Elasticity of the red cell membrane and its relation to hemolytic disorders: an optical tweezers study. *Biophysical Journal*, 77(6):3085–3095, 1999.

[11] M. Puig-de Morales, K. T Turner, J. P Butler, J. J Fredberg, and S. Suresh. Viscoelasticity of the human red blood cell. *J. Appl. Physiol*, 293:597–605, 2007.

[12] A. Zilker, H. Engelhardt, and E. Sackmann. Dynamic reflection interference contrast (ric-) microscopy - a new method to study surface excitations of cells and to measure membrane bending elastic-moduli. *Journal De Physique*, 48 (12):2139–2151, 1987.

[13] M. A. Smith, C. A. Rottkamp, A. Nunomura, A. K. Raina, and G. Perry. Oxidative stress in alzheimer's disease. *Biochimica Et Biophysica Acta-Molecular Basis Of Disease*, 1502(1):139–144, 2000.

[14] H.M. Van Dort, D.W. Knowles, J.A. Chasis, G. Lee, N. Mohandas, and P.S. Low. Analysis of integral membrane protein contributions to the deformability and stability of the human erythrocyte membrane. *Journal of Biological Chemistry*, 276(50):46968, 2001.

[15] X. An, X. Guo, H. Sum, J. Morrow, W. Gratzer, and N. Mohandas. Phosphatidylserine binding sites in erythroid spectrin: Location and implications for membrane stability. *Biochemistry*, 43(2):310–315, 2004.

[16] W. Diakowski and A.F. Sikorski. Brain spectrin exerts much stronger effect on anionic phospholipid monolayers than erythroid spectrin. *BBA-Biomembranes*, 1564(2):403–411, 2002.

[17] W. Helfrich. Elastic properties of lipid bilayers: theory and possible experiments. *Zeitschrift für Naturforschung. Teil C: Biochemie, Biophysik, Biologie, Virologie*, 28(11):693–703, 1973.

[18] F. C Frank. I. liquid crystals. on the theory of liquid crystals. *Discussions of the Faraday Society*, 25:19–28, 1958.

[19] A. G Petrov and I. Bivas. Elastic and flexoelectric aspects of out-of-plane fluctuations in biological and model membranes. *Prog. Surf. Sci*, 16:389–512, 1984.

[20] L. Miao, U. Seifert, M. Wortis, and H.G. Döbereiner. Budding transitions of fluid-bilayer vesicles: the effect of area-difference elasticity. *Physical Review E*, 49(6):5389–5407, 1994.

[21] M. P. Sheetz and S. J. Singer. Biological membranes as bilayer couples. a molecular mechanism of drug-erythrocyte interactions. *Proceedings of the National Academy of Sciences*, 71(11):4457–4461, 1974.

[22] H. G. Döbereiner, E. Evans, M. Kraus, U. Seifert, and M. Wortis. Mapping vesicle shapes into the phase diagram: A comparison of experiment and theory. *Physical Review E*, 55(4):4458–4474, 1997.

[23] W. Wintz, HG Döbereiner, and U. Seifert. Starfish vesicles. *Europhysics Letters*, 33(5):403–408, 1996.

[24] H. W. G. Lim, M. Wortis, and R. Mukhopadhyay. Stomatocyte-discocyte-echinocyte sequence of the human red blood cell: Evidence for the bilayer-couple hypothesis from membrane mechanics. *Proceedings of the National Academy of Sciences of the United States of America*, 99(26):16766–16769, 2002.

[25] N. Gov, A. G. Zilman, and S. Safran. Cytoskeleton confinement and tension of red blood cell membranes. *Physical Review Letters*, 90(22), 2003.

[26] L. C. L. Lin and F. L. H. Brown. Brownian dynamics in fourier space: Membrane simulations over long length and time scales. *Physical Review Letters*, 93(25), 2004.

[27] L. C. L. Lin and F. L. H. Brown. Dynamic simulations of membranes with cytoskeletal interactions. *Physical Review E*, 72(1):11910, 2005.

[28] D. H. Boal. *Mechanics of the Cell*. Cambridge Univ Pr, 2002.

[29] J. Pecreaux, H. G. Dobereiner, J. Prost, J. F. Joanny, and P. Bassereau. Refined contour analysis of giant unilamellar vesicles. *European Physical Journal E*, 13(3):277–290, 2004.

[30] M. B. Schneider, J. T. Jenkins, and W. W. Webb. Thermal fluctuations of large quasi-spherical bimolecular phospholipid-vesicles. *Journal De Physique*, 45(9):1457–1472, 1984.

[31] G. Marcelli, K. H. Parker, and C. P. Winlove. Thermal fluctuations of red blood cell membrane via a constant-area particle-dynamics model. *Biophysical Journal*, 89(4):2473–2480, 2005.

[32] Y. Kantor and D.R. Nelson. Crumpling transition in polymerized membranes. *Physical Review Letters*, 58(26):2774–2777, 1987.

[33] G. Gompper and D. M. Kroll. Random surface discretizations and the renormalization of the bending rigidity. *Journal De Physique I*, 6(10):1305–1320, 1996.

[34] W. Smith and T. R. Forester. The dl_poly molecular simulation package, 1999.

[35] S. Tuvia, S. Levin, A. Bitler, and R. Korenstein. Mechanical fluctuations of the membrane-skeleton are dependent on f-actin atpase in human erythrocytes. *Journal of Cell Biology*, 141(7):1551–1561, 1998.

[36] D. E. Discher, D. H. Boal, and S. K. Boey. Phase transitions and anisotropic responses of planar triangular nets under large deformation. *Physical Review E*, 55(4):4762–4772, 1997.

[37] A. Teitel and I. Radulescu. *Medicina Interna*, 5(32), 1952. In Roumanian.

[38] C. T. Nicolau, P. Teitel, and M. Fotino. Loss of plasticity of erythrocytes coated with incomplete antibodies. 1959.

[39] A. J. Barnes, P. Locke, P. R. Scudder, T. L. Dormandy, J. A. Dormandy, and J. Slack. Is hyperviscosity a treatable component of diabetic microcirculatory disease? *Lancet*, 2(8042):789, 1977.

[40] W. Groner, N. Mohandas, and M. Bessis. New optical technique for measuring erythrocyte deformability with the ektacytometer. *Clinical Chemistry*, 26(10): 1435–1442, 1980.

[41] E. A. Evans, R. Waugh, and L. Melnik. Elastic area compressibility modulus of red cell membrane. *Biophysical Journal*, 16(6):585–595, 1976.

[42] E. A. Evans and R. Waugh. Osmotic correction to elastic area compressibility measurements on red cell membrane. *Biophysical Journal*, 20(3):307–313, 1977.

[43] R. Waugh and EA Evans. Thermoelasticity of red blood cell membrane. *Biophysical Journal*, 26(1):115–131, 1979.

[44] E. A. Evans. Bending elastic modulus of red blood cell membrane derived from buckling instability in micropipet aspiration tests. *Biophysical Journal*, 43(1):27–30, 1983.

[45] J. Guck, R. Ananthakrishnan, C. C. Cunningham, and J. Kas. Stretching biological cells with light. *Journal of Physics-Condensed Matter*, 14(19):4843–4856, 2002.

[46] S. Hénon, G. Lenormand, A. Richert, and F. Gallet. A new determination of the shear modulus of the human erythrocyte membrane using optical tweezers. *Biophysical Journal*, 76(2):1145–1151, 1999.

[47] K. H. Parker and C. P. Winlove. The deformation of spherical vesicles with permeable, constant-area membranes: application to the red blood cell. *Biophysical Journal*, 77(6):3096–3107, 1999.

[48] G. Lenormand, S. Hénon, A. Richert, J. Siméon, and F. Gallet. Direct measurement of the area expansion and shear moduli of the human red blood cell membrane skeleton. *Biophysical Journal*, 81(1):43–56, 2001.

[49] A.Y. Krol, MG Grinfeldt, SV Levin, and AD Smilgavichus. Local mechanical oscillations of the cell surface within the range 0.2–30 hz. *European Biophysics Journal*, 19(2):93–99, 1990.

[50] Y. Alster, A. Loewenstein, S. Levin, M. Lazar, and R. Korenstein. Low-frequency submicron fluctuations of red blood cells in diabetic retinopathy. *Archives of Ophthalmology*, 116(10):1321–1325, 1998.

[51] H. Strey, M. Peterson, and E. Sackmann. Measurement of erythrocyte membrane elasticity by flicker eigenmode decomposition. *Biophysical Journal*, 69 (2):478–488, 1995.

[52] G. Popescu, T. Ikeda, C. A. Best, K. Badizadegan, R. R. Dasari, and M. S. Feld. Erythrocyte structure and dynamics quantified by hilbert phase microscopy. *Journal of Biomedical Optics*, 10(6), 2005.

[53] G. Popescu, K. Badizadegan, R. R. Dasari, and M. S. Feld. Observation of dynamic subdomains in red blood cells. *Journal of Biomedical Optics*, 11(4), 2006.

[54] G. Popescu, T. Ikeda, K. Goda, C. A. Best-Popescu, M. Laposata, S. Manley, R. R. Dasari, K. Badizadegan, and M. S. Feld. Optical measurement of cell membrane tension. *Physical Review Letters*, 97(21), 2006.

[55] F. Brochard and J. F. Lennon. Frequency spectrum of flicker phenomenon in erythrocytes. *Journal De Physique*, 36(11):1035–1047, 1975.

[56] Mary L. Ellsworth, Christopher G. Ellis, Daniel Goldman, Alan H. Stephenson, Hans H. Dietrich, and Randy S. Sprague. Erythrocytes: Oxygen sensors and modulators of vascular tone. *Physiology*, 24(2):107–116, 2009.

[57] V. Bennett. The spectrin-actin junction of erythrocyte membrane skeletons. *BBA-Reviews on Biomembranes*, 988(1):107–121, 1989.

[58] G. M. Wagner, D. T. Y. Chiu, J. H. Qju, R. H. Heath, and B. H. Lubin. Spectrin oxidation correlates with membrane vesiculation in stored rbcs. *Blood*, 69(6):1777–1781, 1987.

[59] R. S. Schwartz, J. W. Madsen, A. C. Rybicki, and R. L. Nagel. Oxidation of spectrin and deformability defects in diabetic erythrocytes. *Diabetes*, 40(6): 701–708, 1991.

[60] R. M. Hochmuth, N. Mohandas, and P. L. Blackshear. Measurement of the elastic modulus for red cell membrane using a fluid mechanical technique. *Biophysical Journal*, 13(8):747–762, 1973.

[61] M. Dao, CT Lim, and S. Suresh. Mechanics of the human red blood cell deformed by optical tweezers. *Journal of the Mechanics and Physics of Solids*, 51(11-12):2259–2280, 2003.

[62] M. Dao, C.T. Lim, and S. Suresh. Mechanics of the human red blood cell deformed by optical tweezers [journal of the mechanics and physics of solids, 51 (2003) 2259-2280]. *Journal of the Mechanics and Physics of Solids*, 53(2): 493 – 494, 2005.

[63] A. Zilker, M. Ziegler, and E. Sackmann. Spectral-analysis of erythrocyte flickering in the 0.3-4-mu-m-1 regime by microinterferometry combined with fast image-processing. *Physical Review A*, 46(12):7998–8002, 1992.

[64] J. B. Fournier, D. Lacoste, and E. Raphael. Fluctuation spectrum of fluid membranes coupled to an elastic meshwork: Jump of the effective surface tension at the mesh size. *Physical Review Letters*, 92(1), 2004.

[65] M. A. Peterson, H. Strey, and E. Sackmann. Theoretical and phase-contrast microscopic eigenmode analysis of erythrocyte flicker - amplitudes. *Journal De Physique Ii*, 2(5):1273–1285, 1992.

[66] S. Levin and R. Korenstein. Membrane fluctuations in erythrocytes are linked to mgatp-dependent dynamic assembly of the membrane skeleton. *Biophysical Journal*, 60(3):733–737, 1991.

[67] L. G. Mesquita, U. Agero, and O. N. Mesquita. Defocusing microscopy: An approach for red blood cell optics. *Applied Physics Letters*, 88:133901, 2006.

[68] J. Evans, W. Gratzer, N. Mohandas, K. Parker, and J. Sleep. Fluctuations of the red blood cell membrane: relation to mechanical properties and lack of atp dependence. *Biophysical Journal*, 94(10):4134–4144, 2008.

[69] W. Rasband. Imagej.

[70] W. Hackl, U. Seifert, and E. Sackmann. Effects of fully and partially solubilized amphiphiles on bilayer bending stiffness and temperature dependence of the effective tension of giant vesicles. *Journal De Physique Ii*, 7(8):1141–1157, 1997.

[71] P. Meleard, C. Gerbeaud, T. Pott, L. Fernandez-Puente, I. Bivas, MD Mitov, J. Dufourcq, and P. Bothorel. Bending elasticities of model membranes: influences of temperature and sterol content. *Biophysical Journal*, 72(6):2616–2629, 1997.

[72] E. Kreyszig. *Advanced engineering mathematics*. Wiley India Pvt. Ltd., 2007.

[73] H. Anton and C. Rorres. *Elementary Linear Algebra Applications Version*. Wiley India Pvt. Ltd., 2008.

[74] H. Engelhardt, HP Duwe, and E. Sackmann. Bilayer bending elasticity measured by fourier analysis of thermally excited surface undulations of flaccid vesicles. *Journal de Physique Lettres*, 46(8):395–400, 1985.

[75] L. Fernandez-Puente, I. Bivas, MD Mitov, and P. Méléard. Temperature and chain length effects on bending elasticity of phosphatidylcholine bilayers. *Europhysics Letters*, 28(3):181–186, 1994.

[76] A. L. Rakow and R. M. Hochmuth. Effect of heat treatment on the elasticity of human erythrocyte membrane. *Biophysical Journal*, 15(11):1095–1100, 1975.

[77] J. G. G. Dobbe, G. J. Streekstra, M. R Hardeman, C. Ince, and C. A. Grimbergen. Measurement of the distribution of red blood cell deformability using an automated rheoscope. *Cytometry*, 50(6), 2002.

[78] K. Fricke, K. Wirthensohn, R. Laxhuber, and E. Sackmann. Flicker spectroscopy of erythrocytes. *European Biophysics Journal*, 14(2):67–81, 1986.

[79] K. Zeman, H. Engelhard, and E. Sackmann. Bending undulations and elasticity of the erythrocyte membrane: effects of cell shape and membrane organization. *European Biophysics Journal*, 18(4):203–219, 1990.

[80] I. Bernhardt and J.C. Ellory. *Red cell membrane transport in health and disease*. Springer, 2003.

[81] D. E. Discher, D. H. Boal, and S. K. Boey. Simulations of the erythrocyte cytoskeleton at large deformation. ii. micropipette aspiration. *Biophysical Journal*, 75(3):1584–1597, 1998.

[82] J. Li, M. Dao, CT Lim, and S. Suresh. Spectrin-level modeling of the cytoskeleton and optical tweezers stretching of the erythrocyte. *Biophysical Journal*, 88(5):3707–3719, 2005.

[83] I.V. Pivkin and G.E. Karniadakis. Accurate coarse-grained modeling of red blood cells. *Physical Review Letters*, 101(11):118105, 2008.

[84] H. Noguchi and G. Gompper. Shape transitions of fluid vesicles and red blood cells in capillary flows. *Proceedings of the National Academy of Sciences*, 102 (40):14159–14164, 2005.

[85] I. Bivas, P. Hanusse, P. Bothorel, J. Lalanne, and O. Aguerre-Chariol. An application of the optical microscopy to the determination of the curvature elastic modulus of biological and model membranes. *Journal de Physique*, 48 (5):855–867, 1987.

[86] D. H. Boal. Computer simulation of a model network for the erythrocyte cytoskeleton. *Biophysical Journal*, 67(2):521–529, 1994.

[87] J. Abe and B. C. Berk. Reactive oxygen species as mediators of signal transduction in cardiovascular disease. *Trends In Cardiovascular Medicine*, 8(2): 59–64, 1998.

[88] J. M. Gutteridge. Lipid peroxidation and antioxidants as biomarkers of tissue damage. *Clinical Chemistry*, 41(12):1819–1828, 1995.

[89] R. M. Johnson, G. Goyette, Y. Ravindranath, and Y. S. Ho. Hemoglobin autoxidation and regulation of endogenous h2o2 levels in erythrocytes. *Free radical biology & medicine*, 39(11):1407–1417, 2005.

[90] B. R. Van Dyke and P. Saltman. Hemoglobin: a mechanism for the generation of hydroxyl radicals. *Free Radical Biology and Medicine*, 20(7):985–989, 1996.

[91] B. Halliwell and J.M.C. Gutteridge. Oxygen toxicity, oxygen radicals, transition metals and disease. *Biochemical Journal*, 219(1):1–14, 1984.

[92] E. Nagababu, F.J. Chrest, and J.M. Rifkind. Hydrogen-peroxide-induced heme degradation in red blood cells: the protective roles of catalase and glutathione peroxidase. *BBA-General Subjects*, 1620(1-3):211–217, 2003.

[93] J. J Van den Berg, K. J. A. Op, B. H. Lubin, B. Roelofsen, and F. A. Kuypers. Kinetics and site specificity of hydroperoxide-induced oxidative damage in red blood cells. *Free radical biology & medicine*, 12(6):487, 1992.

[94] C.C. Winterbourn. Free-radical production and oxidative reactions of hemoglobin. *Environmental Health Perspectives*, 64:321–330, 1985.

[95] P. Jarolim, M. Lahav, SC Liu, and J. Palek. Effect of hemoglobin oxidation products on the stability of red cell membrane skeletons and the associations of skeletal proteins: correlation with a release of hemin. *Blood*, 76(10):2125, 1990.

[96] P. S. Low, S. M. Waugh, K. Zinke, and D. Drenckhahn. The role of hemoglobin denaturation and band 3 clustering in red blood cell aging. *Science*, 227(4686): 531–533, 1985.

[97] L. M. Snyder, N. L. Fortier, J. Trainor, J. Jacobs, L. Leb, B. Lubin, D. Chiu, S. Shohet, and N. Mohandas. Effect of hydrogen peroxide exposure on normal human erythrocyte deformability, morphology, surface characteristics, and

spectrin-hemoglobin cross-linking. *The Journal of clinical investigation*, 76(5): 1971, 1985.

[98] N. Fortier, LM Snyder, F. Garver, C. Kiefer, J. McKenney, and N. Mohandas. The relationship between in vivo generated hemoglobin skeletal protein complex and increased red cell membrane rigidity. *Blood*, 71(5):1427–1431, 1988.

[99] R. A. McPherson, W. H. Sawyer, and L. Tilley. Rotational diffusion of the erythrocyte integral membrane protein, band 3: effect of hemichrome binding. *Biochemistry*, 31(2):512–518, 1992.

[100] R. J. Trotta, S. G. Sullivan, and A. Stern. Lipid peroxidation and haemoglobin degradation in red blood cells exposed to t-butyl hydroperoxide. *Biochemical Journal*, 212(75):772, 1983.

[101] C. R. Kiefer, J. F. Trainor, J. B. McKenney, C. R. Valeri, and L. M. Snyder. Hemoglobin-spectrin complexes: interference with spectrin tetramer assembly as a mechanism for compartmentalization of band 1 and band 2 complexes. *Blood*, 86(1):366, 1995.

[102] A.G. Kriebardis, M.H. Antonelou, K.E. Stamoulis, E. Economou-Petersen, L.H. Margaritis, and I.S. Papassideri. Progressive oxidation of cytoskeletal proteins and accumulation of denatured hemoglobin in stored red cells. *Journal of Cellular and Molecular Medicine*, 11(1):148–155, 2007.

[103] P. S. Becker, C. M. Cohen, and S. E. Lux. The effect of mild diamide oxidation on the structure and function of human erythrocyte spectrin. *Journal of Biological Chemistry*, 261(10):4620–4628, 1986.

[104] R. E. Waugh, M. Narla, C. W. Jackson, T. J. Mueller, T. Suzuki, and G. L. Dale. Rheologic properties of senescent erythrocytes: loss of surface area and volume with red blood cell age. *Blood*, 79(5):1351, 1992.

[105] R. P. Hebbel, A. Leung, and N. Mohandas. Oxidation-induced changes in

microrheologic properties of the red blood cell membrane. *Blood*, 76(5):1015–1020, 1990.

[106] S. L. Schrier and N. Mohandas. Globin-chain specificity of oxidation-induced changes in red blood cell membrane properties. *Blood*, 79(6):1586, 1992.

[107] W. Rawicz, KC Olbrich, T. McIntosh, D. Needham, and E. Evans. Effect of chain length and unsaturation on elasticity of lipid bilayers. *Biophysical Journal*, 79(1):328–339, 2000.

[108] J. J. M. Van den Berg, F. A. Kuypers, B. H. Lubin, B. Roelofsen, and J. A. F. Op den Kamp. Direct and continuous measurement of hydroperoxide-induced oxidative stress on the membrane of intact erythrocytes. *Free radical biology & medicine*, 11(3):255–261, 1991.

[109] M. Brownlee. Biochemistry and molecular cell biology of diabetic complications. *Nature*, 414(6865):813–820, 2001.

[110] National Health Service. Diabetes - introduction. World Wide Web electronic publication, 2009. URL `http://www.nhs.uk/conditions/diabetes/Pages/Introduction.aspx`.

[111] J. R. Williamson, R. A. Gardner, C. W. Boylan, G. L. Carroll, K. Chang, J. S. Marvel, B. Gonen, C. Kilo, et al. Microrheologic investigation of erythrocyte deformability in diabetes mellitus. *Blood*, 65(2):283, 1985.

[112] M. Goldstein, I. Leibovitch, S. Levin, Y. Alster, A. Loewenstein, G. Malkin, and R. Korenstein. Red blood cell membrane mechanical fluctuations in non-proliferative and proliferate diabetic retinopathy. *Graefe's Archive for Clinical and Experimental Ophthalmology*, 242(11):937–943, 2004.

[113] R. Singh, A. Barden, T. Mori, and L. Beilin. Advanced glycation end-products: a review. *Diabetologia*, 44(2):129–146, 2001.

[114] G. Münch, D. Schicktanz, A. Behme, M. Gerlach, P. Riederer, D. Palm, and R. Schinzel. Amino acid specificity of glycation and protein–age crosslinking

reactivities determined with a dipeptide spot library. *Nature biotechnology*, 17 (10):1006–1010, 1999.

[115] J.V. Glenn and A.W. Stitt. The role of advanced glycation end products in retinal ageing and disease. *BBA-General Subjects*, 2009.

[116] C.L. Rohlfing, H.M. Wiedmeyer, R.R. Little, J.D. England, A. Tennill, and D.E. Goldstein. Defining the relationship between plasma glucose and hba1c. *Diabetes Care*, 25(2):275, 2002.

[117] J. A. Miller, E. Gravallese, and H. F. Bunn. Nonenzymatic glycosylation of erythrocyte membrane proteins. relevance to diabetes. *Journal of Clinical Investigation*, 65(4):896, 1980.

[118] R. Bucala, Z. Makita, T. Koschinsky, A. Cerami, and H. Vlassara. Lipid advanced glycosylation: pathway for lipid oxidation in vivo. *Proceedings of the National Academy of Sciences*, 90(14):6434–6438, 1993.

[119] M.R. Owen, E. Doran, A.P. Halestrap, et al. Evidence that metformin exerts its anti-diabetic effects through inhibition of complex 1 of the mitochondrial respiratory chain. *Biochemical Journal*, 348(3):607–614, 2000.

[120] N. Ouslimani, M. Mahrouf, J. Peynet, D. Bonnefont-Rousselot, C. Cosson, A. Legrand, and J.L. Beaudeux. Metformin reduces endothelial cell expression of both the receptor for advanced glycation end products and lectin-like oxidized receptor 1. *Metabolism*, 56(3):308–313, 2007.

[121] E.G. Merrill and A. Ainsworth. Glass-coated platinum-plated tungsten microelectrodes. *Medical and Biological Engineering and Computing*, 10(5):662–672, 1972.

[122] M. Paulitschke and GB Nash. Micropipette methods for analysing blood cell rheology and their application to clinical research. *Clinical hemorheology*, 13 (4):407–434, 1993.

[123] J. A. Cerf and E. Cerf. Holder for rapid filling of micropipet electrodes by centrifugal action. *Pflugers Archiv-European Journal of Physiology*, 349(1): 87–90, 1974.

[124] E. A. Evans. New membrane concept applied to the analysis of fluid shear-and micropipette-deformed red blood cells. *Biophysical Journal*, 13(9):941–954, 1973.

[125] K. G. Engstrom and H. J. Meiselman. Optical and mathematical corrections of micropipette measurements of red-blood-cell geometry during anisotonic perifusion. *Cytometry*, 17(4):279–286, 1994.

[126] H. F. Bunn and P. J. Higgins. Reaction of monosaccharides with proteins: possible evolutionary significance. *Science*, 213(4504):222–224, 1981.

[127] M. G. Sacerdote and J. W. Szostak. Semipermeable lipid bilayers exhibit diastereoselectivity favoring ribose. *Proceedings of the National Academy of Sciences*, 102(17):6004–6008, 2005.

[128] D. Ruggiero-Lopez, M. Lecomte, G. Moinet, G. Patereau, M. Lagarde, and N. Wiernsperger. Reaction of metformin with dicarbonyl compounds. possible implication in the inhibition of advanced glycation end product formation. *Biochemical pharmacology*, 58(11):1765–1773, 1999.

[129] K. Tsukada, E. Sekizuka, C. Oshio, and H. Minamitani. Direct measurement of erythrocyte deformability in diabetes mellitus with a transparent microchannel capillary model and high-speed video camera system. *Microvascular Research*, 61(3):231–239, 2001.

[130] P. Beisswenger and D. Ruggiero-Lopez. Metformin inhibition of glycation processes. *Diabetes & metabolism*, 29(4):6–6, 2003.

[131] H. Khouri, F. Collin, D. Bonnefont-Rousselot, A. Legrand, D. Jore, and M. Gardès-Albert. Radical-induced oxidation of metformin. *European Journal of Biochemistry*, 271(23-24):4745, 2004.

[132] S. Muller, S. Denet, H. Candiloros, R. Barrois, N. Wiernsperger, M. Donner, and P. Drouin. Action of metformin on erythrocyte membrane fluidity in vitro and in vivo. *European Journal of Pharmacology*, 337(1):103–110, 1997.

[133] J. W. Baynes. Role of oxidative stress in development of complications in diabetes. *Diabetes*, 40(4):405–412, 1991.

[134] S. Rahbar, R. Natarajan, K.K. Yerneni, S. Scott, N. Gonzales, and J.L. Nadler. Evidence that pioglitazone, metformin and pentoxifylline are inhibitors of glycation. *Clinica Chimica Acta*, 301(1-2):65–77, 2000.

[135] G. Gompper and D. M. Kroll. Network models of fluid, hexatic and polymerized membranes. *Journal of Physics-Condensed Matter*, 9(42):8795–8834, 1997.

[136] D.A. Fedosov, B. Caswell, and G.E. Karniadakis. General coarse-grained red blood cell models: I. mechanics. *Arxiv preprint arXiv:0905.0042*, 2009.

[137] M.A. Haidekker, N. L'Heureux, and J.A. Frangos. Fluid shear stress increases membrane fluidity in endothelial cells: a study with dcvj fluorescence. *American Journal of Physiology - Heart and Circulatory Physiology*, 278(4):1269–1273, 2000.

[138] P. O'Shea. Intermolecular interactions with/within cell membranes and the trinity of membrane potentials: kinetics and imaging. *Biochemical Society Transactions*, 31:990–996, 2003.